SOLAR CELL CONTACTS: QUANTIFYING THE IMPACT OF INTERFACIAL LAYERS ON CHARGE TRANSFER, SELECTIVITY, RECOMBINATION, AND OPEN-CIRCUIT VOLTAGE

by

KIRA ELISE EGELHOFER RUEGGER

A DISSERTATION

Presented to the Department of Chemistry and Biochemistry
and the Graduate School of the University of Oregon
in partial fulfillment of the requirements
for the degree of
Doctor of Philosophy

September 2020

DISSERTATION APPROVAL PAGE

Student: Kira Elise Egelhofer Ruegger

Title: Solar Cell Contacts: Quantifying the Impact of Interfacial Layers on Charge Transfer, Selectivity, Recombination, and Open-Circuit Voltage

This dissertation has been accepted and approved in partial fulfillment of the requirements for the Doctor of Philosophy degree in the Department of Chemistry and Biochemistry by:

Shannon Boettcher	Chair
Mark Lonergan	Advisor
Cathy Wong	Core Member
Benjamín Alemán	Institutional Representative

and

Kate Mondloch	Interim Vice Provost and Dean of the Graduate School

Original approval signatures are on file with the University of Oregon Graduate School.

Degree awarded September 2020.

DISSERTATION ABSTRACT

Kira Elise Egelhofer Ruegger

Doctor of Philosophy

Department of Chemistry and Biochemistry

September 2020

Title: Solar Cell Contacts: Quantifying the Impact of Interfacial Layers on Charge Transfer, Selectivity, Recombination, and Open-Circuit Voltage

Solar cells require two primary components to function: an absorber and contacts, either of which may limit photovoltaic efficiency. For example, the contacts of silicon and perovskite solar cells limit their performance. To increase efficiency, interfacial layers (IFLs) sandwiched between absorber and contact are frequently used. Improvements due to IFLs are often attributed to changes in qualitative ideas of selectivity and recombination. Further, IFL/contact properties are conflated with performance parameters that depend on the entire cell.

While IFLs may improve efficiency, knowledge of their precise impact on electron and hole transfer at contacts and the relation of these effects to efficiency and well-defined concepts of selectivity and recombination is lacking, limiting photovoltaic technology development. This work addresses this gap by measuring both electron and hole transfer rates at IFL-modified contacts. Further, these rates are related to the open-circuit voltage, an important photovoltaic performance metric, and definitions of selectivity and recombination developed by our group. Specifically, the action of spiro-OMeTAD, the most common IFL used in perovskite solar cells, is characterized by making it a third contact to the interdigitated back-contact silicon solar cell. This architecture creates a three-

in-one photovoltaic that, with numerical simulation, provides equilibrium exchange current densities for electrons (J_{0n}) and holes (J_{0p}) as quantitative charge transfer rates. We define contact selectivity as the ratio of the two J_0 values at one contact (*e.g.*, J_{0p}/J_{0n}) while $(J_{0n}J_{0p})^{0.5}$ describes contact recombination.

Compared to bare gold, adding spiro-OMeTAD reduces $(J_{0n}J_{0p})^{0.5}$ by 10^4, passivating gold to recombination. Incorporating common dopants Li- and Co-TFSI and oxygen exposure increase J_{0p}/J_{0n} by up to 10^9. The improvement in V_{oc} from using spiro-OMeTAD in these cells, however, is not directly due to these changes but rather to increased electron collection asymmetry between the two contacts. The effects of additive *t*-BP on the J_0 values also lend insight into unique chemistry when Co-TFSI is used, likely influencing its effect on V_{oc}. Further, *operando* measurements demonstrate the contribution of spiro-OMeTAD to broadly observed hysteresis behavior. These insights will aid the rational design of IFLs for improved photovoltaic efficiencies.

This dissertation contains both published and unpublished co-authored work.

CURRICULUM VITAE

NAME OF AUTHOR: Kira Elise Egelhofer Ruegger

GRADUATE AND UNDERGRADUATE SCHOOLS ATTENDED:

University of Oregon, Eugene, OR
Willamette University, Salem, OR

DEGREES AWARDED:

Doctor of Philosophy, Chemistry, 2020, University of Oregon
Master of Science, Chemistry, 2016, University of Oregon
Bachelor of Arts, 2015, Chemistry, Willamette University

AREAS OF SPECIAL INTEREST:

Photovoltaics
Materials Science
Renewable Energy

PROFESSIONAL EXPERIENCE:

Rosaria Haugland Graduate Research Fellow, Department of Chemistry and Biochemistry, University of Oregon, Eugene, OR, 2017-2020

Graduate Research Fellow, Department of Chemistry and Biochemistry, University of Oregon, Eugene, OR, 2016-2017

Graduate Teaching Fellow, Department of Chemistry and Biochemistry, University of Oregon, Eugene, OR, 2015-2016

GRANTS, AWARDS, AND HONORS:

Rosaria Haugland Graduate Research Fellowship, Department of Chemistry and Biochemistry, University of Oregon, 2017-2020

Cum Laude, Willamette University, 2015

Senior Certificate, Willamette University, 2015

Phil Hanni Award, Institute for Continued Learning, Willamette University, 2015

Webber Scholarship, Willamette University, 2014-2015

PUBLICATIONS:

K.E. Egelhofer Ruegger, E.T. Roe, M.C. Lonergan, Solar cell contacts: Quantifying the impact of interfacial layers on selectivity, recombination, charge transfer, and V_{oc}, *Proc. Nat. Acad. Sci.*, in Review July 2020.

E.T. Roe, **K.E. Egelhofer**, M.C. Lonergan, Exchange current density model for the contact-determined current-voltage behavior of solar cells, *J. Appl. Phys.*, 2019, **125**, 225302.

E.T. Roe, **K.E. Egelhofer**, M.C. Lonergan, Limits of contact selectivity/recombination on the open-circuit voltage of a photovoltaic, *ACS Appl. Energy Mater*., 2018, **1**, 1037-1046.

R.P. Milstead, K.T. Nance, K.S. Tarnas, **K.E. Egelhofer**, D.R. Griffith, Photochemical degradation of halogenated estrogens under natural solar irradiance, *Environ. Sci.: Processes Impacts*, 2018, **20**, 1350-1360.

J.W. Boucher, A.L. Greenaway, **K.E. Egelhofer**, S.W. Boettcher, Analysis of performance-limiting defects in pn junction GaAs solar cells grown by water-mediated close-space vapor transport epitaxy, *Sol. Energy. Mat. Sol. C.*, 2017, **159**, 546-552.

ACKNOWLEDGEMENTS

I have been extraordinarily fortunate in my life to have the love and support of my parents, Alison and Kurt. I owe my opportunities in education to them; they have encouraged and supported my schooling decisions from the outset and have been a constant source of advice, wisdom, encouragement, and comfort, without which I likely would not have pursued a graduate degree.

Throughout the majority of my graduate career, I have also been fortunate to have the support of the love of my life, best friend, and husband, Alex. His unwavering support and understanding have been my rock and his love and silliness have been my escape and safe harbor through the turmoil that can be graduate school.

My friends have also been truly invaluable sources of encouragement and joy and I would not have made it through graduate school without them. In particular, Alli has been there for me every step of the way. I have never had a better, more loving, more understanding, and more supportive friend and I am so fortunate to have her in my life. I also thank my first-year cohort: Dani Hamann, Justin Dressler, Erik Leonhart, Matt Cerda, and Chris Funch for not only helping me get through first year but also for their friendship, support, and all the laughs over the years.

In addition, I want to thank my advisor Dr. Mark Lonergan for taking me on as a graduate student in his research group. I have learned an extraordinary amount from Mark both as a teacher and as my research advisor, and I am truly grateful for the opportunity to perform research in his lab. Mark is one of the most conscientious, considerate, and thoughtful people I have ever met, and I have learned as much from him outside of the research sphere as I have in. Further, Mark has been endlessly supportive of my

extracurricular activities, particularly my involvement with the UO Women in Graduate Science student organization, throughout my graduate career.

My colleagues in the Lonergan Lab taught me essentially everything I know about solar cell processing and measurement, for which I thank them immensely. I thank previous group members Doctors Ellis Roe, Chris Weber, Colin Bradley, Don Clayton, and Wes Miller, without whom I would have been lost in the world of physics, coding, instrumentation, measurement automation, and the like, and current group member Zack Crawford for his questions and insights.

I have also worked with a number of graduate rotation and undergraduate students, whom I thank for the opportunity to mentor and teach. In particular, I want to thank Natalie Dunn, as the undergraduate who worked with me the most, for her hard work and perseverance in learning how to make and test IBC cell devices and samples. I have used a number of devices she fabricated to make samples in my project.

I also want to thank the plethora of machine/electrical shop, administrative, and other staff who have helped make both my time here and specifically my research possible, including but not limited to: Kris Johnson, John Boosinger, Cliff Dax, Jim Rasmussen, Gerri Ravjaa, Kathy Noakes, Diane Lachenmeier, Leah O'Brien, Christi Mabinuori, Melodi Jayne, Mark Adams, Steve Golledge, Kurt Langworthy, Fuding Lin, and Nanette Jarenwattananon (and CAMCOR in general). Thank you also to UO Women in Graduate Science and all the graduate student board members I have been fortunate to work with.

My work has been made possible by the Rosaria Haugland Graduate Research Fellowship (2017 – 2020) and the Division of Chemical Sciences, Geosciences, and Biosciences, Office of Basic Energy Sciences through grant DE-SC0012363.

TABLE OF CONTENTS

Chapter Page

APPENDICES

LIST OF FIGURES

Figure Page

Figure Page

Figure Page

Figure Page

LIST OF TABLES

Table Page

CHAPTER I

INTRODUCTION

I. Overview

This dissertation presents the research I have performed over the last several years focused on quantifying and understanding the significance of charge transfer processes at solar cell contacts under the guidance of my advisor Dr. Mark Lonergan. This work has coupled experiment and numerical simulation in the context of theory developed by my coworker Dr. Ellis Roe. All experiments and simulations were performed by myself with inspiration and guidance from both Dr. Lonergan and Dr. Roe.

Chapter I discusses the motivation for our solar cell research and, briefly, the basics of solar cell function (sections I.II and I.III). Further, it introduces the interfacial layer material studied in my research, what is known about its impact on solar cell function, and what key information is missing that we would like to find out in this work (section I.IV). Parts of Chapter I are published in Egelhofer Ruegger *et al.* 2020[1] but were rewritten for this dissertation. Chapter II summarizes the theory developed by Dr. Roe (published in Roe *et al.* 2018[2] and Roe *et al.* 2019[3]) and how we consider charge transfer at interfacial layer-modified solar cell contacts. Chapter III lays out the approach of both my experimental and simulation work and presents results from the latter. Parts of this work are published in Egelhofer Ruegger *et al.* 2020,[1] presented both in the main text and Supplementary Information, and parts were written for this dissertation. Chapter IV presents primarily the Results and Discussion from Egelhofer Ruegger *et al.* 2020,[1] that is, the results of using our approach to measure the properties of interfacial layer-modified contacts and the implications for solar cell efficiency. Chapters V and VI show a combination of work

currently in preparation for publication (Egelhofer Ruegger *et al.* 2020 (*in preparation*)[4]) and unpublished work written for this dissertation. Chapter VII presents both published[1] and unpublished results of *operando* studies investigating how charge transfer characteristics change upon solar cell operation. Lastly, Chapter VIII is newly written material to conclude this dissertation.

II. Solar cell basics

Global energy consumption is constantly on the rise, but renewable energy continues to occupy only a small proportion of total energy use compared to nonrenewable and carbon-based energy sources.[5] To decrease both emissions and our reliability on nonrenewable energy sources, renewable energy technologies must become more commercially viable. That is, their efficiency must increase, their cost must decrease, or both. When it comes to photovoltaics, new technologies are constantly being developed with the goal of creating less expensive or/and more efficient solar cells than those currently in use.[6-9] In order to quickly develop and determine the viability of new technologies, the impact of all solar cell components on efficiency must be well understood. Thus, the goal of this work is to address gaps in fundamental understanding of the relationships between the properties of certain photovoltaic components and their impact on efficiency. This advancement in understanding will aid rational design of solar cells for improved efficiencies and increased market share for renewable energy technologies.

Photovoltaic action is a competition between the selective collection of charge carriers (electrons and holes) excited due to incident light and their recombination.[10] These

carriers are collected at the contacts of the solar cell, which are often metals such as gold and silver or transparent conductive oxides such as indium tin oxide,[6-9] to generate current in the external circuit, ideally by separating electrons to one contact and holes to the other. This is the conceptual idea behind selective collection, where a "selective" contact is better at collecting one carrier than the other. This process must occur before electrons and holes recombine – that is, encounter each other and annihilate – either at the contact (interfacial or contact recombination) or in the bulk absorber material (bulk recombination) in order for the solar cell to function. Thus, contacts play a significant role in dictating photovoltaic efficiency.[2,3,10]

In addition to contacts, a solar cell must possess an absorber, which is typically sandwiched between the two contacts. The absorber material – where light is collected – is typically a semiconductor, crystalline examples of which are silicon, metal-halide perovskites, and cadmium telluride, among others.[6-9] Examples of various state-of-the-art solar cells using these absorbers, some contact materials commonly used with them, and their 2020 champion efficiencies are presented in Table 1. Crystalline semiconductors, in addition to many insulator materials and metals, possess extended crystal structures, leading to energy characteristics that can be described by continua of energy states called bands.[11] Basic energy diagrams of an intrinsic (undoped) insulator, intrinsic

Table 1. Common photovoltaic absorbers, contact examples, and champion efficiencies of cells made with the corresponding absorber material.[6-9]

Absorber material	Contact material examples	Efficiency
Crystalline silicon	a-Si:H, Ag, Al, SiO_x, SiTF, TiO_2, MoO_x	26.6 %
Amorphous silicon	Al, Ag, ITO (indium tin oxide), ZnO	14 %
Metal halide perovskite	Au, Ag, TiO_2, ZnO	24.2 %
Copper indium gallium arsenide	ZnO, NiAl, Mo	23.3 %
Cadmium telluride	Mo, ZnO, Cu, MoO_x	22.9 %

semiconductor, and metal area shown in Figure 1.

Semiconductors and insulators are characterized by the complete filling of one band, called the valence band, and an energy gap between this band and the next available band, the conduction band, which is empty. This energy gap – the band gap – possesses no available states and is much larger for an insulator than for a semiconductor. While metals may possess gaps between bands in their overall energy structure, when it comes to filling of the states they are instead characterized by the partial filling of a single band.

Intrinsic semiconductors and insulators may only conduct electrons when sufficient energy is supplied to excite an electron from the valence band into the conduction band. When the electron is excited into the conduction band, it leaves behind its positive, mobile equivalent, the hole. Electrons do not readily conduct through the filled valence band

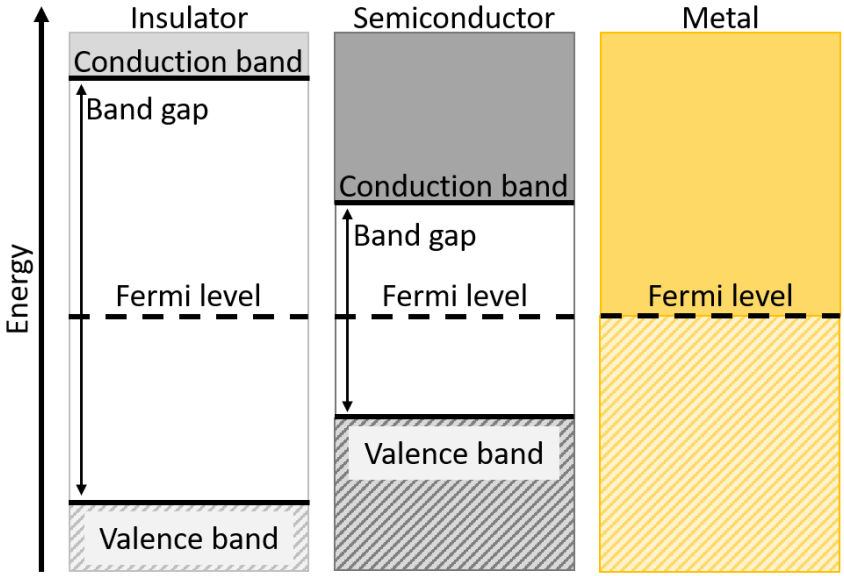

Fig. 1. Relative band energy positions of an intrinsic insulator, intrinsic semiconductor, and metal. Filled states are indicated by shaded regions while empty states are indicated by solid colors and white space indicates the absence of states. The insulator and semiconductor possess valence and conduction bands separated by a band gap while the metal is instead characterized by a partially filled band. The Fermi level of the metal is also measured as the work function.

because there are no empty, accessible energy levels into which they may move. However, states in the conduction band are empty and exist very close to one another in energy space. Thus, when an electron is excited with enough energy to promote it into the conduction band, there are many available states into which the electron may be accelerated, enabling conduction. Further, the hole generated in the valence band may also conduct due to the newly vacated state from which the electron has been promoted.

Conduction through a metal is more facile. Because states in a single band are only partially filled, empty states are much closer in energy space to filled states than in an intrinsic semiconductor. Thus, there are many energy levels readily available to accelerate electrons into, enabling facile conduction. Metals are typically used in applications where unobstructed flow of charge carriers is desired, such as when current is used or produced as it is in photovoltaics.

In a solar cell, when light of sufficient energy encounters the semiconductor absorber, it can excite an electron from the valence to the conduction band,[12] as shown in Figure 2. The excited electron may conduct through the conduction band and leaves behind

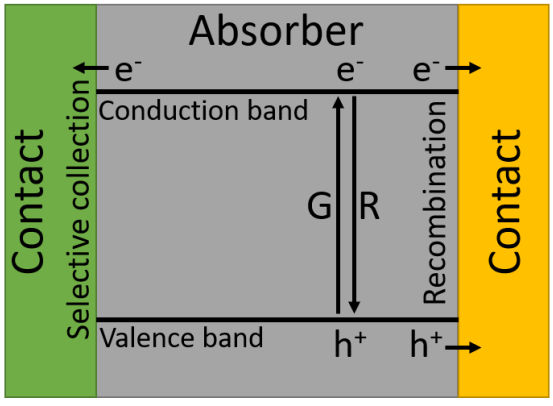

Fig. 2. Solar cell cartoon where "G" is generation due to light and "R" is bulk recombination. Interfacial processes are simplified and shown at only one contact each for clarity (both selective collection and contact recombination occur at each contact).

its positive equivalent, the hole, which is mobile and may conduct through the valence band. The electron and hole are then considered free carriers[11] and must be collected by separate contacts (*i.e.*, be collected selectively) before recombining in the bulk or at a contact in order to generate current. Thus, the characteristics of the absorber material and the contacts that determine recombination and collection rates limit solar cell function.

To investigate the role of these components in dictating photovoltaic performance, the current-voltage characteristics of the solar cell are typically measured. Electrodes are connected to the two contacts, the cell is illuminated, voltage is swept, and the resulting current is recorded, generating a current-voltage (*IV*) curve as shown in Figure 3. For solar cells, the ideal relationship between voltage and current is expressed by the diode equation with a current source:

$$I = I_0 \left(e^{\left(\frac{qV}{kT}\right)} - 1 \right) - I_L \tag{1.1}$$

Where I is current, I_0 is the equilibrium exchange current or saturation current, I_L is current generated due to light, q is the elementary charge, V is the voltage across the junction, k is the Boltzmann constant, and T is temperature. Note that an equivalent expression may be written in terms of current density (J) where the current is simply divided by the area through which it flows. While this is the ideal case, real solar cells rarely demonstrate perfect behavior. Comparing the *IV* curve of a real solar cell to the ideal equation can provide general information about areas of improvement but does not provide information about the properties of individual components (*e.g.*, one contact) or how those properties contribute to overall performance.

Despite this limitation, the *IV* curve is still an essential tool for measuring and understanding solar cell function. To determine efficiency, for example, there are several

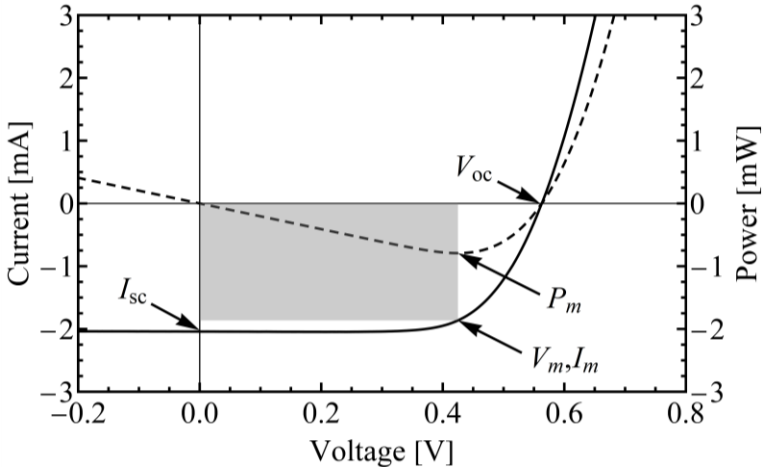

Fig. 3. Current-voltage (*IV*) curve (solid) and power curve (dashed) of a real solar cell under illumination. In this case, negative power corresponds to that generated by the cell while positive values correspond to power consumption. (V_m,I_m) is the point on the *IV* curve where maximum power is generated by the solar cell, corresponding to P_m on the power curve. The gray rectangle is the numerator when calculating both the fill factor and the power conversion efficiency.

important points to consider. Two of these points are marked in Fig. 3: the short-circuit current (I_{sc}) and open-circuit voltage (V_{oc}). The former measures the current when there is zero applied voltage while the latter measures the voltage where there is zero net current.

The solar cell only generates power in the power quadrant, the quadrant in Fig. 3 where voltage is positive and current is negative. Power is simply the product of voltage and current, and the maximum power *generated* by the cell, P_m, occurs in the power quadrant when the absolute magnitude of the product of the voltage and current is maximized, denoted (V_m,I_m) in Fig. 3. In addition to the V_{oc} and I_{sc}, two other performance metrics are typically used: the fill factor (FF) and power conversion efficiency (η). The fill factor is the comparison of P_m to the power that would be generated if the *IV* curve were a perfect rectangle and therefore produced its maximum power at (V_{oc},I_{sc}). Thus, the fill factor is

$$FF = \frac{V_m I_m}{V_{oc} I_{sc}} \tag{1.2}$$

The power conversion efficiency is a comparison of the power produced by the solar cell to the incident power from incoming photons. Thus,

$$\eta \equiv \frac{P_{out}}{P_{in}} = \frac{V_m I_m}{P_{in}} \tag{1.3}$$

Both the absorber material and contacts may limit solar cell efficiency. While the limits of solar cell efficiency dictated by the absorber were explored and described by Shockley and Queisser in their seminal theoretical work in the 1960s,[13] more recent models (including our own, herein termed REL Theory) have been developed to describe the role of contacts in limiting efficiency.[2,3,14] Briefly, REL Theory describes the dependence of solar cell performance metrics on precise definitions of contact properties (selectivity and recombination) in terms of quantitative charge transfer measures at contacts. More details about these models are provided in Chapter II.

III. Contact-limited solar cells

When it comes to relationships between the contacts and photovoltaic performance, a contact that collects one type of carrier with no restriction or energy loss while completely rejecting the other presents no limitations to the efficiency of a solar cell. Such a contact is perfectly selective[10] and does not contribute to electron-hole recombination because it only collects one type of carrier.

The concept of a perfectly selective contact is well understood, but less so is the imperfect selective contact where both carriers are collected at some finite rate and neither without some restriction. In this case, what is the quantitative definition of selectivity? As the contact may now collect both carriers, how does the concept of selectivity relate to electron-hole recombination at the contact? How in turn do imperfect selectivity and

contact recombination limit efficiency? These questions are addressed in the recent theoretical models[2,3,14] mentioned in section I.I and highlight the need for precise definitions and quantitative measures of selectivity and recombination, but these models have not been explored experimentally. Further, prominent solar cell technologies such as silicon[15] and metal-halide perovskites[16] are limited by their contacts. Consequently, there has been intense interest in improving solar cell contacts to the perfectly selective limit. This pursuit is often cast in terms of designing and developing carrier-selective contacts, but the term "carrier selective" is typically used without definition.

In the literature, the selectivity and recombination characteristics of a solar cell and its contacts are often *qualitatively* related to changes in performance metrics such as the power conversion efficiency and the V_{oc}.[17-28] In this work, we focus on the latter. However, the V_{oc} of the cell may increase if the selectivity improves or if there is a decrease in contact recombination, or both. Because the selectivity and recombination characteristics of a solar cell can both contribute to the V_{oc} and therefore to the performance, using the V_{oc} to measure selectivity and recombination characteristics of solar cell contacts is problematic because they can work in concert or in competition to cause changes in V_{oc}. Further, the V_{oc} also depends on the properties of the rest of the solar cell, particularly the other contact.

A common means of improving solar cell contacts is through the introduction of an interfacial layer (IFL) between the absorber and current-collecting electrode of a photovoltaic.[6-9,17-29] This is particularly true in emerging technologies based on perovskite absorbers and perovskite-containing tandem architectures.[30-34] IFL materials are many and varied, ranging from metal oxides to conjugated fullerenes and polymers to nanoparticles to organics.[6-9,17-29,30-34] As with solar cell contacts in general, performance enhancements

are often qualitatively described in terms of selectivity or recombination or both, but their role in the action of IFLs remains unclear. For instance, the most recent and comprehensive review of IFLs[29] states that "interfacial layers with appropriate energy levels are introduced to enhance the charge selectivity of the corresponding electrode by preventing unfavorable recombination…". This statement connects decreased recombination with improved selectivity, the extreme limit of which is no recombination at a perfectly selective contact. But are selectivity and recombination really connected in an imperfect contact, or are they distinct, independent phenomena as others[25] suggest? This question embodies the broader mechanistic ambiguity surrounding the terms selectivity and recombination as applied to IFLs, which has hindered fundamental understanding and thus rational design of IFLs across established and emerging materials systems.

The mechanistic ambiguity surrounding the terms selectivity and recombination as applied to IFLs is amplified by the fact that the action of IFLs is most often explored by measuring their effect on parameters, such as the V_{oc},[17-28] that convolute recombination and selective carrier collection not just at a single contact but throughout the entire photovoltaic, as discussed above. Ultimately, the action of IFLs needs to be understood in terms of the fundamental rates of electron and hole transfer processes at the interface, as affected by, for instance, energy level shifts or the introduction of other charge transfer barriers as shown in Figure 4 (refer to section II.II for a more in-depth and quantitative discussion of how energy level alignments and charge transfer barriers contribute to charge transfer rates in the context of REL Theory[3,4]). The interrelation between and action of IFLs on selectivity, recombination, and these interfacial electron and hole transfer rates remains a significant knowledge gap.

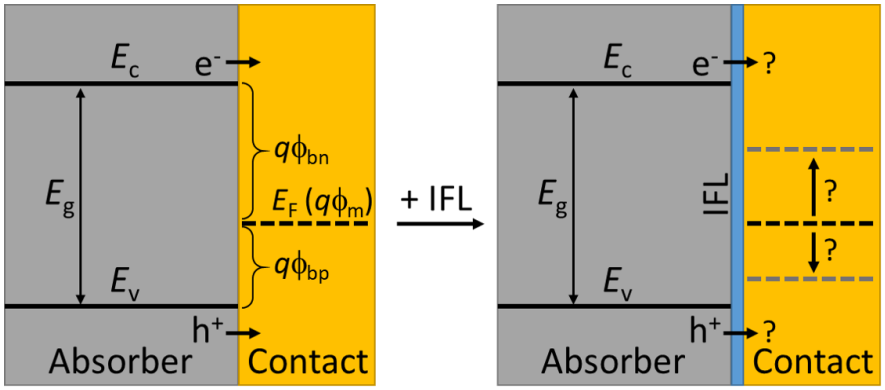

Fig. 4. General energy level alignment at the solar cell absorber/contact interface where E_c, E_v, and E_g are the conduction, valence, and band gap energies, respectively. E_F is the Fermi level energy or work function ($q\phi_m$) of the contact and $q\phi_{bn}$ and $q\phi_{bp}$ are the barriers to electron and hole transfer, respectively. When an IFL is added, it can shift the effective energy level of the contact from the perspective of carriers in the absorber and introduce other charge transfer barriers that are not captured in energy level shifts.

To complement REL Theory and to address limitations in the field's fundamental understanding of the role of solar cell contacts in determining efficiency, the specific aim of this work is to measure charge transfer rates at solar cell contacts and relate them to selectivity, recombination, and photovoltaic performance metrics to develop a more complete understanding of how to rationally design solar cell IFLs and contacts for higher efficiencies.

IV. Spiro-OMeTAD interfacial layers

A prime example of where there is need for further mechanistic understanding of the impact of IFLs on charge transfer and therefore performance is in describing the action of the most common hole selective IFL used in perovskite and solid-state dye-sensitized (SSDS) solar cells, 2,2',7,7'-tetrakis-(N,N-di-*p*-methoxyphenylamine)-9,9'-spirobifluorene (spiro-OMeTAD).[17-19,21,24,27,30,31,37,38] Figure 5 shows the chemical structures of spiro-OMeTAD and its additives and general solar cell structures it is used in.

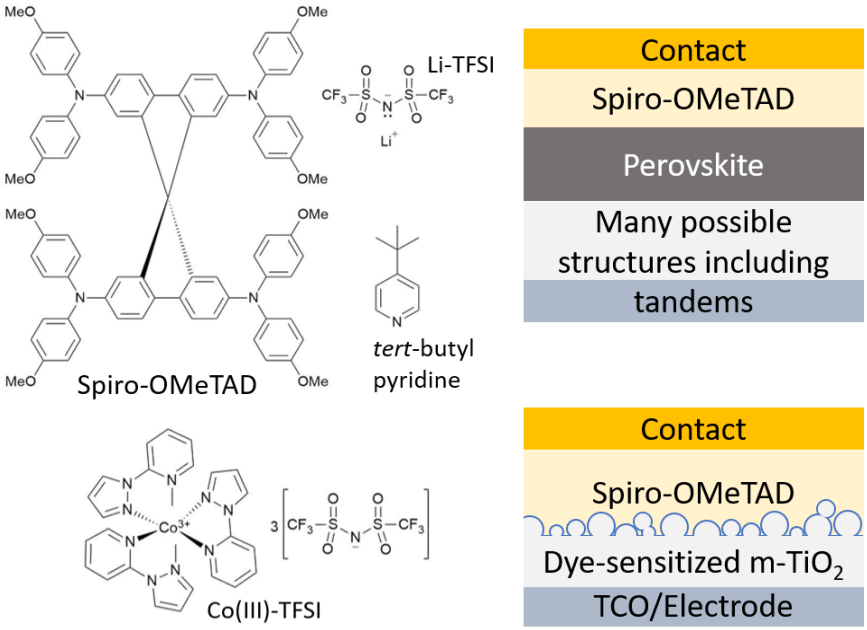

Fig. 5. Structures of spiro-OMeTAD, Li-TFSI, *tert*-butyl pyridine, and Co(III)-TFSI (left) and examples of solar cells that use spiro-OMeTAD including perovskites and perovskite tandems (top right) and solid-state dye-sensitized cells (bottom right).

A contact modified with spiro-OMeTAD is commonly referred to as a hole selective contact.[22,23,25,27,39] Its operation as such is primarily attributed to two interrelated factors. The first stems from the energy level alignments between the contact and the absorber. Photoemission spectroscopy studies show that spiro-OMeTAD introduces more significant charge transfer barriers to electron transfer relative to hole transfer when used with perovskite absorbers.[30,36] And while in these studies the effects of spiro-OMeTAD on the charge transfer rates are not quantified, the V_{oc} has been shown to change when the charge transfer barriers change.[36] The second factor is the effect of spiro-OMeTAD on the recombination of photogenerated charge carriers. Impedance spectroscopy and electroluminescence measurements have shown that spiro-OMeTAD can increase recombination resistance and reduce nonradiative recombination, respectively, relative to the unmodified gold electrode in perovskite solar cells.[20,22] Furthermore, transient

measurements of cell properties in SSDS cells have shown that common dopant bis(trifluoromethane)sulfonimide lithium salt (Li-TFSI) affects recombination lifetimes.[17]

Changes in recombination lifetimes and energy level alignments are often related to the ability of the spiro-OMeTAD to block electrons,[23,27,36] the "undesired" carrier, but the mechanisms by which this quality alters V_{oc} and its importance relative to other factors remains uncertain. Specifically, it is unclear whether changes in the collection of the undesired carrier are entirely responsible for changes in performance or whether modifications in hole collection also contribute. Hole processes have been shown to impact performance through low hole mobility in spiro-OMeTAD films, causing series resistance and thus degrading the fill factor.[20,27] In fact, the importance of hole transport has been a common explanation for the need to dope spiro-OMeTAD to increase the conductivity.[16,17] However, this doping can also modify charge transfer barriers by shifting energy level alignments,[37] and hence could impact both electron and hole transfer at the interface.

In fact, the complexity of the action of spiro-OMeTAD is greatly increased by the addition of such additives. Salts such as Li-TFSI and tris(2-(1*H*-pyrazol-1-yl)pyridine)cobalt(III) bis(trifluoromethane)sulfonimide (Co-TFSI) are commonly used, in addition to *tert*-butyl pyridine (*t*-BP), which aids the incorporation of the ionic salts into the organic spiro-OMeTAD thus acting as a morphological controller.[17,37,39-46] The impact of Li-TFSI is fairly well understood but some questions remain. Transient measurements of cell properties in SSDS cells have shown that Li-TFSI affects recombination lifetimes.[17] Further, the addition of Li-TFSI oxidizes spiro-OMeTAD in the presence of oxygen, generating spiro-OMeTAD$^{\bullet+}$.[18] This process essentially p-dopes the material, shifting energy level alignments at the absorber/contact interface.[37] These energy level shifts can

impact both electron and hole transfer at the interface, but the relative importance of electron *vs.* hole transfer rates in determining performance when Li-TFSI is present, including how they relate to recombination and selectivity, is unknown.

The role of *t*-BP, previously considered to primarily impact film morphology,[39,40] is likewise poorly understood from the perspective of quantitative charge transfer. A recent study showed that *t*-BP neutralizes spiro-OMeTAD$^{\bullet+}$,[41] the formation of which has long been considered the mechanism that tunes the energy level of spiro-OMeTAD to make it "hole selective."[17,37] Complexation between *t*-BP and Li^+ has also been suggested,[40] which would effectively decrease the concentration of spiro-OMeTAD$^{\bullet+}$ as well. This oxidized species of spiro-OMeTAD is often observed spectroscopically and spectra are used to quantify the amount of spiro-OMeTAD$^{\bullet+}$ generated due to the presence of salts such as Li- and Co-TFSI.[43] The changes in energy level or other contact properties that could occur in response to the reaction of this species with *t*-BP, however, are yet unknown. Further, Kruger *et al.* showed an *increase* in the lifetime of spiro-OMeTAD$^{\bullet+}$ in SSDS cells when *t*-BP was present compared to when it was not,[47] attributed to a decrease in charge recombination in the presence of *t*-BP. Thus, *t*-BP could play a more complicated role than previously thought, and its specific quantitative contributions to charge transfer rates, energy level shifts (*i.e.*, contact selectivity), and changes in interfacial recombination, in addition to how it could interact with other additives such as Li- and Co-TFSI, remain unknown.

The role of Co(III) salts has been investigated in more depth than that of *t*-BP. Photoluminescence (PL) measurements of spiro-OMeTAD-containing perovskites have shown that the presence of Co(III) salt produces lower PL signals than when only Li-TFSI

and *t*-BP are present in the spiro-OMeTAD layer.[46] Similarly, transient photovoltage[46] and impedance measurements[45] both show longer lifetimes when Co(III) salts are present *vs.* when they are not. These results all indicate slower recombination in the presence of Co(III) salts. At the same time, observed increases in V_{oc} of both SSDS and perovskite solar cells when Co(III) salts are added[42-46] could be due to changes in either the recombination or selectivity characteristics of the contact, or the charge transfer rate of only one carrier. In short, the role of these salts in determining energy levels and charge transfer characteristics of spiro-OMeTAD-modified contacts is not understood.

Though visible spectroscopy measurements demonstrate spiro-OMeTAD oxidation upon incorporation of Co(III) salts,[42-44] there is a lack of clear evidence that this oxidation actually shifts the energy level and, further, that those changes would contribute to the observed changes in V_{oc} when Co(III) salts are used. In fact, the conductivity of spiro-OMeTAD films with Co(III) salt was shown to be lower than spiro-OMeTAD films with Li-TFSI and *t*-BP,[44] indicating that Co(III) salts could have unknown/different effects on the electronic properties of spiro-OMeTAD films than UV-Vis measurements alone would suggest. Additionally, when only Co(III) salt was used in spiro-OMeTAD in complete perovskite solar cells,[44] the V_{oc} was greater than when only Li-TFSI and *t*-BP were present despite the lower conductivity, and a further improvement occurred when all three additives were used. These results could suggest that: 1) Oxidation due to Co(III) salts does not have the same effect on the properties of the spiro-OMeTAD-modified contact as oxidation due to Li-TFSI and air and 2) Co(III), Li-TFSI, or/and *t*-BP could work synergistically to change the charge transfer properties of the contact and therefore improve overall performance metrics, most notably the V_{oc}. However, there is no direct evidence to

support either of these conclusions, nor is there any knowledge of the role *t*-BP plays in dictating the charge transfer properties of the contact when only Co(III) or both Co(III) and Li-TFSI are present. This information is key for optimizing the use of spiro-OMeTAD IFLs incorporating Co(III) salts (which most recipes do[20,24,28]) and for the use of dopants in IFLs in general.

In addition to their potential impact on steady-state charge transfer characteristics of spiro-OMeTAD-modified contacts, Li- and Co-TFSI introduce mobile ions, which can contribute to hysteretic behavior observed principally in perovskite solar cells.[20,33,48-50] Hysteretic behavior is the dependence of the current-voltage characteristics on pre-scan conditions. For example, if the solar cell is held under illumination at open circuit before the *IV* curve is measured, the current-voltage characteristics (and therefore efficiency) are different than if it is instead held at short circuit beforehand. This behavior is typically considered undesirable because it indicates the solar cell may be unable to perform consistently over time under changing environmental conditions and thus may be unsuitable for commercialization.

Pre-scan conditions and scan direction affect the current-voltage characteristics of both SSDS and perovskite solar cells containing spiro-OMeTAD.[20,33,48-50] There are mixed reports concerning whether spiro-OMeTAD contributes to hysteresis,[48-50] but Jacobs *et al.* show that ion accumulation in perovskite absorbers increases recombination at the absorber/spiro-OMeTAD interface and decreases hole injection from spiro-OMeTAD into the perovskite, indicating that spiro-OMeTAD does indeed play a role.[48] However, it is unclear whether these effects are caused entirely by ion accumulation in the absorber or if pre-scan light/voltage application (*i.e.*, cell operation) changes the properties of spiro-

OMeTAD itself. The effects of cell operation on the electron and hole transfer rates are simply unknown. Thus, this work also seeks to address the role of spiro-OMeTAD and its additives in contributing to hysteresis through changes in charge transfer properties induced by solar cell operation. Understanding the role of spiro-OMeTAD in hysteresis behavior is crucial for mitigating its potential contributions to hysteresis in perovskite and SSDS cells in addition to providing general information about the role of IFLs in hysteresis behavior, which remains largely unexplored to date.

In summary, in light of what is known (and not known) about the impact of spiro-OMeTAD IFLs and IFLs in general at solar cell contacts, there are two specific aims of this dissertation. The first is to measure electron and hole transfer rates at a solar cell contact and describe the relation of these rates to selectivity, recombination, and the important cell-level photovoltaic metric V_{oc}. The second is to advance understanding of the specific action of spiro-OMeTAD on modifying gold contacts and improving the V_{oc} of a solar cell. The two goals are synergistic in that the spiro-OMeTAD system is an excellent one to address the first because it can be widely tuned through the addition of Li- and Co-TFSI, air oxidation, and the application of bias (*i.e.*, solar cell operation). In turn, achieving the first goal provides exactly the fundamental understanding needed to mechanistically describe the action of spiro-OMeTAD including the effect of additives and cell operation. The findings presented herein provide essential insights to the field which will help develop methods of engineering solar cell IFLs for higher photovoltaic efficiencies.

CHAPTER II

THEORY OF CONTACT-LIMITED SOLAR CELLS

Many theories have been developed to describe the relationships between the properties of solar cell components and how those components limit both certain performance metrics and overall efficiency.[2,3,13,14,51-57] This chapter summarizes some of these theories (section II.I), in particular our group's approach (REL Theory[2,3]), to provide the foundation from which measurements and simulations are performed in this work. Section II.II summarizes work published in Roe *et al.* 2018[2] and Roe *et al.* 2019.[3]

I. Theoretical limits to solar cell efficiency

In the 1960s, Shockley and Queisser presented the detailed balance limit of efficiency for pn junction solar cells.[13] This theory shows both the dependence of the efficiency on the band gap of the absorber material and that the maximum attainable efficiency occurs when all recombination is radiative. That is, recombination only occurs when an electron and hole encounter each other and annihilate in the bulk of the absorber with the emission of a photon rather than in a non-radiative event such as when an electron and hole are collected by the same contact simultaneously. This assumes the contacts are perfectly selective.

It is clear even from Shockley and Queisser's treatment that non-radiative recombination, *e.g.*, recombination at the contacts, can limit solar cell performance. More recent works have shown experimentally that cells with both silicon[15] and perovskite[16] absorbers are limited by their contacts and that a theoretical understanding of exactly how contacts limit performance is necessary to improve current solar cell efficiencies. In fact,

quite a few theoretical studies have explored the factors that dictate contact-limited solar cell behavior for a variety of absorber technologies.[14,51-57] Understandably, these theories approach the concept of a selective contact as collecting "desired" *vs.* "undesired" carriers and typically focus on the effects of only one or the other.

Mora-Seró and Bisquert developed a general model based on a generic semiconductor sandwiched by two selective contacts, one perfectly selective and the other not.[51] They showed that introducing trap states for the minority carrier at the nonideal contact interface strongly influenced solar cell performance parameters. Sandberg *et al.* also developed a general model for sandwich-type thin-film solar cells where they likewise treated one contact as perfectly selective.[52] They then determined an analytic expression for the relationship between collection of the undesired carrier at the non-perfectly selective contact and V_{oc} in various regimes where surface recombination is limited by bulk *vs.* interfacial transfer processes.

When it comes to specific solar cell technologies, many more models have been explored and developed. Early on, Niemegeers and Burgelman developed an analytic model to describe "rollover" behavior observed in the current-voltage characteristics of cadmium telluride (CdTe) solar cells.[57] Rollover is where current in forward bias does not increase exponentially with applied voltage as predicted by the ideal diode equation of the solar cell (eq. 1.1) but instead reaches a maximum value and plateaus, which can have a negative impact on performance. To model this behavior, they used a back-to-back diode structure in which one of the diodes presents a barrier to the extraction of majority carriers, which they showed was responsible for the rollover behavior. In organic solar cells, Kirchartz *et al.* showed relationships between charge separation and carrier collection and

the V_{oc} by incorporating surface recombination both at the donor/acceptor interface in the bulk and at the contacts.[14] Further, Wagenpfahl *et al.* showed that restricting the majority carrier transfer at the anode in organic solar cells, like in CdTe cells, was responsible for rollover behavior and provided an analytic expression for the dependence of the V_{oc} on majority carrier transfer limitations.[56] In silicon solar cells, Chavali *et al.* likewise showed that a barrier to majority carrier extraction directly resulted in nonideal solar cell behavior.[54] Brendel and Peibst took the treatment of silicon solar cells a step further by incorporating both the majority and minority carrier processes at a single contact, using a ratio of majority to minority carrier resistances to describe contact selectivity.[53] They then demonstrated that the efficiency depends both on this selectivity parameter and on a contact recombination parameter.

While these models provide insight into the properties of solar cell contacts that can limit efficiency, only Brendel and Peibst showed that consideration of both carrier processes at a single contact are important[53] and none of them considered the collection of *both* carriers at *both* contacts. Only a treatment that takes into account all four collection processes can provide a thorough model of contact-determined solar cell performance. This is where REL Theory comes in.

II. REL Theory

In REL Theory, charge transfer processes for both the desired and undesired carrier are considered at both contacts.[2,3] The model addresses the relations between these processes, well-defined concepts of selectivity and recombination, and the current-voltage behavior of a complete, general sandwich configuration solar cell. REL Theory considers

charge transfer at the absorber/contact interface using the equilibrium exchange current density (J_0) for thermionic emission, which can be applied to the description of both heterojunctions[58] and semiconductor/metal interfaces,[59] and is described by:

$$J_{0\mathrm{x}} = \kappa_{\mathrm{x}} A^*_{\mathrm{x}} T^2 e^{\left(\frac{-q\phi_{\mathrm{bx}}}{kT}\right)} \tag{2.1}$$

where A^*_{x}, κ_{x}, and ϕ_{bx} are the Richardson coefficient, transmission coefficient, and barrier height for electrons (x = n) or holes (x = p).[11,59] The J_0 measures the flux of charge carriers crossing the interface per unit area at dynamic equilibrium, that is, when no *net* current flows, and can be measured for real solar cells.

There are two J_0 values at each contact, as shown in Figure 6, one for electrons and one for holes. Thus, there are four J_0 values in every sandwich-type solar cell. Throughout this thesis, superscript labels are used to specify the contact or contacts associated with a particular quantity. The contact under study is labelled with either "E" or "H" to signify

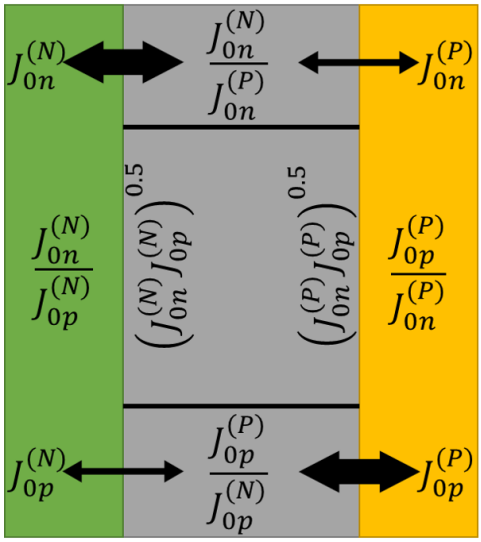

Fig. 6. Exchange current densities (J_0s) for a sandwich-type solar cell where the green contact is the "electron contact" and the yellow, the "hole contact" which are designated by the superscripts "N" and "P", respectively, for clarity. The J_0-based definitions of contact selectivity are shown in their respective contacts, of carrier selectivity are shown at the top and bottom of the absorber, and of contact recombination are shown at the two absorber/contact interfaces.

whether it operates as the electron or hole contact, respectively, in a measurement. Any other contacts in the cell are labelled either "N" or "P" to signify whether they operate as the electron or hole contact, respectively. As the J_{0p} and J_{0n} values of the contact under consideration do not depend on whether it is operating as an electron or hole contact, we simply omit the superscript. Hence, any time a J_0 value is presented without a superscript it should be considered that of the contact under study (refer to Chapter III and section IV.I for more information regarding the contact under study in this work).

To describe the properties of a contact in terms charge transfer, we define two types of selectivity (contact and carrier) and contact recombination in terms of the four J_0 values. We define contact selectivity as the ratio of the J_0 values of the two carriers at *one contact*, *e.g.*, the hole contact selectivity $S_{con} = J_{0p}/J_{0n}$. Carrier selectivity (S_{car}) is instead the ratio of the J_0 values of the *same carrier* at the two separate contacts. For example, the electron carrier selectivity is defined as $S_{car,n} = J_{0n}^{(N)}/J_{0n}$. REL Theory finds that while S_{con} is useful in characterizing the J_0 values at a contact, the carrier selectivity is more important in dictating the current density-voltage ($J(V)$) behavior because it describes the asymmetry available to support the quasi-Fermi level splitting (QFLS) in the cell, which measures the balance of generation and recombination. Contact recombination is defined as the geometric mean of the exchange current densities, $(J_{0n}J_{0p})^{0.5}$, which describes the geometric average of the number of electrons and holes collected by the contact simultaneously.

Further, REL Theory finds that the $J(V)$ behavior of a contact-limited solar cell depends on the carrier selectivity of both the electron and hole, but one typically dominates in the power quadrant. Here, how these relationships specifically impact the V_{oc} will be

discussed. When, for example, the electron is limiting (*i.e.*, the hole collection asymmetry is greater than the electron collection asymmetry) and J_L is greater than J_{0n} at both contacts:

$$V_{oc} = \frac{kT}{q} ln(S_{car,n}) \tag{2.2}$$

where k is the Boltzmann constant, T is temperature, and q is the elementary charge. When J_L is instead between J_{0n} at the electron contact and J_{0n} at the hole contact, there is excess carrier asymmetry in the system, and the contact-limited V_{oc} is given by:

$$V_{oc} = \frac{kT}{q} ln\left(\frac{J_L}{J_{0n}}\right) \tag{2.3}$$

where J_{0n} refers to that of the hole contact. Herein, we refer to this latter situation as a light-limited carrier selectivity. If a cell is instead limited by contact recombination rather than by carrier selectivity, the V_{oc} is given by the QFLS/q. When considering a cell with QFLS/q limited by recombination at the hole contact:

If $J_L > J_{0p} > J_{0n}$ $$V_{oc} = \frac{kT}{q} ln\left(\frac{J_L}{(J_{0n}J_{0p})^{0.5}}\right) \tag{2.4a}$$

If $J_{0p} > J_L > J_{0n}$ $$V_{oc} = \frac{kT}{q} ln\left(\frac{J_L}{J_{0n}}\right) \tag{2.4b}$$

These two expressions come from recombination being second order (eq. 2.4a) *vs.* quasi-first order (eq. 2.4b). When J_L is larger than both J_{0p} and J_{0n}, the carrier concentrations at the contact must change significantly from their equilibrium values to support the light current, *i.e.*, both J_{0n} and J_{0p} must change. Because both J_{0n} and J_{0p} change significantly, V_{oc} depends on them both – specifically, on their geometric mean $(J_{0n}J_{0p})^{0.5}$. Both J_{0n} and J_{0p} dictate the recombination-limited V_{oc}, thus, recombination is second order. Conversely, when J_L is smaller than the larger J_0, in this case J_{0p}, carrier concentrations at the contact do not need to change significantly from their equilibrium values and the V_{oc} depends only on the J_0 for the limiting carrier, in this case J_{0n}, and recombination is quasi-first order. In

this work, J_L is greater than both J_{0n} and J_{0p} for all IFL-modified contacts (refer to Chapters IV – VI for the J_0 values of the IFL-modified contacts studied herein). Thus, eq. 2.4a applies, and if the V_{oc} is limited by contact recombination, it depends on $(J_{0n}J_{0p})^{0.5}$.

Throughout this work we refer to changes in the J_0 values as changes in contact properties. To understand the origins of changes in the J_0 values when IFLs are introduced, the following is a discussion of the properties of the contact or IFL-modified contact that can influence the J_0 value itself. As shown in eq. 2.1, J_0 depends on only two quantities that are not constants, κ_x and ϕ_{bx}. Figure 7 shows a schematic demonstrating how these two parameters contribute to charge transfer at the interface.

The IFL-modified interface can be viewed as a perturbed semiconductor/metal interface in which case the ϕ_{bn} and ϕ_{bp} are given by the difference between the contact Fermi level and conduction and valence band energies, respectively, of the absorber. The IFL in this case is seen as modifying the effective work function of the metal with any additional charge transfer barrier due to tunneling or additional band offsets being captured

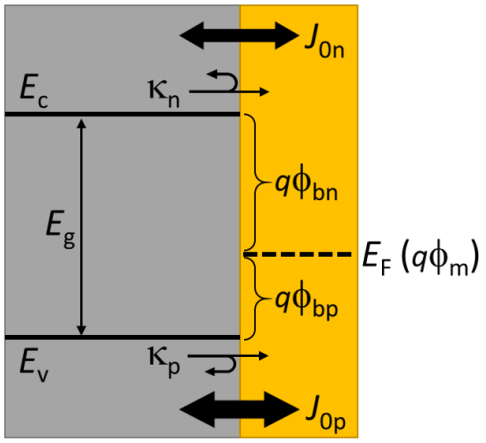

Fig. 7. Thermionic emission contributions to charge transfer processes at the absorber/contact interface where E_c, E_v, and E_g are the conduction band, valence band, and band gap energies, respectively. The $q\phi_{bn}$ and $q\phi_{bp}$ are the barrier heights and κ_n and κ_p the transmission coefficients for electrons and holes, respectively, and E_F ($q\phi_m$) is the Fermi level (work function) of the yellow contact.

in κ. For a metal/semiconductor contact, κ is one, but it is generally less than one for molecular contacts with a lower density of states than a metal. In addition, the ϕ_{bn} and ϕ_{bp} of a semiconductor/metal contact sum to the band gap energy, and changes in these quantities are typically equated with so-called work function effects. Alternatively, the IFL/contact can be considered in terms of a type I heterojunction where band offsets can be included in the ϕ_{bn} and ϕ_{bp} terms. Either way, any shift in the energy levels or contact work function that causes an increase in one of the barriers would cause a decrease in the other. If an IFL causes only a change in ϕ_{bp} (and therefore ϕ_{bn}) and not κ, only the contact selectivity will be affected. Specifically, if ϕ_{bp} increases by Δ, J_{0p}/J_{0n} will change by a factor of $\exp[2q\Delta/kT]$ while $(J_{0n}J_{0p})^{0.5}$ will remain unchanged.

For $(J_{0n}J_{0p})^{0.5}$ to change, there must be a change in κ, introduced by, for example, band offsets that present additional charge transfer or tunneling barriers. In parallel to the J_{0p}/J_{0n} case, if an IFL causes a change in only κ but not in ϕ_b, only $(J_{0n}J_{0p})^{0.5}$ will change while J_{0p}/J_{0n} will remain unchanged. Measuring J_{0p}/J_{0n} and $(J_{0n}J_{0p})^{0.5}$ allows us to determine the individual J_{0n} and J_{0p} values through simple arithmetic. Initially, however, using definitions of contact selectivity and recombination, rather than individual J_0 values, allows one to *directly* relate properties of the interface – κ and ϕ_b – to quantitative charge transfer parameters and thus to photovoltaic performance metrics like the V_{oc} through eq.s 2.2 – 2.4. Thus, the treatment provided by REL Theory allows one to understand the relationships between collection processes for both carriers at both contacts, the selectivity and recombination characteristics of those contacts, and overall solar cell performance. This information is useful for rationally designing solar cell contacts for improved contact-limited solar cell efficiencies. Further, understanding the interface in terms of ideas like

selectivity and recombination is also useful to the field because these ideas are already commonly used to qualitatively describe solar cell contacts.

In summary, many theoretical descriptions of the processes that occur at contacts to dictate solar cell performance metrics have been developed.[14,51-57] The theory developed by our group (REL Theory), however, is the first to consider the entire contact-limited sandwich structure solar cell in a general sense.[2,3] REL Theory treats charge transfer at each absorber/contact interface as being described by the equilibrium exchange current density (J_0) for each carrier and shows how in different situations, the V_{oc} of the cell can depend on the J_0 values (and on selectivity and recombination) in different ways. Knowing these relationships and their implications is key for understanding the impact of IFLs in contact-limited solar cells.

CHAPTER III

MEASURING SELECTIVITY, RECOMBINATION, AND CHARGE TRANSFER AT INTERFACIAL LAYER-MODIFIED CONTACTS

This chapter presents our approach to measuring selectivity, recombination, and charge transfer at solar cell contacts, which involves a combination of experiment and numerical simulation. It is taken from both the Introduction and Results and Discussion sections of Egelhofer Ruegger *et al.* 2020[1] but has been minimally edited to stand on its own in this chapter. Here, the experimental platform and simulation approach of this work are described in addition to simulation results. Experimental results and the use of simulation results to extract charge transfer (J_0) values from experimental data are presented in Chapters IV – VII.

Our equilibrium exchange current density-based definitions of contact selectivity (J_{0p}/J_{0n}) and recombination ($(J_{0n}J_{0p})^{0.5}$) are discussed in detail in section II.II. In order to measure these quantities, we use the commercially available interdigitated back-contact (IBC) silicon solar cell as a platform to measure the selectivity and recombination properties of IFL-modified contacts. To determine the J_0 values responsible for these selectivity and recombination characteristics, we use a model of the same IBC cell in COMSOL, a simulation software tool, to determine the relationships between J_{0p}/J_{0n} and $(J_{0n}J_{0p})^{0.5}$ and the quantities we can measure with experimental IBC cells. Thus, section III.I describes the use of the IBC cell to measure selectivity and recombination properties of IFL-modified contacts, section III.II details the use of numerical simulation to model the IBC cell, and section III.III presents the simulation results and discusses their significance.

I. IBC cell measurements of contact selectivity and recombination

Our unique approach to measuring the selectivity and recombination properties of IFL-modified contacts uses a third contact to a commercially available interdigitated back-contact (IBC) silicon solar cell, illustrated as the spiro-OMeTAD-modified gold contact in Figure 8.[60,61] This single structure provides three separate solar cells in one, created from a lightly n-doped silicon absorber interfaced with either: (1) the top and n^+ contacts, (2) the top and p^+ contacts, or (3), the n^+ and p^+ contacts, where the n^+- and p^+-Si contacts are the state-of-the-art electron and hole selective contacts to silicon, respectively. In these three cells, the contact under study (the top contact) acts respectively as: (i) the hole contact, (ii) the electron contact, or (iii) a recombination-active surface. All three cells may be simultaneously monitored *for the same film and during photovoltaic operation* to study the effects of environmental or pre-biasing conditions.

The ability to measure hole and electron processes and recombination simultaneously with the IBC cell, coupled with the capacity to accurately model it using numerical simulation (see sections III.II and III.III), allows us to extract exchange current densities (J_0s) quantifying electron and hole transfer. Aided by theoretical models,[2,3] these

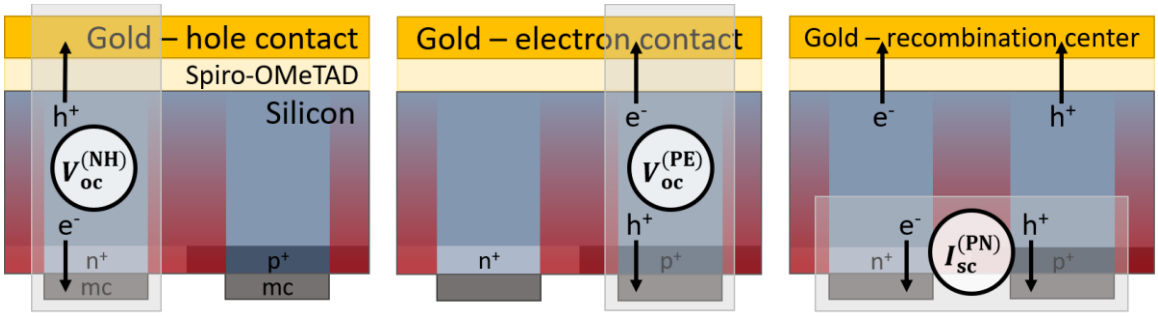

Fig. 8. Cross section of illuminated IBC cell structure[61] consisting of a lightly n-doped silicon absorber with interdigitated n^+- and p^+-Si contacts on the bottom and a top, IFL-modified metal-electrode contact. The cell is illuminated (indicated by areas of red to represent red light) through the interdigitated metal contacts on the back. Layers not to scale (see Fig. 9).

J_0 values are then related to concepts of selectivity and recombination and to solar cell performance. The underlying physics illustrated on the silicon model system provide guidance for the rational design of contacts to other more complicated absorber materials such as perovskites.

We measure three quantities using the illuminated IBC cell to describe the contact under study: $V_{oc}^{(PE)}$, $V_{oc}^{(NH)}$, and $I_{sc}^{(PN)}$, all taken to be positive. The superscripts "P" and "N" refer to the p^+- and n^+-Si back contacts, respectively, while "H" and "E" refer to the top contact's action as either the hole or electron contact when measured *vs.* the back n^+- or p^+-Si contact, respectively. The $I_{sc}^{(PN)}$ is the short-circuit current measured between the n^+- and p^+-Si contacts while $V_{oc}^{(NH)}$ and $V_{oc}^{(PE)}$ are the V_{oc}s measured between the top contact and the n^+- or p^+-Si contacts. First, we will introduce the qualitative meaning of these parameters then return to a quantitative understanding through numerical simulation and theory. Our group previously used the IBC cell to characterize the effect of conjugated polyfluorenes on interfacial charge transfer, but only studied $V_{oc}^{(PE)}$ and $V_{oc}^{(NH)}$ in that work.[60] The measurement of $I_{sc}^{(PN)}$ provides significant additional information on recombination.

The $V_{oc}^{(NH)}$ tells us how the contact under study performs as the hole contact and $V_{oc}^{(PE)}$ as the electron contact. The labels "hole contact" and "electron contact" should not be overinterpreted. Changes to $V_{oc}^{(NH)}$ and $V_{oc}^{(PE)}$ may signal changes in the effectiveness of the top contact as a hole or electron contact, respectively. This does not mean that the contact is necessarily becoming more efficient at collecting holes or electrons, respectively, because there are many different rate processes that can lead to changes in V_{oc}. However,

a *comparison* of $V_{oc}^{(NH)}$ and $V_{oc}^{(PE)}$ measured using the IBC cell, *i.e.*, the difference $V_{oc}^{(PE)} - V_{oc}^{(NH)}$ or $V_{oc}^{(NH)} - V_{oc}^{(PE)}$, describes the ability of the contact to act as one contact compared to as the other and thus can tell us about the contact selectivity of the contact under study.

The $I_{sc}^{(PN)}$ is a measure of the interfacial recombination at the top contact. If there is no interfacial recombination, $I_{sc}^{(PN)}$ is unaffected. As recombination at the contact increases, fewer electrons and holes are available for the p^+- and n^+-contacts to collect, thus decreasing $I_{sc}^{(PN)}$. This is akin to measuring surface recombination velocities using transistor geometries.[62] We note that carrier diffusion lengths in the IBC cell are long enough[11,61] for $I_{sc}^{(PN)}$ to be sensitive to changes in recombination of the top contact.

The IBC cell quantities we measure to describe the action of IFLs are all cell-level characteristics that depend on the balance of many different kinetic processes. Our goal is to quantify how IFLs modify the kinetics of individual electron and hole processes at the interface and understand their relation to overall cell performance. To achieve this, we use numerical simulation to connect the cell-level parameters $V_{oc}^{(PE)}$, $V_{oc}^{(NH)}$, and $I_{sc}^{(PN)}$ to the quasi-Fermi level splitting (QFLS) and to J_{0n} and J_{0p}. As discussed in section II.II, quantitative measurements of J_{0n} and J_{0p} provide a framework for understanding how concepts of selectivity and recombination limit solar cell performance. Next, the model of the IBC cell used for numerical simulation to extract these quantities will be presented.

II. Numerical simulation model of the IBC cell

COMSOL was used to model a 2D representation of the IBC cell including the top contact under study as shown in Figure 9. Numerical simulations were performed using the 2D semiconductor module at 300K with a 2.25 mm wide and 200 μm thick silicon absorber with 0.392 cm cross section (for which measured values were corrected; direct current scaling was verified). The bulk silicon was lightly n-doped (10^{15} cm^{-3}) with n^+- and p^+-doped regions on the bottom (495 μm wide and 2 μm deep) with their respective ohmic metal contacts (250 μm wide in the middle of the dopant well). Beer-Lambert Generation was used in defined areas to account for contact "shadowing." Auger and SRH Recombination were present everywhere in the device. The top contact was simulated with a metal Schottky contact 2.25 mm wide on the top of the silicon bulk.

To generate the simulation results, the program calculated $V_{oc}^{(PE)}$, $V_{oc}^{(NH)}$, and $I_{sc}^{(PN)}$ of the device with a normal mesh while varying J_{0p}/J_{0n} (from 2.3×10^{-7} to 1.4×10^{6}) and $(J_{0n}J_{0p})^{0.5}$ (from 3.5×10^{-8} to 3.5×10^{-3} A/cm^2) of the top metal contact. Shunt resistance was introduced at the back side (in between the metal contacts) to match experimental V_{oc}s of pristine IBC cells. Table 2 shows the parameters used in the simulations.

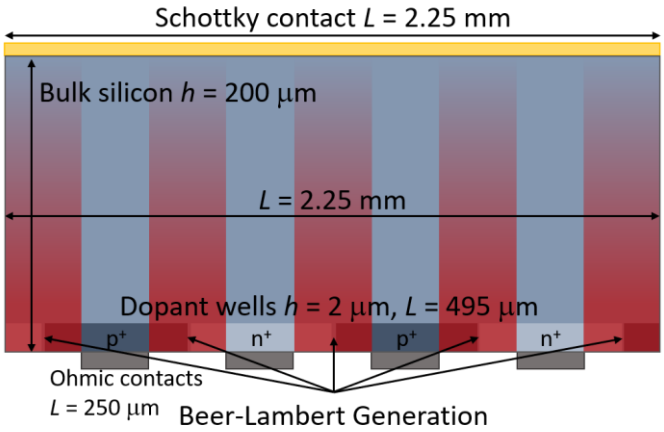

Fig. 9. Two-dimensional IBC cell model used in COMSOL simulations.

Table 2. Simulation model parameters

Symbol	Description	Value
T	Temperature	300 K
E_g	Band gap	1.12 eV
ε_r	Relative permittivity	11.7
χ_0	Electron affinity	4.05 V
N_C	Effective conduction band DOS	10^{19} cm^{-3}
N_V	Effective valence band DOS	2.7×10^{19} cm^{-3}
$N_{D,b}$	Dopant density, bulk Si	10^{15} cm^{-3}
$N_{A,d}$	Dopant density, p^{+}-Si dopant wells	10^{18} cm^{-3}
$N_{D,d}$	Dopant density, n^{+}-Si dopant wells	10^{18} cm^{-3}
μ_n	Electron mobility	1448 cm^{2}V^{-1}s^{-1}
μ_p	Hole mobility	473 cm^{2}V^{-1}s^{-1}
G_L	Electron and hole Beer-Lambert generation rate; y is distance on y coordinate	$(1.52\times10^{21})\exp(-y/\alpha[\mu m^{-1}])$ cm^{-3}s^{-1}
α	Absorption depth	10 μm
res	Resistance between back p & n contacts	0 Ω for $I_{sc}^{(PN)}$, 10^{10} Ω for $V_{oc}^{(PE)}$ and $V_{oc}^{(NH)}$
J_{0p}/J_{0n}	Contact selectivity, top contact	2.3×10^{-7} to 1.4×10^{6} as a geometric series with common ratio 4.7
$(J_{0n}J_{0p})^{0.5}$	Interfacial recombination, top contact	3.5×10^{-8} to 3.5×10^{-3} A/cm^2 as a geometric series with common ratio 1.3
C	Auger recomb. coeff. for electrons and holes	2.0×10^{-30} cm^6/s
τ	SRH lifetime for electrons and holes	1 ms in bulk silicon; 10 μs in dopant wells

In the COMSOL simulations, the boundary conditions are described by the diode equation for the partial currents of electrons and holes, J_n and J_p, at the interface between the semiconductor and the contact under study:

$$J_x = J_{0x}\left(e^{\left(\frac{qV}{kT}\right)} - 1\right) \tag{3.1}$$

where V is the voltage across the junction, q is the elementary charge, k is the Boltzmann

constant, T is temperature, and x = n (p) for electron (hole) processes. Charge transfer at many semiconductor interfaces is described by eq. 3.1, including certain types of metal/semiconductor interfaces, pn junctions, and heterojunctions.[11,58,59] In particular, for eq. 3.1 to apply, the semiconductor must generate free carriers (as opposed to excitons) upon excitation. Semiconductors that produce free carriers include perovskites,[62] silicon, cadmium telluride, and other crystalline absorbers.[11,58,59] J_{0n} and J_{0p} enter into the simulations through these boundary conditions. Simulations were performed by varying J_{0p}/J_{0n} and $(J_{0n}J_{0p})^{0.5}$ while solving for $V_{oc}^{(PE)}$, $V_{oc}^{(NH)}$, and $I_{sc}^{(PN)}$. Next, simulation results showing the relationships between $V_{oc}^{(PE)}$, $V_{oc}^{(NH)}$, $I_{sc}^{(PN)}$, J_{0p}/J_{0n}, and $(J_{0n}J_{0p})^{0.5}$ will be presented.

III. Numerical simulation results

This section presents the results of using the model presented in section III.II to numerically simulate the IBC cell and describes the significance of these results. The first thing the simulations provide is an estimate of the quasi-Fermi level splitting (QFLS) in the absorber using $I_{sc}^{(PN)}$. The QFLS is the difference between the electron and hole quasi-Fermi levels in the bulk of the absorber. It is determined by the balance of generation and recombination in the cell and is therefore sensitive to changes in interfacial recombination.[12] As the recombination decreases, the QFLS increases. As shown in Figure 10, the simulated QFLS increases monotonically with the simulated $I_{sc}^{(PN)}$. Hence, these results confirm the qualitative idea mentioned above that $I_{sc}^{(PN)}$ measures interfacial recombination. The fact that the different colors lie on top of each other means that the

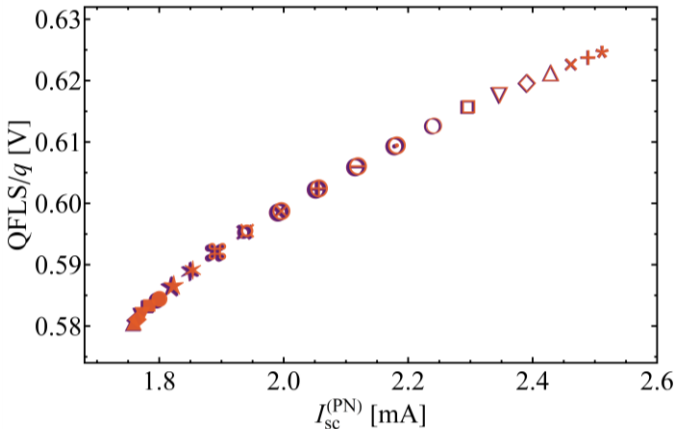

Fig. 10. Simulation results demonstrating the relationship between the QFLS and the $I_{sc}^{(PN)}$ in the COMSOL model. The symbols indicate $(J_{0n}J_{0p})^{0.5}$ with values decreasing from bottom left to top right as a geometric series from 3.5×10^{-6} to 3.5×10^{-8} A/cm^2 with common ratio 1.3. Different colors represent different values of J_{0p}/J_{0n} (from 8×10^{-1} to 9.1×10^{5}) and stack on top of each other because the QFLS does not significantly depend on J_{0p}/J_{0n}.

QFLS is independent of the ratio J_{0p}/J_{0n}. Further, the simulation data in Fig. 10 can be used to estimate the QFLS from the measured $I_{sc}^{(PN)}$.

The second thing the simulations provide is a measure of J_{0n} and J_{0p}, the fundamental parameters we use to describe how IFLs modify electron and hole transfer rates. It is useful to represent J_{0n} and J_{0p} in terms of their geometric mean, $(J_{0n}J_{0p})^{0.5}$, and ratio, J_{0p}/J_{0n}. As previously mentioned, the former describes how the IFL affects the combined rates of both electron and hole transfer and is therefore an intuitive definition of contact recombination. The latter describes how the IFL affects one rate compared to the other. In our work, J_{0p}/J_{0n} is taken as an intuitive definition of the contact hole selectivity (S_{con}) describing the relative rates of hole *vs.* electron transfer. The contact electron selectivity is defined as its reciprocal.

The significance of J_{0p}/J_{0n} and $(J_{0n}J_{0p})^{0.5}$ can be seen from the simulation results presented in Figure 11, which shows simulated values of $I_{sc}^{(PN)}$ versus $V_{oc}^{(PE)} - V_{oc}^{(NH)}$ for systematically varying values of J_{0p}/J_{0n} and $(J_{0n}J_{0p})^{0.5}$. Over a wide range of parameter

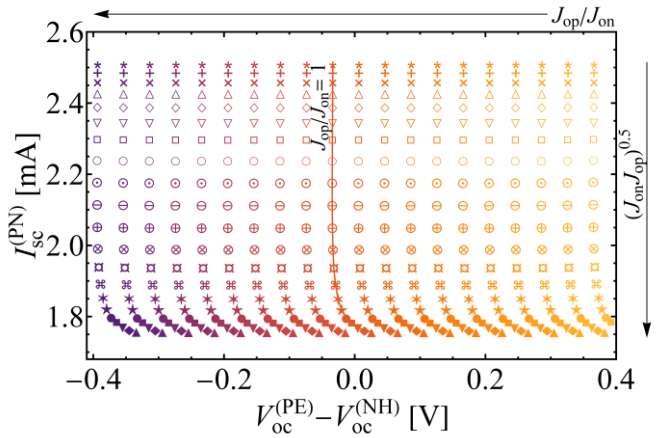

Fig. 11. Simulation results for $V_{oc}^{(PE)}$-$V_{oc}^{(NH)}$ and $I_{sc}^{(PN)}$ as a function of J_{0p}/J_{0n} and $(J_{0n}J_{0p})^{0.5}$. The symbols indicate $(J_{0n}J_{0p})^{0.5}$ with values increasing from top to bottom as a geometric series from 3.5×10^{-8} to 3.5×10^{-6} A/cm^2 with common ratio 1.3. Data with the same values of J_{0p}/J_{0n} lie in quasi vertical groupings of the same color, for example as marked for the J_{0p}/J_{0n} = 1 data. The J_{0p}/J_{0n} increases from right to left as a geometric series from 1.5×10^{-7} (lightest orange) to 9.1×10^{5} (darkest purple) with common ratio 4.7.

space, the simulated $V_{oc}^{(PE)}$–$V_{oc}^{(NH)}$ and $I_{sc}^{(PN)}$ data form a nearly rectangular grid. A perfectly rectangular grid would indicate that $V_{oc}^{(PE)}$–$V_{oc}^{(NH)}$ and $I_{sc}^{(PN)}$ measure independent quantities. The curving over of the $I_{sc}^{(PN)}$ data at the bottom of the plot indicates the region of $(J_{0n}J_{0p})^{0.5}$ parameter space where bulk transport, rather than interfacial recombination, begins to limit the QFLS and therefore the $I_{sc}^{(PN)}$. The direction of curvature is determined by the doping of the bulk silicon; when it is switched from lightly n- to p-doped the direction also changes. Fig. 11 shows that $V_{oc}^{(PE)}$–$V_{oc}^{(NH)}$ changes systematically with J_{0p}/J_{0n} but has little dependence on $(J_{0n}J_{0p})^{0.5}$. Hence, over a wide range of parameter space $V_{oc}^{(PE)}$–$V_{oc}^{(NH)}$ is a measure of contact selectivity; the comparison of the action of the contact as a hole contact *vs.* as an electron contact describes the asymmetry of hole *vs.* electron processes at the contact.

The $I_{sc}^{(PN)}$ changes systematically with $(J_{0n}J_{0p})^{0.5}$ but has little dependence on J_{0p}/J_{0n} for the range of parameter space and light intensity in the grid-like region of the simulation results. The net recombination rate at an interface with partial currents governed by eq. 3.1 depends on the excess carrier concentrations relative to those present at equilibrium. When both carrier concentrations have to be driven significantly from equilibrium to support recombination of the light current density (J_L), the net recombination rate is second order and is thus described by $(J_{0n}J_{0p})^{0.5}$.[2,3] This is the situation we encounter because J_L is greater than both J_{0n} and J_{0p} in the grid-like region. Overall, the simulation results show that IBC cell measurements of $I_{sc}^{(PN)}$ and $V_{oc}^{(PE)}$–$V_{oc}^{(NH)}$ are measures of contact recombination and selectivity, respectively, as defined by REL Theory.

To extract J_0 values for experimental IFL-modified contact, we compare experimental values of $I_{sc}^{(PN)}$ and $V_{oc}^{(PE)}$–$V_{oc}^{(NH)}$ to the simulation data in Fig. 11 to find $(J_{0n}J_{0p})^{0.5}$ and J_{0p}/J_{0n} and hence to determine J_{0n} and J_{0p}. To do so, we generate an interpolation function relating simulated $V_{oc}^{(PE)}$–$V_{oc}^{(NH)}$ and $I_{sc}^{(PN)}$ values to the J_{0p}/J_{0n} and $(J_{0n}J_{0p})^{0.5}$ used to generate them. This is essentially a mathematical representation of the data shown in Fig. 11. The interpolation function is then solved using the experimental $V_{oc}^{(PE)}$–$V_{oc}^{(NH)}$ and $I_{sc}^{(PN)}$ data to find the corresponding J_{0p}/J_{0n} and $(J_{0n}J_{0p})^{0.5}$ values which are then used to calculate the individual J_{0n} and J_{0p} values. The same process is used with the QFLS simulation results to determine experimental QFLS values. The gold contact is treated slightly differently in the interpolation than filmed samples. Because it resides in the bulk recombination limit, we set the value of the Richardson Coefficient, A^*, to the value for metals. We only then use the interpolation function to determine the J_{0p}/J_{0n} and

$(J_{0n}J_{0p})^{0.5}$ for unmodified gold. To see data overlaid on simulation results and the resulting J_0 values for experimental IFL-modified contacts, refer to section IV.X.

In this work, the action of spiro-OMeTAD IFLs on the properties of gold contacts is of interest (for more, see sections I.IV and IV.I). Because spiro-OMeTAD-modified gold is used as the hole contact in perovskite and SSDS cells,[17-19,21,24,27,30,31,37,38] we are interested in the V_{oc} when it acts as such, *i.e.*, the $V_{oc}^{(NH)}$. Specifically, we would like to know how the charge transfer values, selectivity, and recombination are related to $V_{oc}^{(NH)}$ for spiro-OMeTAD-modified gold contacts. In order to determine these relations, we must first understand the general relationships between the J_0 values and the $V_{oc}^{(NH)}$. Thus, these relationships, determined using numerical simulation and for the IBC cell geometry, are shown in Figure 12. Note that these results may also be obtained simply using REL Theory because that is where the boundary conditions and other assumptions used in the simulation

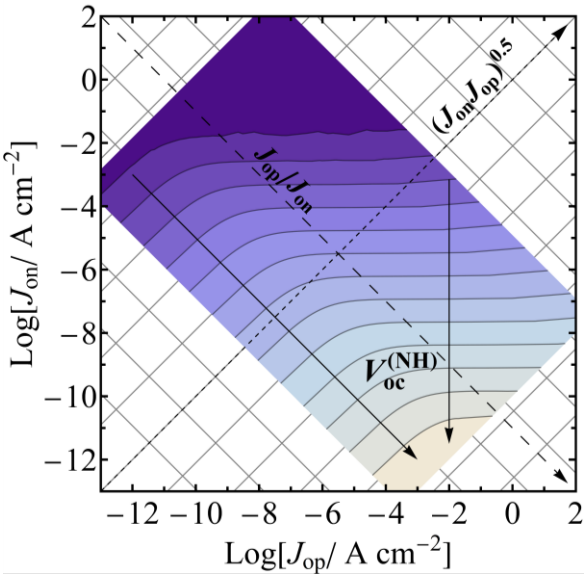

Fig 12. Contour plot of simulated $V_{oc}^{(NH)}$ values as a function of J_{0n} and J_{0p}. The darkest purple region corresponds to $V_{oc}^{(NH)}$ < 0.04 V and the tan region to $V_{oc}^{(NH)}$ > 0.54 V. The $V_{oc}^{(NH)}$ contours increase by 0.04 V in the direction of the arrows. The underlying grid shows constant values of J_{0p}/J_{0n} and $(J_{0n}J_{0p})^{0.5}$ increasing in the directions of the long- and short-dashed arrows, respectively.

come from.[2] The gray grid lines in the background show the relationships between the individual J_0 values and the contact hole selectivity and contact recombination. From top left to bottom right, the contact hole selectivity J_{0p}/J_{0n} increases systematically with the grid lines perpendicular to the long-dashed arrow. From bottom left to top right, the contact recombination $(J_{0n}J_{0p})^{0.5}$ increases systematically with the grid lines perpendicular to the short-dashed arrow.

The blue scale contour plot shown in Fig. 12 addresses the relationships between the contact-level J_0 values and the cell-level device metric $V_{oc}^{(NH)}$. We first note that the QFLS, which is 0.58 to 0.63 eV over the entire simulated region (see Fig. 10), is always greater than $qV_{oc}^{(NH)}$. This means the QFLS does *not* limit the V_{oc}. Next, there are two characteristic regions of the $V_{oc}^{(NH)}$ contour plot. In the region where the contours of equal $V_{oc}^{(NH)}$ run parallel to the J_{0p} axis and perpendicular to the J_{0n} axis, $V_{oc}^{(NH)}$ depends on J_{0n} but not J_{0p}. To illustrate, if one follows the vertical arrow on the right side of the $V_{oc}^{(NH)}$ contour plot, J_{0p} remains constant while J_{0n} changes, directly resulting in changes in $V_{oc}^{(NH)}$. However, if one were to travel from left to right in this region, changing J_{0p} but not J_{0n}, the $V_{oc}^{(NH)}$ remains unchanged. In this regime, the $V_{oc}^{(NH)}$ behavior is described by eq. 2.3 of REL Theory, *i.e.*, it depends on the carrier selectivity, in this case of the electron.

In the other region of the contour plot the contours of equal $V_{oc}^{(NH)}$ run diagonally, parallel to the J_{0p}/J_{0n} contours and perpendicular to the $(J_{0n}J_{0p})^{0.5}$ contours. In this region, $V_{oc}^{(NH)}$ depends on contact selectivity but not on the geometric mean of the J_0s. Traveling along the arrow on the left side of the plot in the direction of increasing contact hole selectivity while holding $(J_{0n}J_{0p})^{0.5}$ constant, $V_{oc}^{(NH)}$ increases. Conversely, if one were

travel along a J_{0p}/J_{0n} contour, changing $(J_{0n}J_{0p})^{0.5}$ while keeping J_{0p}/J_{0n} constant, $V_{oc}^{(NH)}$ would remain unchanged.

In summary, these results show the silicon IBC cell, aided by numerical simulation and the theoretical framework developed by our group, may be used to measure the charge transfer quantity J_0 for both the electron and hole at the contact under study. Not only do they demonstrate the applicability of our approach for measuring individual J_0 values, selectivity, and recombination, but they also show quantitative relationships between selectivity, recombination, J_0 values, and an important performance parameter, the V_{oc}. The next chapter will show the results of using the IBC cell to measure the properties of spiro-OMeTAD-modified gold contacts, *i.e.*, the selectivity, recombination, and individual J_0 values extracted from IBC cell measurements and the simulation results presented herein.

CHAPTER IV

IMPACT OF SPIRO-OMETAD AND LI-TFSI ON THE CHARGE TRANSFER PROPERTIES OF GOLD CONTACTS

This chapter presents the results of investigating the impacts of spiro-OMeTAD interfacial layers and additive Li-TFSI on the selectivity, recombination, and charge transfer properties of gold contacts. It also demonstrates the relationships between these quantities and the V_{oc} when the spiro-OMeTAD-modified gold acts as the hole contact. It is taken from the Results and Discussion section of Egelhofer Ruegger *et al.* 2020[1] and edited minimally for this dissertation.

I. IBC cell measurements of spiro-OMeTAD-modified gold contacts

Spiro-OMeTAD is the state-of-the-art "hole selective" interfacial layer material used in perovskite, SSDS, and perovskite-containing tandem solar cells.[17-19,21-25,27,30,31,36-38] It is almost never used without Li-TFSI, Co(III) salts, and *t*-BP. The role of Co(III) salts will be discussed in Chapter V and that of *t*-BP in Chapter VI. For a complete description of our motivation for studying spiro-OMeTAD, refer to section I.IV. As a brief summary, spiro-OMeTAD interfacial layers are typically associated with either an increase in majority carrier (hole) collection through doping with Li- and Co-TFSI salts or with a decrease in minority carrier (electron) collection.[16,17,20,23,27,36] Li-TFSI has been shown to cause spiro-OMeTAD oxidation through generation of superoxide, producing spiro-OMeTAD$^{\bullet+}$.[18] This oxidation processes is typically credited for "p-doping" the spiro-OMeTAD, thus increasing its hole conductivity and therefore "selectivity."[17-19,21,24,27,30,31,37,38] However, the relative importance of the majority *vs.* minority carrier

collection – and how these processes are influenced by spiro-OMeTAD$^{\bullet+}$ formation – in dictating performance metrics such as the V_{oc} and the specific role(s) of the additives listed above are not understood. Further, the relations of these carrier collection processes to well-defined concepts of selectivity and recombination are also lacking. This information is important for the optimal use of spiro-OMeTAD and its additives (and other interfacial layer materials altogether) in state-of-the-art perovskite and tandem solar cells.

In this chapter, we show how spiro-OMeTAD impacts the performance of a photovoltaic through understanding its effect on *individual* electron and hole processes at the contact (*i.e.*, J_{0n} and J_{0p}). We also show how these processes relate to the well-defined concepts of recombination and selectivity previously detailed in sections II.II and III.III, and to the photovoltaic performance metric V_{oc}. We illustrate the role of air oxidation and doping with Li-TFSI, facilitating its incorporation into spiro-OMeTAD using *t*-BP.[18,39,40,47]

In this study we investigate the effects of thin (3-5 nm) films of neat spiro-OMeTAD and spiro-OMeTAD containing Li-TFSI in a 1:4 mole ratio on the properties of gold contacts to IBC cells (for more information about the use of the IBC cell to study contact properties, refer to section III.I). Herein, the mole ratio refers to the number of moles of Li-TFSI (1) or other species per mole of spiro-OMeTAD (4).

The complete action of spiro-OMeTAD layers in a solar cell depends on how they impact the optical properties of the entire cell, carrier transport through the cell, and charge transfer at interfaces within the cell. Our studies isolate the latter. We study thin spiro-OMeTAD layers to minimize limitations from bulk transport. The ability to study such thin films is made possible by the smoothness of the single crystal silicon substrate. To minimize optical effects,[21] the cells are illuminated from the side opposite the top contact

with a wavelength (785 nm) characterized by an absorption depth that is only a fraction of the absorber thickness.

Spiro-OMeTAD films are spin coated onto IBC cells in ambient conditions and exposed to air for 10 minutes before thermal evaporation of the gold contact and then for another 10 minutes after contact deposition. To establish a baseline, samples are first held under nitrogen atmosphere for 1 hour before being re-exposed to air for measurement every 5 minutes for 6 hours. Samples are kept in the dark except for the 4–5 seconds total required for each measurement of the three IBC cell quantities $V_{\mathrm{oc}}^{(\mathrm{PE})}$, $V_{\mathrm{oc}}^{(\mathrm{NH})}$, and $I_{\mathrm{sc}}^{(\mathrm{PN})}$. More detailed descriptions of experimental procedures may be found in Appendices A – C. The use of the IBC cell to measure selectivity and recombination characteristic of IFL-modified contacts is described in section III.I.

Figure 13 shows $V_{\mathrm{oc}}^{(\mathrm{PE})}$, $V_{\mathrm{oc}}^{(\mathrm{NH})}$, and $I_{\mathrm{sc}}^{(\mathrm{PN})}$ measured over time in air. The addition of spiro-OMeTAD substantially increases the $I_{\mathrm{sc}}^{(\mathrm{PN})}$ relative to gold regardless of whether Li-TFSI is present or whether the samples have been exposed to air (Fig. 13a). Thus, spiro-OMeTAD IFLs decrease the interfacial recombination of gold contacts. The addition of Li-TFSI increases the recombination compared to when it is not present as indicated by the decrease in $I_{\mathrm{sc}}^{(\mathrm{PN})}$ from that of neat spiro-OMeTAD. After 6 hours of air exposure, the initial trend still holds.

Neat spiro-OMeTAD increases the $V_{\mathrm{oc}}^{(\mathrm{PE})}$ of unmodified gold by ~200 mV with a similar decrease in $V_{\mathrm{oc}}^{(\mathrm{NH})}$ (Fig. 13b). Exposure to air has little additional effect. The incorporation of Li-TFSI causes a slight increase (decrease) in the initial $V_{\mathrm{oc}}^{(\mathrm{NH})}$ ($V_{\mathrm{oc}}^{(\mathrm{PE})}$).

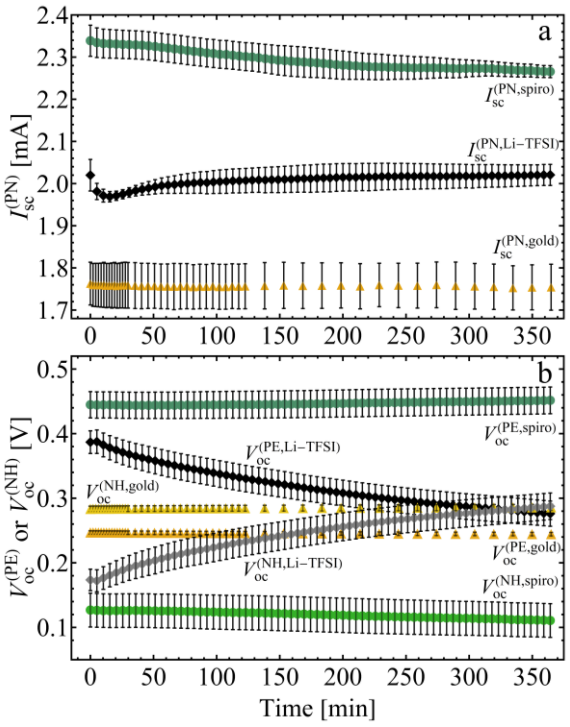

Fig. 13. Experimentally measured (a) $I_{sc}^{(PN)}$ and (b) $V_{oc}^{(PE)}$ and $V_{oc}^{(NH)}$ values and their change over time in air for unmodified gold (yellow triangles), gold modified with neat spiro-OMeTAD (green circles), and gold modified with spiro-OMeTAD containing 1:4 mole ratio Li-TFSI to spiro-OMeTAD (black/gray diamonds).

Exposure to air causes $V_{oc}^{(NH)}$ to increase by over 100 mV while $V_{oc}^{(PE)}$ decreases by about the same amount. Table 3 summarizes the experimental data collected in this study.

As mentioned in section III.I, the IBC cell quantities we measure to describe the action of spiro-OMeTAD IFLs are all cell-level characteristics that depend on the balance of many different kinetic processes. Our goal is to quantify how IFLs modify the kinetics

Table 3. Experimental $V_{oc}^{(PE)}$, $V_{oc}^{(NH)}$, $I_{sc}^{(PN)}$, and simulation-generated QFLS data for unmodified gold, neat spiro-OMeTAD-modified gold, and Li-TFSI-doped spiro-OMeTAD-modified gold before (initial) and after (final) 6 hours of air exposure. The number in parenthesis is the uncertainty in the last digit.

	$V_{oc}^{(PE)}$ (V)		$V_{oc}^{(NH)}$ (V)		$I_{sc}^{(PN)}$ (mA)		QFLS at open circuit (eV)	
	Initial	Final	Initial	Final	Initial	Final	Initial	Final
Gold	0.247(3)	0.245(3)	0.283(4)	0.276(5)	1.76(5)	1.75(5)	0.580(5)	0.581(5)
Spiro	0.44(2)	0.45(2)	0.13(3)	0.11(3)	2.34(4)	2.27(1)	0.618(2)	0.614(1)
+ Li-TFSI	0.39(2)	0.28(2)	0.17(2)	0.29(2)	2.02(4)	2.02(2)	0.601(2)	0.601(1)

of *individual* electron and hole processes at the interface and understand their relation to overall cell performance. To achieve this, we use numerical simulation to connect the cell-level parameters $V_{\mathrm{oc}}^{(\mathrm{PE})}$, $V_{\mathrm{oc}}^{(\mathrm{NH})}$, and $I_{\mathrm{sc}}^{(\mathrm{PN})}$ to the quasi-Fermi level splitting (QFLS) and to equilibrium exchange current densities, $J_{0\mathrm{n}}$ and $J_{0\mathrm{p}}$, describing the rates of electron and hole transfer at the interface, respectively. Quantitative measurements of $J_{0\mathrm{n}}$ and $J_{0\mathrm{p}}$ further provide a framework for understanding how concepts of selectivity and recombination limit solar cell performance (for more details, refer to sections II.II and III.III). The J_0 values measured using these IBC cell measurements will be presented in section IV.II.

Throughout, we use superscript labels to specify the contact or contacts associated with a particular quantity. We have chosen to label the top contact with either "E" or "H" to signify whether it operates as the electron or hole contact in a measurement. As the $J_{0\mathrm{n}}$ and $J_{0\mathrm{p}}$ values of the spiro-OMeTAD-modified contact do not depend on whether it is operating as an electron or hole contact, we simply omit the superscript. Hence, any time a J_0 value is presented without a superscript it should be considered that of the contact under study.

II. Extracted J_0 values of spiro-OMeTAD-modified gold contacts

The experimental IBC cell data collected in this study are presented in Figure 14. The initial and final time points are overlaid on the simulation results presented in section III.III. Comparing experimental to simulation results in this way allows us to extract $J_{0\mathrm{n}}$ and $J_{0\mathrm{p}}$ for spiro-OMeTAD-modified gold contacts, as described in more detail in section III.III. As a brief summary, the $V_{\mathrm{oc}}^{(\mathrm{PE})} - V_{\mathrm{oc}}^{(\mathrm{NH})}$ and $I_{\mathrm{sc}}^{(\mathrm{PN})}$ values collected experimentally are plugged in to an interpolation function relating the simulation-generated $V_{\mathrm{oc}}^{(\mathrm{PE})} - V_{\mathrm{oc}}^{(\mathrm{NH})}$ and

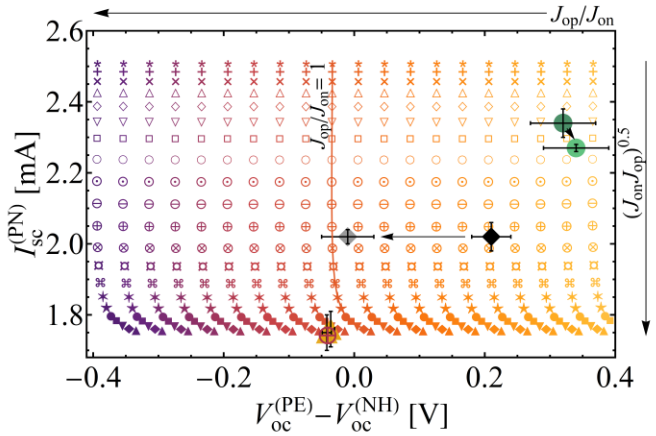

Fig. 14. Simulation results for $V_{oc}^{(PE)}$-$V_{oc}^{(NH)}$ and $I_{sc}^{(PN)}$ as a function of J_{0p}/J_{0n} and $(J_{0n}J_{0p})^{0.5}$ with experimental data overlaid. Green circles are neat spiro-OMeTAD-modified gold, black and gray diamonds are Li-TFSI-containing spiro-OMeTAD-modified gold, and yellow triangles are unmodified gold. Arrows indicate direction of change upon exposure to air. For the simulated data, symbols indicate $(J_{0n}J_{0p})^{0.5}$ with values increasing from top to bottom as a geometric series from 3.5×10^{-8} to 3.5×10^{-6} A/cm^2 with common ratio 1.3. Data with the same values of J_{0p}/J_{0n} lie in quasi vertical groupings of the same color, for example as marked for the J_{0p}/J_{0n} = 1 data. The J_{0p}/J_{0n} increases from right to left as a geometric series from 1.5×10^{-7} (lightest orange) to 9.1×10^{5} (darkest purple) with common ratio 4.7.

$I_{sc}^{(PN)}$ data to the known J_{0p}/J_{0n} and $(J_{0n}J_{0p})^{0.5}$ of the top contact in the IBC cell model. This interpolation function returns the J_{0p}/J_{0n} and $(J_{0n}J_{0p})^{0.5}$ values responsible for experimental $V_{oc}^{(PE)}-V_{oc}^{(NH)}$ and $I_{sc}^{(PN)}$ data. Individual J_{0p} and J_{0n} values may then be calculated.

The J_0 values of the experimental spiro-OMeTAD-modified gold contacts determined from this treatment are shown in Figure 15, overlaid on the contour plot of $V_{oc}^{(NH)}$ reproduced from Fig. 12. We use $V_{oc}^{(NH)}$ because it is the V_{oc} for the cell where spiro-OMeTAD-modified gold acts as the hole contact as it does in perovskite and SSDS solar cells. This representation shows the J_{0p}, J_{0n}, J_{0p}/J_{0n}, $(J_{0n}J_{0p})^{0.5}$, and $V_{oc}^{(NH)}$ values of these contacts simultaneously.

The relationships between the J_0 values, J_{0p}/J_{0n}, $(J_{0n}J_{0p})^{0.5}$, and $V_{oc}^{(NH)}$ presented in Fig. 15 are detailed in section III.III. To briefly summarize, the background gray grid shows

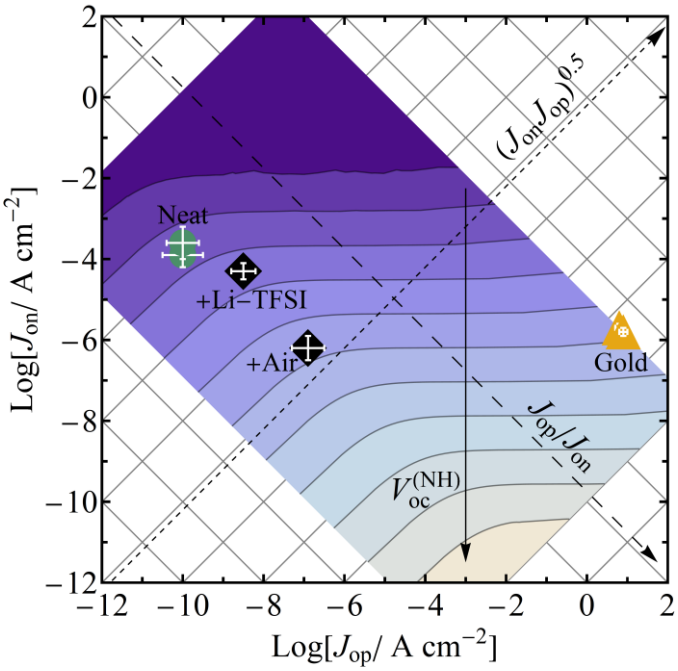

Fig. 15. Contour plot of simulated $V_{oc}^{(NH)}$ values as a function of J_{0n} and J_{0p}. The $V_{oc}^{(NH)}$ contours increase by 0.05 V in the direction of the downward vertical arrow. The darkest purple region corresponds to $V_{oc}^{(NH)}$ < 0.05 V and the tan region to $V_{oc}^{(NH)}$ > 0.55 V. The locations of the experimental contacts are marked as symbols with error bars: triangles indicate gold, circles indicate gold with neat spiro-OMeTAD, and diamonds indicate gold with spiro-OMeTAD containing Li-TFSI in a 1:4 mole ratio, before and after six hours in air. The underlying grid shows constant values of J_{0p}/J_{0n} and $(J_{0n}J_{0p})^{0.5}$ increasing in the directions of the long- and short-dashed arrows, respectively.

contours of constant J_{0p}/J_{0n} and $(J_{0n}J_{0p})^{0.5}$ which increase from top left to bottom right and bottom left to top right as illustrated with the long- and short-dashed arrows, respectively. The blue scale contour plot overlaid shows how the $V_{oc}^{(NH)}$ depends on J_{0p} and J_{0n} and therefore also on J_{0p}/J_{0n} and $(J_{0n}J_{0p})^{0.5}$. There are two distinct regimes of behavior – one where the contours of constant $V_{oc}^{(NH)}$ are parallel to the x axis, and one where the contours are parallel to the J_{0p}/J_{0n} contours. In the former region, $V_{oc}^{(NH)}$ depends only on J_{0n}, that is, the carrier selectivity. In the latter region, $V_{oc}^{(NH)}$ depends on the contact selectivity.

The gold contact in Fig. 15 is clearly in the region where $V_{oc}^{(NH)}$ depends only on J_{0n}; the spiro-OMeTAD-modified contacts also remain essentially within this region. This

means that the primary reason that spiro-OMeTAD affects the $V_{oc}^{(NH)}$ in the IBC cell is a change in J_{0n}. In Fig. 15, one can move from the $V_{oc}^{(NH)}$ of the gold contact to the $V_{oc}^{(NH)}$ value of any one of the spiro-OMeTAD contacts simply by changing J_{0n} alone to move to the proper contour. Changing J_{0p} has little to no additional effect on V_{oc}. In other words, all the contacts to the IBC cell studied herein as hole contacts are approximated by eq. 2.3, reproduced here:

$$V_{oc}^{(NH)} = \frac{kT}{q} ln\left(\frac{J_L}{J_{0n}}\right) \tag{4.1}$$

where the J_{0n} is that of the spiro-OMeTAD-modified gold contact. The V_{oc} for the cell with the contact under study serving as the hole contact is determined by the rate of electron collection, and Li-TFSI and air exposure reduce the J_{0n} of spiro-OMeTAD-modified gold contacts by up to about three orders of magnitude, depending on the level of oxidation determined by the amount of air exposure. This oxidation process generates spiro-OMeTAD$^{\bullet+}$ as a "p-doping" mechanism,[18] resulting in the observed increase in J_{0p}/J_{0n}.

The fact that spiro-OMeTAD significantly reduces $(J_{0n}J_{0p})^{0.5}$ relative to gold indicates that the change is not simply a work function effect at a metal/semiconductor-like interface, but that the κ values also change due to the introduction of band offsets that present additional charge transfer or tunneling barriers. The spiro-OMeTAD layer itself is responsible for an overall reduction in $(J_{0n}J_{0p})^{0.5}$ as evidenced by all the IFLs falling on a similar $(J_{0n}J_{0p})^{0.5}$ contour in Fig. 15. The addition of Li-TFSI and air tunes the J_{0p}/J_{0n} along this constant $(J_{0n}J_{0p})^{0.5}$ contour *the same way as changing the effective work function* of the combined IFL/gold contact. The change in J_{0p}/J_{0n} from neat spiro-OMeTAD to air-oxidized with Li-TFSI corresponds to a change in the barrier height ($\Delta\phi_b$) of about 0.19 V.

Spiro-OMeTAD changes both the contact selectivity and $(J_{0n}J_{0p})^{0.5}$, but we reiterate that the $V_{oc}^{(NH)}$ of the cells studied herein does not depend directly on these quantities. Rather, the $V_{oc}^{(NH)}$ depends only on the rate of electron collection (J_{0n}) as quantified by eq. 4.1. To better understand the origin of eq. 4.1, which is ubiquitous in solar cell physics, and its relations to selectivity and recombination, it is helpful to summarize how, in general, contacts can limit the V_{oc} of a solar cell. This description is based on recent theoretical work by our group[2,3] and others;[14,51-57] more details may be found there and in section II.II which provides a detailed overview of the theory developed by our group. Here, a brief summary is provided to facilitate discussion of the results presented above.

To start, we consider two different types of selectivity: contact and carrier. We defined contact selectivity above as the ratio of the J_0 values of the two carriers at *one contact*, *e.g.*, the hole contact selectivity $S_{con} = J_{0p}/J_{0n}$. Carrier selectivity (S_{car}) is instead the ratio of the J_0 values of the *same carrier* at the two contacts. For example, the electron carrier selectivity is defined as $S_{car,n} = J_{0n}^{(N)}/J_{0n}$. While S_{con} is useful in characterizing the J_0 values at a contact, the carrier selectivity is more important to the current density-voltage ($J(V)$) behavior because it describes the asymmetry available to support the QFLS in the cell.

The $J(V)$ behavior of a contact-limited solar cell depends on the carrier selectivity of both the electron and hole, but one typically dominates in the power quadrant. When, for example, the electron is limiting and J_L is greater than J_{0n} at both contacts, the V_{oc} is given by $(kT/q)\ln(S_{car,n})$. When J_L is between J_{0n} at the electron contact and J_{0n} at the top contact, there is excess carrier asymmetry in the system, and the contact-limited V_{oc} is given by $(kT/q)\ln(J_L/J_{0n})$. Herein, we refer to this latter situation as a light-limited carrier

selectivity. If a cell is limited by contact recombination rather than by carrier selectivity, the V_{oc} is given by the QFLS/q. When considering a cell with QFLS limited by recombination at the hole contact, $V_{oc} = (kT/q)\ln(J_L/((J_{0n}J_{0p})^{0.5}))$ when $J_L > J_{0p} > J_{0n}$ and $V_{oc} = (kT/q)\ln(J_L/J_{0n})$ when $J_{0p} > J_L > J_{0n}$. The two expressions come from recombination being second order *vs.* quasi-first order, respectively. Note that the latter yields the same expression as the light-limited carrier asymmetry expression, namely eq. 4.1.

The IBC cell measurements demonstrate that carrier collection asymmetry can be equally important as recombination in determining the impact of spiro-OMeTAD on V_{oc}. Although eq. 4.1 can hold in either case, the observation that the QFLS is always significantly greater than qV_{oc} for the cells studied herein shows that the V_{oc} is determined by the light-limited carrier selectivity. Though the spiro-OMeTAD-containing cells are not limited by contact recombination, the observed changes in QFLS demonstrate that spiro-OMeTAD IFLs do passivate the gold electrode to recombination. The effect, however, is much smaller than on the light-limited carrier selectivity.

Reducing contact recombination is often argued to be the primary mechanism by which spiro-OMeTAD increases the V_{oc} by as much as 400 mV in perovskite and SSDS solar cells.[19,21-23] However, herein the QFLS/q increases at most 40 mV in response to an almost four order-of-magnitude reduction in $(J_{0n}J_{0p})^{0.5}$. This is partly because the full recombination effect of the gold electrode is limited by the bulk transport rates of both carriers to the interface, evidenced by the curvature of the simulation data in Fig. 11 at low values of $I_{sc}^{(PN)}$. This curving over shows that a further increase in $(J_{0n}J_{0p})^{0.5}$ eventually results in no change in $I_{sc}^{(PN)}$ and hence no further reduction in the QFLS. The $(J_{0n}J_{0p})^{0.5}$ value for the gold contact puts it well into the bulk transport-limited regime, and similar

bulk effects would be expected to limit the impact of contact recombination in other absorbers as well.[11] In general, we expect that large increases in V_{oc} well below the radiative limit are due to the effect of spiro-OMeTAD on the light-limited carrier asymmetry rather than on recombination. However, changes in the V_{oc} of cells that already have a relatively large V_{oc} could certainly be due to modifications to spiro-OMeTAD (*e.g.*, Li-TFSI-induced oxidation) that affect $(J_{0n}J_{0p})^{0.5}$, *i.e.*, recombination.

The discussion above highlights two important points about the role of selectivity in determining the V_{oc}. First, it is natural to separate the ideas of selectivity and recombination rather than thinking of recombination as a method to achieve selectivity, unlike what is commonly done in the literature.[29] This is perhaps a semantic argument, but the distinct roles of the QFLS and carrier collection asymmetry in determining V_{oc} provide a natural basis for separating them. Second, altering the collection rate of the undesired carrier can be seen as either a selectivity or recombination effect. The impact of spiro-OMeTAD on collecting the undesired carrier has been previously recognized from impedance and transient photovoltage measurements on perovskite and SSDS cells[17,18,28] and is often informally associated with qualitative ideas of recombination. The emphasis on recombination is understandable because the earliest form of eq. 4.1 is that derived from the classic treatment of radiative recombination,[13] with J_{0n} replaced with a J_0 quantifying the radiative recombination rate. However, the collection rate of the undesired carrier also contributes to the carrier selectivity (as defined herein), which can limit the qV_{oc} to less than the recombination-determined QFLS. The J_{0n} also alters the contact selectivity, but this is not as important to the $J(V)$ behavior of a contact-limited solar cell as the carrier selectivity.

The correlation of J_{0p}/J_{0n}, $(J_{0n}J_{0p})^{0.5}$, or the individual J_0 values with a property such as V_{oc} as in Fig. 15 illustrates two additional important points. First, any measure of a contact property alone cannot provide a complete picture of the performance of an entire solar cell. That is, the J_0 values shown in Fig. 15 are characteristics of the contact, but the underlying contour plot that describes how they impact a cell-level property such as V_{oc} depends on the properties of both contacts, the absorber, and the geometry of the cell. Both contacts are important because they define the carrier collection asymmetry necessary to achieve a photovoltaic effect and recombination anywhere in the cell limits the QFLS that can be obtained and ultimately harnessed to generate power. Second, it is difficult to determine the action of an IFL on a contact from measuring the V_{oc} of a solar cell. An excellent example comes from considering the Li-TFSI-containing samples herein. After extended air exposure (t = ~350 min in Fig. 3), the introduction of Li-TFSI-containing spiro-OMeTAD has almost no effect on $V_{oc}^{(NH)}$ (compare $V_{oc}^{(NH,Au)}$ and $V_{oc}^{(NH,Li-TFSI)}$ at t = 350 in Fig. 13). Thus, one might suspect there is little work function modification or little general impact on charge transfer. Inspection of Fig. 15, however, shows this is not the case. The fact that the $V_{oc}^{(NH)}$ remains unchanged is a consequence of a cancellation of the effect on J_{0p}/J_{0n}, a "work function effect", and a reduction in contact recombination $(J_{0n}J_{0p})^{0.5}$. The result is no change in J_{0n}, which in this case is the relevant J_0 in the region where the contacts operate. A simple measurement of the V_{oc} such as in many studies of IFL-modified contacts[17-28] does not capture these important fundamental properties.

In summary, this chapter shows the effect of spiro-OMeTAD on the selectivity, recombination, and charge transfer characteristics of gold contacts to IBC cells. Further, it illustrates how changes in these properties due to the presence of spiro-OMeTAD and its

additive Li-TFSI affect the V_{oc} when the spiro-OMeTAD-modified gold contact acts as the hole contact. While the addition of spiro-OMeTAD changes both the contact selectivity and recombination compared to bare gold, we find that changes in the light-limited carrier selectivity, as demonstrated by changes in J_{0n} in this case, are directly responsible for the observed changes in V_{oc} in the regime where these contacts operate. These findings answer questions both about the precise relationships between selectivity, recombination, charge transfer, and V_{oc} and about the specific role of spiro-OMeTAD and its additive Li-TFSI in dictating contact and overall solar cell properties.

CHAPTER V

IMPACT OF CO-TFSI IN SPIRO-OMETAD ON THE CHARGE TRANSFER PROPERTIES OF GOLD CONTACTS

This chapter presents results on the impact of Co(III) salts on the selectivity, recombination, and charge transfer characteristics of spiro-OMeTAD-modified gold contacts and the relation of these characteristics to the V_{oc} when spiro-OMeTAD-modified gold acts as the hole contact. This is material both in preparation for publication[4] and unpublished. As previously discussed in sections II.II, III.III, IV.I, and IV.II, simulation and experimental IBC cell results are used to extract charge transfer (J_0) values of the contacts under study. For more details about this process, please refer to those sections.

I. Lingering questions about the role of Co(III) salts in spiro-OMeTAD

In the previous chapter we showed the effects of Li-TFSI in spiro-OMeTAD-modified gold contacts on the selectivity, recombination, and charge transfer properties and on the V_{oc} when spiro-OMeTAD-modified gold contacts act as the hole contact (refer to section IV.II for more details). However, the most common spiro-OMeTAD "recipes" used in perovskite solar cells incorporate Co(III) complexes in addition to Li-TFSI.[20,24,28,42-46] Thus, a comprehensive understanding of how the addition of Co(III) salts affects charge transfer and photovoltaic performance is necessary to both optimize its use and potentially open new avenues for IFL engineering. While the effects of Co(III) salts on the performance characteristics of complete solar cells has been investigated,[42-46] their direct impact on the charge transfer, selectivity, and recombination properties of contacts and how changes in those characteristics due to the presence of Co(III) could impact

performance remain unknown. A more detailed description of what is known about the effects of Co(III) is presented in section I.IV. What follows is a brief summary.

While UV-Vis studies show that Co(III) salts produce the same spectroscopic indications of oxidation when added to spiro-OMeTAD solutions[42-44] as Li-TFSI and air exposure (*i.e.*, Li-TFSI and oxygen react to produce superoxide, which then oxidizes neutral spiro-OMeTAD to spiro-OMeTAD$^{\bullet+}$[18]), there is no direct evidence that these changes are responsible for observed changes in contact and overall solar cell properties when Co(III) salts are used in spiro-OMeTAD films. In fact, there is some evidence in the literature that suggests the impact of Co(III) on the chemistry of spiro-OMeTAD films may be different from that of Li-TFSI. For example, Burschka *et al*. found that the conductivity of spiro-OMeTAD films with Co(III) salt was lower than spiro-OMeTAD films with Li-TFSI.[43] If the effect of Co(III) on the chemistry of spiro-OMeTAD were the same as Li-TFSI, one would hypothesize the same conductivity properties in the presence of both salts due to the generation of spiro-OMeTAD$^{\bullet+}$. Differences in conductivity, therefore, may suggest generation of different species or complexes which could contribute more to the properties of the film than spiro-OMeTAD$^{\bullet+}$.

Additionally, in a recent study, Saygili *et al.* showed that the oxidation mechanism of spiro-OMeTAD in the presence of $Zn(TFSI)_2$ is different than that induced by Li-TFSI.[63] Because Co^{3+} is significantly more reactive than Li^+,[64] and Co(III) complexes also contain ligands unlike either Li-TFSI or $Zn(TFSI)_2$, it is possible that it could cause different chemistry to occur like in the case of $Zn(TFSI)_2$ and thus could impact contact properties differently. By measuring J_{0n}, J_{0p}, and $V_{oc}^{(NH)}$, this study investigates the role of the Co(III) salt tris(2-(1*H*-pyrazol-1-yl)pyridine) cobalt(III) tri[bis(trifluoromethane)sulfonimide]

(herein referred to as Co-TFSI) in contributing to charge transfer properties of spiro-OMeTAD-modified gold contacts and therefore to solar cell performance. Because we observed changes in contact hole selectivity of Li-TFSI-containing spiro-OMeTAD-modified gold contacts due to the generation of spiro-OMeTAD$^{\bullet+}$ over time in air, the contact hole selectivity (J_{0p}/J_{0n}) in particular could help determine the impact of Co-TFSI on the chemistry of spiro-OMeTAD IFLs.

II. Impact of Co-TFSI on selectivity, recombination, charge transfer, and $V_{oc}^{(NH)}$

In this study, the impact of Co-TFSI salt at 1:10 and 1:5 mole ratio to spiro-OMeTAD in spiro-OMeTAD-modified gold contacts was studied. Figure 16 shows the results of measuring the J_0 values for these contacts with various Co-TFSI concentrations

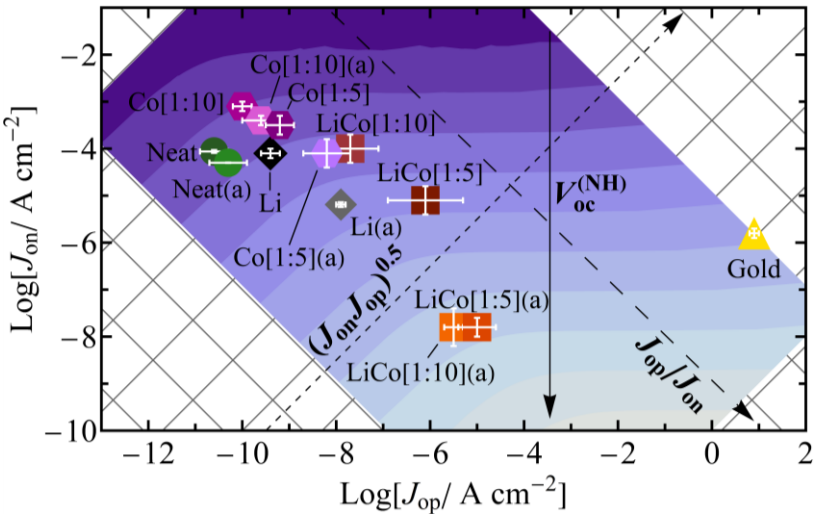

$V_{oc}^{(NH)}$ [V]	
Gold	0.285(5)
Neat	0.12(1)
Neat(a)	0.13(1)
Co[1:10]	0.09(1)
Co[1:10](a)	0.12(2)
Co[1:5]	0.13(1)
Co[1:5](a)	0.17(2)
Li	0.14(1)
Li(a)	0.223(6)
LiCo[1:10]	0.16(3)
LiCo[1:10](a)	0.37(2)
LiCo[1:5]	0.24(2)
LiCo[1:5](a)	0.37(2)

Fig. 16. Experimental J_0 values for spiro-OMeTAD-modified gold contacts with different salt additives and concentrations. If present, the concentration of Li-TFSI is always 1:4 mole ratio to spiro-OMeTAD. Gold triangle = unmodified gold, green circles = neat spiro-OMeTAD, gray diamonds = Li-TFSI at 1:4 mole ratio to spiro-OMeTAD only, pink hexagons = Co-TFSI at 1:10 only, purple hexagons = Co-TFSI at 1:5 only, orange squares = Li-TFSI at 1:4 and Co-TFSI at 1:10, and red squares = Li-TFSI at 1:4 and Co-TFSI at 1:5. In sample names, (a) refers to the values after six hours of air exposure. The table shows the magnitudes of $V_{oc}^{(NH)}$ for each case.

with and without Li-TFSI (always at 1:4 mole ratio to spiro-OMeTAD) while the accompanying $V_{oc}^{(NH)}$ values are tabulated. The background grid and blue contour plot are reproduced from Fig. 15. As a brief summary, the grid corresponds to systematic variations in either J_{0p}/J_{0n} (which increases from top left to bottom right) and $(J_{0n}J_{0p})^{0.5}$ (which increases from bottom left top right) while the blue scale contour plot shows how the $V_{oc}^{(NH)}$ depends on the J_0 values. In the region of this plot where the $V_{oc}^{(NH)}$ contours are parallel to the x axis, $V_{oc}^{(NH)}$ depends on the light-limited carrier selectivity, *i.e.*, on J_{0n} alone of the contact under study. In the region where the contours are instead parallel to the J_{0p}/J_{0n} contours, $V_{oc}^{(NH)}$ changes with changing contact selectivity. Please refer to sections III.III and IV.II for more details about this plot and the two different regimes of behavior.

Data overlaid on top of the contour plot in Fig. 16 show the changes in J_{0n} and J_{0p} when spiro-OMeTAD contains Co-TFSI at 1:10 mole ratio to spiro-OMeTAD, Co-TFSI at 1:5 mole ratio, Li-TFSI at 1:4 mole ratio, both Co-TFSI at 1:10 and Li-TFSI at 1:4 mole ratio, or both Co-TFSI at 1:5 and Li-TFSI at 1:4 mole ratio and modifies gold contacts. All films contain the same spiro-OMeTAD concentration and the same *t*-BP:spiro-OMeTAD mole ratio. The experimental $V_{oc}^{(NH)}$, $V_{oc}^{(PE)}$, and $I_{sc}^{(PN)}$ data both before and after air exposure are presented in Table 4 while the extracted J_{0n}, J_{0p}, J_{0p}/J_{0n}, and $(J_{0n}J_{0p})^{0.5}$ data are presented in Tables 5 and 6.

Overall, when spiro-OMeTAD with *t*-BP (*i.e.*, "neat") modifies a gold contact, it decreases the recombination by about four and a half orders of magnitude. When salts are added to the spiro-OMeTAD film, the recombination ($(J_{0n}J_{0p})^{0.5}$) decreases by half an order of magnitude, regardless of which salts, at what concentration, and in what combinations.

Table 4. Experimental $V_{oc}^{(NH)}$, $V_{oc}^{(PE)}$, and $I_{sc}^{(PN)}$ of mixtures studied, measured using the IBC cell. Amounts of Li-TFSI and Co-TFSI are given in mole ratio relative to spiro-OMeTAD. All samples contain the same spiro-OMeTAD concentration and same *t*-BP:spiro-OMeTAD mole ratio.

			$V_{oc}^{(NH)}$		$V_{oc}^{(PE)}$		$I_{sc}^{(PN)}$	
Sample	Li-TFSI	Co-TFSI	Initial	Final	Initial	Final	Initial	Final
Gold	-	-	0.283(4)	0.285(5)	0.247(3)	0.245(3)	1.76(5)	1.75(5)
Spiro	-	-	0.12(1)	0.13(1)	0.46(1)	0.45(1)	2.48(5)	2.47(7)
Spiro, Li-TFSI	1:4	-	0.14(1)	0.223(6)	0.43(1)	0.339(5)	2.24(3)	2.10(2)
Spiro, Co-TFSI	-	1:10	0.09(1)	0.12(2)	0.47(1)	0.45(1)	2.13(3)	2.10(7)
Spiro, Co-TFSI	-	1:5	0.13(1)	0.17(2)	0.43(2)	0.38(2)	1.98(4)	1.90(4)
Spiro, Li-TFSI, Co-TFSI	1:4	1:10	0.16(3)	0.37(2)	0.36(3)	0.19(2)	1.80(1)	2.18(5)
Spiro, Li-TFSI, Co-TFSI	1:4	1:5	0.24(2)	0.37(2)	0.30(2)	0.18(2)	1.77(2)	2.02(6)

Further, when salts are added, the contact hole selectivity increases with increasing total salt concentration, from quite electron selective for neat films and films with Co-TFSI only to significantly more hole selective for contacts modified with spiro-OMeTAD containing both Li- and Co-TFSI.

To more clearly illustrate the impact of adding Co-TFSI in different concentrations

Table 5. Initial (before 6 hours of air exposure) J_0 values for samples with varying amounts of Li- and Co-TFSI. Amounts of Li-TFSI and Co-TFSI are given in mole ratio relative to spiro-OMeTAD. All samples contain the same spiro-OMeTAD concentration and same *t*-BP:spiro-OMeTAD mole ratio.

Sample	Li-TFSI	Co-TFSI	Log(J_{0n})	Log(J_{0p})	Log(J_{0p}/J_{0n})	Log($(J_{0n}J_{0p})^{0.5}$)
Gold	-	-	-5.7(1)	0.8(1)	6.5(2)	-2.5(2)
Spiro	-	-	-4.06(3)	-10.6(3)	-6.5(4)	-7.3(1)
Spiro, Li-TFSI	1:4	-	-4.1(1)	-9.4(2)	-5.4(3)	-6.76(5)
Spiro, Co-TFSI	-	1:10	-3.1(1)	-10.0(2)	-6.9(3)	-6.58(5)
Spiro, Co-TFSI	-	1:5	-3.5(2)	-9.2(3)	-5.7(5)	-6.3(1)
Spiro, Li-TFSI, Co-TFSI	1:4	1:10	-4.0(5)	-7.7(6)	-4(1)	-5.87(5)
Spiro, Li-TFSI, Co-TFSI	1:4	1:5	-5.1(3)	-6.1(8)	-1(1)	-5.6(3)

Table 6. Final (after 6 hours of air exposure) J_0 values for samples with varying amounts of Li- and Co-TFSI. Amounts of Li-TFSI and Co-TFSI are given in mole ratio relative to spiro-OMeTAD. All samples contain the same spiro-OMeTAD concentration and same *t*-BP:spiro-OMeTAD mole ratio.

Sample	Li-TFSI	Co-TFSI	Log(J_{0n})	Log(J_{0p})	Log(J_{0p}/J_{0n})	Log($(J_{0n}J_{0p})^{0.5}$)
Gold	-	-	-5.8(1)	0.9(1)	6.6(2)	-2.5(2)
Spiro	-	-	-4.274(4)	-10.3(4)	-6.0(4)	-7.3(2)
Spiro, Li-TFSI	1:4	-	-5.19(5)	-7.9(1)	-2.7(2)	-6.53(3)
Spiro, Co-TFSI	-	1:10	-3.4(1)	-9.6(4)	-6.2(5)	-6.5(1)
Spiro, Co-TFSI	-	1:5	-4.1(3)	-8.2(5)	-4.1(9)	-6.2(1)
Spiro, Li-TFSI, Co-TFSI	1:4	1:10	-7.8(4)	-5.5(2)	2.4(7)	-6.7(1)
Spiro, Li-TFSI, Co-TFSI	1:4	1:10	-7.8(2)	-5.0(4)	2.7(7)	-6.4(1)

and with *vs.* without Li-TFSI also present, the rest of this chapter primarily investigates the results presented in Fig. 16 in more detail. Figure 17 shows the specific effect of the different salt concentrations on the charge transfer properties compared to neat spiro-OMeTAD. The data represent measurements taken after six hours of air exposure and accompanying changes in $V_{oc}^{(NH)}$ are presented in the table (the effects of air exposure itself will be discussed further below).

The first important note is that the neat spiro-OMeTAD-modified gold contacts shown in Fig. 17 contain *t*-BP, unlike those presented in Chapter IV. Neat samples in this study include *t*-BP because we wish to understand exactly the impact of adding *just* the Li- or/and Co-TFSI salt to the spiro-OMeTAD. Because all films with salts must contain *t*-BP in order to produce smooth, amorphous films, we also use it in neat spiro-OMeTAD in this study for the sake of comparison. While this does not impact the contact selectivity (see section IV.II for the J_0 values of neat spiro-OMeTAD-modified gold contacts without *t*-BP), it does decrease contact recombination by about half an order of magnitude. The most important result of this change is that neat spiro-OMeTAD-modified gold contacts in this

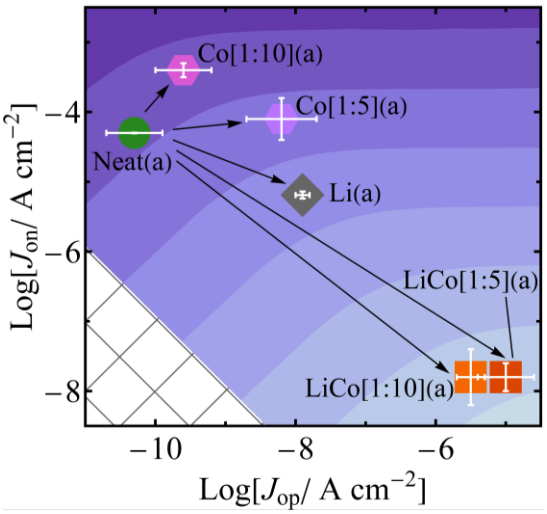

Change	$\Delta V_{oc}^{(NH)}$ [V]
Neat(a) → Co[1:10](a)	-0.01(2)
Neat(a) → Co[1:5](a)	0.04(2)
Neat(a) → Li[1:4](a)	0.09(1)
Neat(a) → LiCo[1:10](a)	0.24(2)
Neat(a) → LiCo[1:5](a)	0.24(2)

Fig. 17. Changes to experimental J_0 values and accompanying changes in $V_{oc}^{(NH)}$ (tabulated) due to adding different salt combinations to neat spiro-OMeTAD, shown after air exposure. Green circle = neat spiro-OMeTAD, gray diamond = Li-TFSI at 1:4 mole ratio to spiro-OMeTAD, pink hexagon = Co-TFSI at 1:10 mole ratio, purple hexagon = Co-TFSI at 1:5 mole ratio, orange square = Li-TFSI at 1:4 and Co-TFSI at 1:10, and red square = Li-TFSI at 1:4 and Co-TFSI at 1:5 mole ratio to spiro-OMeTAD.

study operate in the regime where the $V_{oc}^{(NH)}$ depends on contact selectivity as opposed to J_{0n} alone (discussed in more detail in sections III.III and IV.II). This means that when salts are added, changes in $V_{oc}^{(NH)}$ only occur if the contact selectivity changes.

As shown in Fig. 17, the addition of salts, independent of mixture and concentration, causes the contact recombination to increase by about half an order of magnitude compared to neat spiro-OMeTAD-modified gold. However, because the neat spiro-OMeTAD-modified contacts operate in the regime where $V_{oc}^{(NH)}$ depends on contact selectivity, there are no direct implications for performance of these increases in recombination for the spiro-OMeTAD-modified gold contacts in the IBC cells we study. At the same time, these results are still useful because they illustrate how the addition of salt impacts recombination. For cells limited by contact recombination, this would be valuable information to optimize IFL-modified contacts for performance improvements of

those photovoltaics.

For these IFL-modified contacts, changes to contact selectivity when salts are added are those that impact performance. When Co-TFSI alone is added to the spiro-OMeTAD film, we see small changes if any to the contact hole selectivity. In fact, films with Co-TFSI only (both 1:10 and 1:5 mole ratio to spiro-OMeTAD), are similar in contact selectivity to contacts modified with films with no salt at all. Samples with Co-TFSI at 1:5 mole ration demonstrate a slight increase in contact hole selectivity while those with 1:10 mole ratio demonstrate no increase at all. The small increase in contact hole selectivity for films with Co-TFSI at 1:5 mole ratio compared to when no salts are present results in a slight increase in the $V_{oc}^{(NH)}$ (~40 mV) while the lack of change in contact selectivity upon addition of Co-TFSI at 1:10 mole ratio means there is no increase in the $V_{oc}^{(NH)}$ compared to neat.

These results are surprising given the spectroscopic evidence in the literature[42-44] showing the facile oxidation of spiro-OMeTAD in the presence of Co-TFSI. In general, when spiro-OMeTAD becomes oxidized the color changes from light yellow (neutral spiro-OMeTAD absorbs at about 390 nm) to pink/red, accompanied by a peak in the visible spectrum at about 520 nm.[18] This peak is attributed to spiro-OMeTAD$^{\bullet+}$ as it is generated in the presence of Li-TFSI and air.[18] Recent studies have also shown that Co(III) salts generate this same absorbance peak both in the absence of air and at low concentrations compared to Li-TFSI.[42-44] These results suggest that Co(III) salts oxidize spiro-OMeTAD in the same manner as Li-TFSI and at much lower concentrations. Further, as shown in Figure 18, we observe significant color change when adding Co-TFSI salt to spiro-OMeTAD solution, even in the absence of air, indicating a large concentration of spiro-

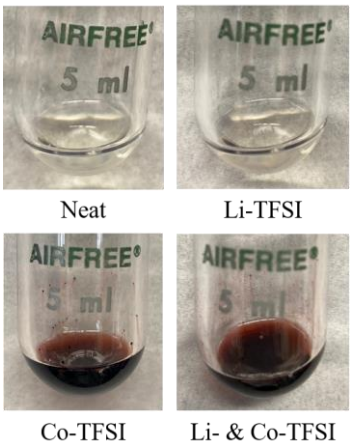

Fig. 18. Color changes induced by adding salts to neat spiro-OMeTAD solution under air free conditions.

OMeTAD$^{\bullet+}$ (for spectroscopic studies, refer to section VI.III).

Thus, we hypothesized the addition of Co-TFSI would cause the hole contact selectivity to increase significantly, regardless of concentration, but, as discussed above, this is not what we observe. While we might predict lower total salt concentrations in general would lead to lower contact hole selectivity, both the results presented in the literature[42-44] and the color changes observed indicate that there is significantly more spiro-OMeTAD$^{\bullet+}$ generated by Co-TFSI at 1:10 mole ratio than by Li-TFSI at 1:4 mole ratio (*i.e.*, when Co-TFSI is present at a lower concentration). The lack of change in contact hole selectivity, then, indicates that the formation of spiro-OMeTAD$^{\bullet+}$ may not dictate the contact properties when Co-TFSI alone is used. This in turn suggests that some other chemistry – perhaps involving the ligands of the Co-TFSI complex or/and *t*-BP – may compete with spiro-OMeTAD$^{\bullet+}$ formation to determine the properties of the IFL-modified contact when Co-TFSI is the only salt present.

When Li-TFSI alone is added to the spiro-OMeTAD film, we see a larger change in contact hole selectivity than when Co-TFSI alone is added. The J_{0p}/J_{0n} increases by about three orders of magnitude, resulting in an increase in $V_{oc}^{(NH)}$ of about 90 mV compared to

neat. Further, when both salts are added, the contact hole selectivity increases significantly more than when either salt is added alone, regardless of Co-TFSI concentration. In fact, the end result is independent of Co-TFSI concentration. The contact hole selectivity increases by almost nine orders of magnitude compared to when no salt is present, accompanied by an increase in $V_{oc}^{(NH)}$ of about 240 mV.

The changes in both contact hole selectivity and $V_{oc}^{(NH)}$ when both salts are present are more than additive. That is, the changes are greater than the sum of the changes when only the individual salts are present. This finding, in conjunction with the evidence that Co-TFSI may cause different chemical changes in the spiro-OMeTAD film than Li-TFSI, suggests that the chemistry occurring in the presence of Co-TFSI could promote the oxidation of spiro-OMeTAD by Li-TFSI to cause larger changes in the properties of spiro-OMeTAD-modified contacts than when only one salt or the other is present.

To further investigate these phenomena, the effects of air exposure on the properties of contacts modified with Co-TFSI-containing spiro-OMeTAD were probed. Figure 19 shows the changes that occur over six hours of air exposure for the same spiro-OMeTAD-modified gold contacts as those presented above. The accompanying table presents the shifts in $V_{oc}^{(NH)}$ that occur in parallel. Salted spiro-OMeTAD-modified gold contacts all operate in the regime where $V_{oc}^{(NH)}$ depends on only J_{0n}. However, changes to contact selectivity reflect changes in J_{0n} to a certain degree and provide some additional insight about chemical changes occurring in the spiro-OMeTAD films. Thus, the following discussion focuses on contact selectivity as a means of understanding changes in chemistry. At the same time, we emphasize that the changes in $V_{oc}^{(NH)}$ due to air exposure for these

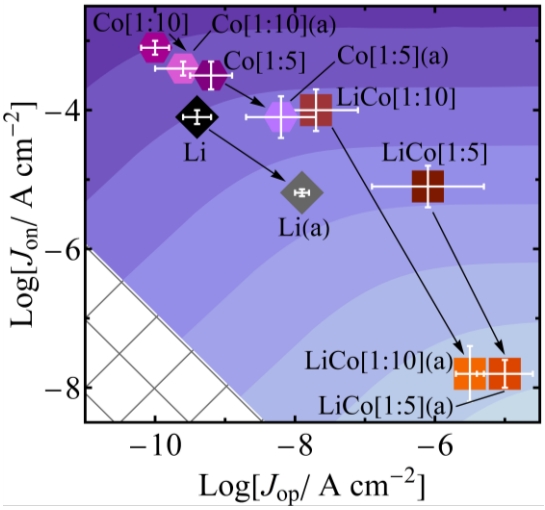

Change	$\Delta V_{oc}^{(NH)}$ [V]
Co[1:10] → Co[1:10](a)	0.03(2)
Co[1:5] → Co[1:5](a)	0.04(2)
Li → Li(a)	0.08(1)
LiCo[1:10] → LiCo[1:10](a)	0.21(4)
LiCo[1:5] → LiCo[1:5](a)	0.13(3)

Fig. 19. Changes in experimental J_0 values and accompanying changes in $V_{oc}^{(NH)}$ (tabulated) due to air exposure for different salt combinations in spiro-OMeTAD-modified gold contacts. Black/gray diamonds = Li-TFSI at 1:4 mole ratio to spiro-OMeTAD, pink hexagons = Co-TFSI at 1:10, purple hexagons = Co-TFSI at 1:5, orange squares = Li-TFSI at 1:4 and Co-TFSI at 1:10, and red squares = Li-TFSI at 1:4 and Co-TFSI at 1:5 mole ratio.

contacts are specifically due to changes in J_{0n}.

We find that samples with Co-TFSI only experience small changes in charge transfer properties (specifically, there is little change in contact selectivity) and $V_{oc}^{(NH)}$ over time in air compared to those with Li-TFSI or both salts. Further, the changes in $V_{oc}^{(NH)}$ due to air exposure that occur when Co-TFSI alone is present are the same for both concentrations. The small changes in contact selectivity upon air exposure could be due to most of the Co(III) being converted to Co(II)[43] through Co(III)-induced oxidation of spiro-OMeTAD in solution before the film is even made (as suggested by the color change). Co(II) does not oxidize spiro-OMeTAD,[43] thus little additional spiro-OMeTAD$^{\bullet+}$ would be generated upon film deposition and exposure to air, resulting in little change in the contact selectivity. Further, the oxidation of spiro-OMeTAD by Co-TFSI does not depend on the presence of oxygen, unlike Li-TFSI-induced oxidation. While this does not mean Co(III)

would not oxidize spiro-OMeTAD in air, it could help explain the results.

When Li-TFSI alone is used, the contact hole selectivity increases by about three orders of magnitude due to air exposure, likely due to the generation of spiro-OMeTAD$^{\bullet+}$, accompanied by an increase in $V_{oc}^{(NH)}$ of about 80 mV. When both salts are present there are significant changes in the J_{0p}/J_{0n} and $V_{oc}^{(NH)}$ due to air exposure. The contact hole selectivity increases by about six and four orders of magnitude for Co-TFSI at 1:10 and 1:5 mole ratio to spiro-OMeTAD, respectively, and $V_{oc}^{(NH)}$ increases by more than 200 and more than 100 mV, respectively. There is less change when the Co-TFSI concentration is higher, in this case because the contact hole selectivity is higher at the initial time point for samples with Co-TFSI at 1:5 mole ratio to spiro-OMeTAD, likely due to a greater degree of oxidation before the first measurement is taken. The greater change over time in air compared to films with only one salt could simply be due to the overall higher salt concentration but, again, because the changes are more than additive, they could also be due to interactions between different species in the film (or in the solution before the film is even deposited), or all of the above. To further probe how these effects might be related to changes in film chemistry, the role of the other additive – *t*-BP – was investigated, the results of which are presented in Chapter VI.

In summary, the quantitative effects of Co-TFSI when used in spiro-OMeTAD-modified gold contacts on selectivity, recombination, charge transfer, and $V_{oc}^{(NH)}$ were shown. While Co-TFSI causes striking color changes when added to spiro-OMeTAD solutions, suggesting the formation of spiro-OMeTAD$^{\bullet+}$ both with and without Li-TFSI, the charge transfer properties when it is used alone do not reflect the idea that spiro-OMeTAD$^{\bullet+}$ causes the contact hole selectivity to change as we originally observed with

Li-TFSI alone. That is, our results suggest that the properties of spiro-OMeTAD-modified gold contacts with Co-TFSI only may not be dictated by the generation of spiro-OMeTAD$^{\bullet+}$ but rather by other possible interactions occurring due to the presence of Co-TFSI.

Further, there are more-than-additive effects on charge transfer and $V_{oc}^{(NH)}$ when both Co- and Li-TFSI are used compared to only one or the other, indicating a likely synergistic effect of using both salts. Because the effects are more than additive, it seems unlikely that these effects are simply due to increased overall salt concentration. Alternatively, Co-TFSI-caused interactions between species present in solution and/or in the film could instead promote Li-TFSI-induced spiro-OMeTAD$^{\bullet+}$ formation compared to when Co-TFSI is not present. To further investigate these possibilities, the role of *t*-BP as the final component of these films – and its potential interactions with other film components – is presented in Chapter VI.

CHAPTER VI

IMACT OF *t*-BP IN SPIRO-OMETAD ON THE CHARGE TRANSFER PROPERTIES OF GOLD CONTACTS

This chapter presents results on the impact of *tert*-butyl pyridine (*t*-BP) on the selectivity, recombination, and charge transfer characteristics of spiro-OMeTAD-modified gold contacts and the relation of these characteristics to the V_{oc} when spiro-OMeTAD-modified gold acts as the hole contact. This is material both in preparation for publication[4] and unpublished. As previously discussed in sections II.II, III.III, IV.I, and IV.II, simulation results and experimental IBC cell results are used to extract charge transfer (J_0) values of the contacts under study in this work. Further, the impact of Li- and Co-TFSI on the properties of spiro-OMeTAD-modified contacts are inextricably tied to the effects of *t*-BP and are discussed in Chapters IV and V. For more details about those additives or for more details about experiments and simulations, please refer to those chapters/sections.

I. Lingering questions about the role of *t*-BP in spiro-OMeTAD

In Chapters IV and V we showed the effects of two Spiro-OMeTAD dopants, Li- and Co-TFSI, on the selectivity, recombination, and charge transfer properties of gold contacts to IBC cells and on the V_{oc} when the spiro-OMeTAD-modified gold contact acts as the hole contact. Here, we investigate the effects of the third common additive to spiro-OMeTAD, *t*-BP, and its potential interaction with other species in solution or in films, on the same properties of spiro-OMeTAD-modified gold contacts. The primary purpose of *t*-BP is to control film morphology[18,39,40,47] but more recent studies have shown it could have an impact on other aspects of spiro-OMeTAD chemistry as well.[40,41]

Studies have shown that Co(III) salts oxidize spiro-OMeTAD to spiro-OMeTAD$^{\bullet+}$ in the same way as Li-TFSI and exposure to oxygen using visible spectroscopy.[18,42-44] Lamberti *et al.* more recently used electron paramagnetic resonance spectroscopy (EPR) to measure the radical character of spiro-OMeTAD doped with Li-TFSI.[41] Simultaneously, they showed that the radical character of spiro-OMeTAD depends on the concentration of *t*-BP. This led them to conclude that *t*-BP quenches spiro-OMeTAD$^{\bullet+}$ generated in the presence of Li-TFSI and oxygen,[41] proposing a mechanism where the lone pair electrons on nitrogen in *t*-BP react with spiro-OMeTAD$^{\bullet+}$ to neutralize it. At the same time, the interaction between Li^+ of Li-TFSI and *t*-BP has also been proposed to contribute to the chemistry of spiro-OMeTAD films.[40] Wang *et al.* proposed a mechanism where Li^+ attracts the lone pair electrons of nitrogen on four *t*-BP molecules, complexing *t*-BP as it would water.[40] This phenomenon would lead to less spiro-OMeTAD$^{\bullet+}$ formation to begin with because Li^+ is less available to promote the oxidation of spiro-OMeTAD. Thus, decreasing the *t*-BP concentration would lead to higher spiro-OMeTAD$^{\bullet+}$ concentrations because it would cause Li^+ to be more available. It is possible these two phenomena occur in parallel, and the addition of Co(III) salts to the mixture likely adds even more complexity.

The results presented in section IV.II show that the contact hole selectivity of spiro-OMeTAD-modified gold contacts with Li-TFSI increases due to air exposure. This phenomenon is likely due to the generation of spiro-OMeTAD$^{\bullet+}$. Even larger increases in contact hole selectivity are observed when both Co- and Li-TFSI are used, as shown in section V.II, very likely indicating significant generation of spiro-OMeTAD$^{\bullet+}$. While the effect of *t*-BP on spiro-OMeTAD$^{\bullet+}$ concentration in the presence of Li-TFSI alone has been investigated using EPR, the effects of *t*-BP when both Co- and Li-TFSI are present are

unknown. While we might predict that it would have similar effects because the oxidized spiro-OMeTAD species is the same, the results presented in Chapter V, namely that the contact properties of spiro-OMeTAD-modified contacts containing only Co-TFSI do not align with predictions and those with both salts demonstrate more-than-additive changes, further suggest that the role of *t*-BP may be more complicated in the presence of Co-TFSI.

More specifically, when Co-TFSI alone is used in spiro-OMeTAD, little change in contact hole selectivity is observed despite the significant change in color of the spiro-OMeTAD solution when Co-TFSI is added, even under air free conditions (refer to section V.II for more details). These observations suggest different chemical interactions occurring in the presence of Co-TFSI, perhaps due to the ligands or reaction with *t*-BP, which may compete with spiro-OMeTAD$^{\bullet+}$ to determine the observed contact properties. The synergistic effects on charge transfer and V_{oc} of using both salts further indicate that the simple formation of spiro-OMeTAD$^{\bullet+}$ in the presence of Co-TFSI may not completely describe the role of Co-TFSI in spiro-OMeTAD interfacial layers.

If this is the case, *t*-BP also likely plays a more complex role in dictating the properties of spiro-OMeTAD-modified contacts containing both Co- and Li-TFSI. This hypothesis reflects recent results that show the role of $Zn(TFSI)_2$ is different than that of Li-TFSI in the oxidation mechanism of spiro-OMeTAD.[63] In fact, *t*-BP interacts with the zinc species to form $[Zn(t\text{-BP})_3]^+(TFSI^-)$, oxidizing spiro-OMeTAD in the process. This insight with a different TFSI species and the involvement of *t*-BP in the oxidation process shows the nuances that accompany the use of salts and *t*-BP as additives in spiro-OMeTAD. It also suggests that *t*-BP could interact with Co-TFSI itself rather than or in addition to spiro-OMeTAD$^{\bullet+}$, as proposed for Li-TFSI by Wang *et al.*,[40] or with other species

altogether, which could cause differences in the charge transfer characteristics and therefore V_{oc} compared to when Li-TFSI is used.

In light of these ideas, the goal of this study is to determine the role of *t*-BP in the chemistry of spiro-OMeTAD containing Co- and Li-TFSI and in the charge transfer properties of gold contacts modified with the same. To probe the former, EPR was used to investigate the radical character of spiro-OMeTAD solutions with different salts and different *t*-BP concentrations while IBC cell measurements were used to probe the latter (for a description of how IBC cell measurements and simulation results are used to determine J_0 values, refer to sections III.I and III.III). Understanding the role of *t*-BP when both Li- and Co-TFSI is used will answer lingering questions about the impact of these additives on the properties of spiro-OMeTAD-modified contacts and on solar cell performance. This, in turn, will help the field optimize the use of spiro-OMeTAD and its additives for improved photovoltaic (particularly perovskite) efficiencies.

II. Radical character of spiro-OMeTAD solutions with Li- and Co-TFSI

To investigate the radical character of spiro-OMeTAD when Co- and/or Li-TFSI are present, EPR spectra of solutions with various salts (made in the same manner as those used to make films) were collected, as shown in Figure 20. For more experimental details, refer to Appendix A. These spectra demonstrate that Li- and Co-TFSI (at 1:4 and 1:10 mole ratio to spiro-OMeTAD, respectively) both induce radical character in spiro-OMeTAD solutions (the results presented in this chapter focus on Co-TFSI at the 1:10 mole ratio concentration because of the two concentrations presented in Chapter V it is the more relevant for real solar cells[42-46]). However, those with Li-TFSI demonstrate a much smaller

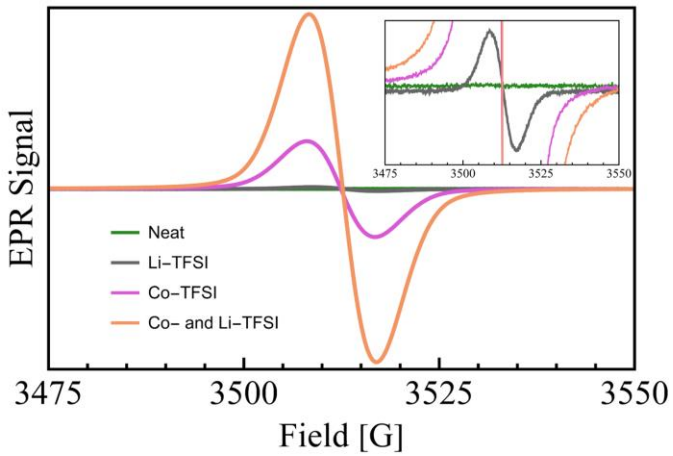

Fig. 20. Electron paramagnetic resonance spectra of spiro-OMeTAD solutions in chlorobenzene containing no salts ("Neat"), Li-TFSI at 1:4 mole ratio ("Li-TFSI"), Co-TFSI at 1:10 mole ratio ("Co-TFSI"), and both Co- and Li-TFSI at their respective concentrations ("Co- and Li-TFSI"). Spectra are magnified inset to show the Li-only solution in more detail. All solutions have the same spiro-OMeTAD concentration and also contain *t*-BP.

signal than those with Co-TFSI, indicating a smaller concentration of spiro-OMeTAD$^{\bullet+}$ even with higher salt concentration. This simply shows the same result as the color changes do: Co-TFSI induces spiro-OMeTAD$^{\bullet+}$ formation without the need for air or light exposure, unlike Li-TFSI. Further, the signal when both salts are present is substantially larger than when only Co-TFSI is present. This result reflects the synergistic change in the charge transfer properties of spiro-OMeTAD-modified gold contacts when both salts are present compared to only one or the other.

Additionally, these results indicate that if this radical character is conserved in the film deposition process, and the contact selectivity of spiro-OMeTAD-modified contacts depends on the concentration of spiro-OMeTAD$^{\bullet+}$, contacts modified with Co-TFSI-containing spiro-OMeTAD without Li-TFSI should demonstrate larger contact hole selectivity due to a higher concentration of spiro-OMeTAD$^{\bullet+}$. However, because this is not the case, other interactions between Co-TFSI, *t*-BP, and spiro-OMeTAD could occur to dominate the contact properties as previously mentioned. Alternatively, or perhaps

additionally, the radical character may not be conserved when films are deposited from solution. This could be because once the solvent is gone, *t*-BP has more of an opportunity to quench spiro-OMeTAD$^{\bullet+}$ or/and interact with metal ions such as Li^+ (which likely would not complex with *t*-BP in solution phase) than it does in solution. To first test the impact of *t*-BP on the radical character of solutions, EPR spectra were taken of spiro-OMeTAD solutions with Li- or/and Co-TFSI with different concentrations of *t*-BP, the results of which are shown in Figure 21.

Based on the results from Lamberti *et al.*[41] and Wang *et al.*[40] showing quenching of spiro-OMeTAD$^{\bullet+}$ generated by Li-TFSI in the presence of *t*-BP and complexation of *t*-BP with Li^+, we predicted that decreasing the *t*-BP concentration would increase the radical character of solutions with Co-TFSI. We find that when the amount of *t*-BP is decreased in solutions with only Li-TFSI or only Co-TFSI, the radical character increases as predicted due to decreased *t*-BP-caused quenching of spiro-OMeTAD$^{\bullet+}$, a smaller degree of Li^+ complexation by *t*-BP, or both. However, when both salts are present there is little change in the signal. This lack of change could be due to the same synergistic effect of both salts

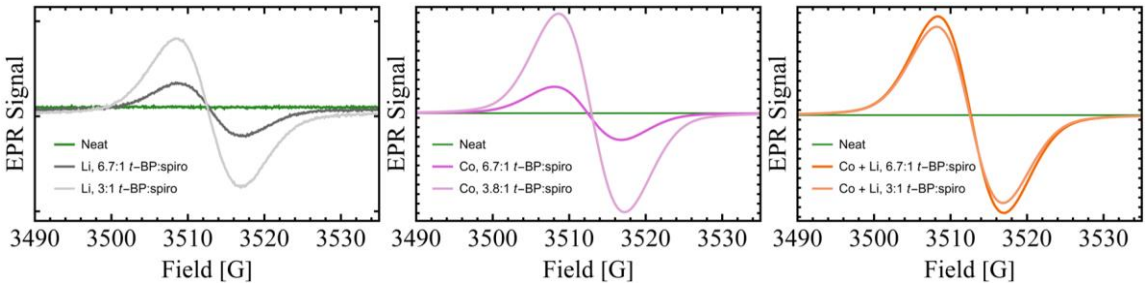

Fig. 21. EPR spectra of spiro-OMeTAD solutions with Li-TFSI at 1:4 mole ratio to spiro-OMeTAD ("Li," left), Co-TFSI at 1:10 mole ratio ("Co," center) or both ("Co + Li," right) and the effects of decreasing the *t*-BP concentration (*t*-BP concentrations shown in mole ratio to spiro-OMeTAD). Spectra shown are of solutions that have been exposed to air for an hour. Ticks on the vertical axis represent 2 units for Li-TFSI-containing solutions and 5 units for solutions with Co-TFSI only and both salts. The sample with only Co-TFSI and less *t*-BP has a larger *t*-BP:spiro-OMeTAD ratio than the others because it is the lowest possible *t*-BP concentration for smooth films with only Co-TFSI.

being present as that observed in the charge transfer characteristics presented in section V.II. These results suggest this synergistic effect is likely due to the ability of Co-TFSI to oxidize spiro-OMeTAD significantly in solution before film deposition. Because there is also Li-TFSI present, the *t*-BP may react with Li^+ once the film is formed while any Co^{3+} that has not already reacted may continue to oxidize spiro-OMeTAD. Further, interactions between Co-TFSI and *t*-BP could also occur, further decreasing the *t*-BP available to quench spiro-OMeTAD$^{\bullet+}$ or react with Li^+. Overall, these interactions all allow both Co- and Li-TFSI to generate more spiro-OMeTAD$^{\bullet+}$ than when only one salt or the other is present and for *t*-BP to quench less spiro-OMeTAD$^{\bullet+}$ as it is made. To further investigate these phenomena, the next question we ask is: how do these changes in radical character of solutions impact the charge transfer properties of contacts modified with Co- and Li-TFSI-containing spiro-OMeTAD?

III. Impact of *t*-BP on selectivity, recombination, charge transfer, and $V_{oc}^{(NH)}$

To investigate the role of *t*-BP in dictating the charge transfer characteristics, selectivity, and recombination of spiro-OMeTAD-modified contacts, the amount of *t*-BP in spiro-OMeTAD films with Li-TFSI only (1:4 mole ratio to spiro-OMeTAD), with Co-TFSI only (1:10 mole ratio), and with both salts was varied. The observed changes in the charge transfer characteristics due to decreasing the *t*-BP concentration are shown in Figure 22, where (a-) indicates the samples with lower *t*-BP content after air exposure and where the table shows the changes in $V_{oc}^{(NH)}$ that occur in response to the changes in J_{0n} and J_{0p}. Data shown in Fig. 22 represent the final measurement after six hours of air exposure (refer to Tables 7-9 for all initial and final values). The effects of air exposure with varying *t*-BP

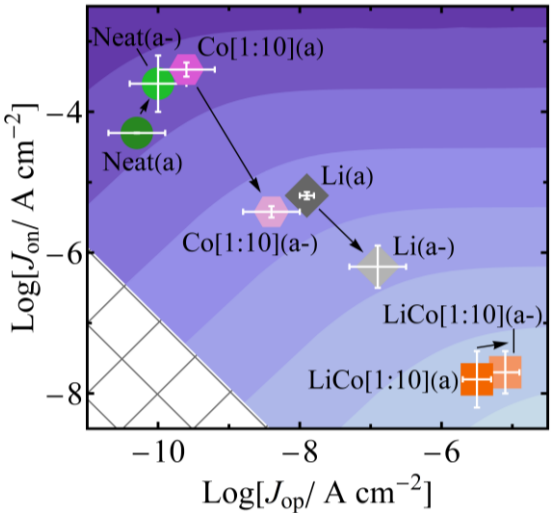

Change	$\Delta V_{oc}^{(NH)}$ [V]
Neat(a) → Neat(a-)	0.01(4)
Co[1:10](a) → Co[1:10](a-)	0.10(2)
Li(a) → Li(a-)	0.07(2)
LiCo[1:10](a) → LiCo[1:10](a-)	0.00(3)

Fig. 22. Changes to experimental J_0 values and accompanying changes in $V_{oc}^{(NH)}$ (tabulated) due to decreasing the amount of *t*-BP in spiro-OMeTAD films modifying gold contacts. All data shown are after air exposure as denoted with (a) or (a-) where the latter denotes films with less *t*-BP. Green circles = neat spiro-OMeTAD (where (a-) has no *t*-BP), black/gray diamonds = Li-TFSI at 1:4 mole ratio to spiro-OMeTAD, pink hexagons = Co-TFSI (1:10 mole ratio), orange squares = Li-TFSI (1:4 mole ratio) and Co-TFSI (1:10 mole ratio). All films contain the same spiro-OMeTAD concentration.

Table 7. Experimental $V_{oc}^{(NH)}$, $V_{oc}^{(PE)}$, and $I_{sc}^{(PN)}$ of mixtures studied, measured using the IBC cell. Amounts of *t*-BP, Li-TFSI, and Co-TFSI are given in mole ratio relative to spiro-OMeTAD. All samples contain the same spiro-OMeTAD concentration.

				$V_{oc}^{(NH)}$		$V_{oc}^{(PE)}$		$I_{sc}^{(PN)}$	
Sample	*t*-BP	Li-TFSI	Co-TFSI	Initial	Final	Initial	Final	Initial	Final
Gold	-	-	-	0.283(4)	0.285(5)	0.247(3)	0.245(3)	1.76(5)	1.75(5)
Spiro	-	-	-	0.12(3)	0.11(3)	0.44(2)	0.45(2)	2.29(4)	2.26(1)
Spiro, *t*-BP	6.7:1	-	-	0.12(1)	0.13(1)	0.46(1)	0.45(1)	2.48(5)	2.47(7)
Spiro, *t*-BP, Li-TFSI	3:1	1:4	-	0.17(2)	0.29(2)	0.39(2)	0.28(2)	2.02(4)	2.02(2)
Spiro, *t*-BP, Li-TFSI	6.7:1	1:4	-	0.14(1)	0.223(6)	0.43(1)	0.339(5)	2.24(3)	2.10(2)
Spiro, *t*-BP, Co-TFSI	3.8:1	-	1:10	0.17(2)	0.22(1)	0.40(2)	0.36(1)	2.28(8)	2.33(8)
Spiro, *t*-BP, Co-TFSI	6.7:1	-	1:10	0.09(1)	0.12(2)	0.47(1)	0.45(1)	2.13(3)	2.10(7)
Spiro, *t*-BP, Li-TFSI, Co-TFSI	3:1	1:4	1:10	0.22(1)	0.37(2)	0.32(1)	0.18(1)	1.84(2)	2.03(4)
Spiro, *t*-BP, Li-TFSI, Co-TFSI	6.7:1	1:4	1:10	0.16(3)	0.37(2)	0.36(3)	0.19(2)	1.80(1)	2.18(5)

concentration will be discussed below. The background grid and contour plot shown in Fig. 22 are reproduced from Figures 12 and 15 and described in more detail in section III.III.

As a brief summary, the blue scale contour plot in Fig. 22 shows the dependence of $V_{oc}^{(NH)}$ (the V_{oc} when the contact under study acts as the hole contact) on the two J_0 values. The data overlaid on top show the experimentally determined J_0 values for real spiro-OMeTAD-modified gold contacts. For a description of how these values are determined using IBC cell measurements and numerical simulation, refer to sections III.I and III.III. It is important to note that all spiro-OMeTAD-modified contacts presented here except "Neat(a)" operate in the regime where $V_{oc}^{(NH)}$ depends on J_{0n} alone, *i.e.*, the light-limited

Table 8. Initial (before 6 hours of air exposure) J_0 values for samples studied herein. Amounts of *t*-BP, Li-TFSI, and Co-TFSI are given in mole ratio relative to spiro-OMeTAD. All samples contain the same spiro-OMeTAD concentration.

Sample	*t*-BP	Li-TFSI	Co-TFSI	Log(J_{0n})	Log(J_{0p})	Log(J_{0p}/J_{0n})	Log($(J_{0n}J_{0p})^{0.5}$)
Gold	-	-	-	-5.7(1)	0.8(1)	6.5(2)	-2.5(2)
Spiro	-	-	-	-3.9(3)	-10.0(5)	-6.0(8)	-6.9(1)
Spiro, *t*-BP	6.7:1	-	-	-4.06(3)	-10.6(3)	-6.5(4)	-7.3(1)
Spiro, *t*-BP, Li-TFSI	3:1	1:4	-	-4.3(2)	-8.5(3)	-4.2(5)	-6.4(1)
Spiro, *t*-BP, Li-TFSI	6.7:1	1:4	-	-4.1(1)	-9.4(2)	-5.4(3)	-6.76(5)
Spiro, *t*-BP, Co-TFSI	3.8:1	-	1:10	-4.6(2)	-9.1(5)	-4.5(7)	-6.8(1)
Spiro, *t*-BP, Co-TFSI	6.7:1	-	1:10	-3.1(1)	-10.0(2)	-6.9(3)	-6.58(5)
Spiro, *t*-BP, Li-TFSI, Co-TFSI	3:1	1:4	1:10	-4.9(1)	-7.1(4)	-2.2(4)	-6.0(1)
Spiro, *t*-BP, Li-TFSI, Co-TFSI	6.7:1	1:4	1:10	-4.0(5)	-7.7(6)	-4(1)	-5.87(5)

Table 9. Final (after 6 hours of air exposure) J_0 values for samples studied herein. Amounts of *t*-BP, Li-TFSI, and Co-TFSI are given in mole ratio relative to spiro-OMeTAD. All samples contain the same spiro-OMeTAD concentration.

Sample	*t*-BP	Li-TFSI	Co-TFSI	Log(J_{0n})	Log(J_{0p})	Log(J_{0p}/J_{0n})	Log($(J_{0n}J_{0p})^{0.5}$)
Gold	-	-	-	-5.8(1)	0.9(1)	6.6(2)	-2.5(2)
Spiro	-	-	-	-3.6(4)	-10.0(4)	-6.4(8)	-6.81(1)
Spiro, *t*-BP	6.7:1	-	-	-4.274(4)	-10.3(4)	-6.0(4)	-7.3(2)
Spiro, *t*-BP, Li-TFSI	3:1	1:4	-	-6.2(3)	-6.6(4)	-0.5(7)	-6.40(3)
Spiro, *t*-BP, Li-TFSI	6.7:1	1:4	-	-5.19(5)	-7.9(1)	-2.7(2)	-6.53(3)
Spiro, *t*-BP, Co-TFSI	3.8:1	-	1:10	-5.42(8)	-8.4(4)	-6.2(5)	-6.5(1)
Spiro, *t*-BP, Co-TFSI	6.7:1	-	1:10	-3.4(1)	-9.6(4)	-6.2(5)	-6.5(1)
Spiro, *t*-BP, Li-TFSI, Co-TFSI	3:1	1:4	1:10	-7.7(3)	-5.1(2)	2.5(5)	-6.4(1)
Spiro, *t*-BP, Li-TFSI, Co-TFSI	6.7:1	1:4	1:10	-7.8(4)	-5.5(2)	2.4(7)	-6.7(1)

carrier selectivity. However, changes in J_{0p}/J_{0n}, the contact hole selectivity, are often discussed instead as they can provide insight about the chemical changes occurring in the film. For example, when spiro-OMeTAD oxidizes in the presence of Li-TFSI and air, J_{0p}/J_{0n} increases due to the formation of spiro-OMeTAD$^{\bullet+}$. However, the observed increases in $V_{oc}^{(NH)}$ due to this oxidation are specifically due to the decreases in J_{0n}.

We find that when the amount of *t*-BP decreases, no significant changes in the J_0 values or $V_{oc}^{(NH)}$ are observed for samples with no salt or with both salts. However, when only Co- or Li-TFSI is present there are significant increases in the contact hole selectivity and $V_{oc}^{(NH)}$ when the *t*-BP content goes down, the largest being for films containing only Co-TFSI (1:10 mole ratio). These results show for the first time the quantitative impact of *t*-BP quenching of spiro-OMeTAD$^{\bullet+}$ or/and *t*-BP complexation with metal ions on charge transfer and $V_{oc}^{(NH)}$. That is, there is a higher concentration of spiro-OMeTAD$^{\bullet+}$ in the film when the *t*-BP concentration decreases, resulting in an increase in hole contact selectivity (J_{0p} increases by up to an order of magnitude, J_{0n} decreases by up to two orders of magnitude) while recombination remains unchanged. In this regime, the decreases in J_{0n} are responsible for the 100 and 70 mV increases in $V_{oc}^{(NH)}$ for samples with Co-TFSI (1:10 mole ratio to spiro-OMeTAD) or Li-TFSI (1:4 mole ratio), respectively.

These results indicate that at higher *t*-BP concentrations with Co-TFSI at 1:10 mole ratio to spiro-OMeTAD, there may be enough *t*-BP in the film to quench any spiro-OMeTAD$^{\bullet+}$ such that no changes in contact properties are measured. Then, when the *t*-BP concentration is decreased, the largest changes in $V_{oc}^{(NH)}$ are observed compared to films with only Li-TFSI or with both salts. Intuitively, this indicates that as overall salt

concentration decreases, the contact properties depend more strongly on *t*-BP concentration. Further, when both salts are present, decreasing the *t*-BP concentration does not change the charge transfer characteristics or $V_{oc}^{(NH)}$. This could be because there is little enough *t*-BP at the higher concentration that it does not impact the formation of spiro-OMeTAD$^{\bullet+}$. Additionally, it could be due to the complexation of Li^+ or other Co-related species with *t*-BP, causing little spiro-OMeTAD$^{\bullet+}$ quenching at either *t*-BP concentration.

To further illustrate the role of *t*-BP in dictating the charge transfer characteristics of spiro-OMeTAD-modified gold contacts, Figure 23 shows the changes in the J_0 values and accompanying changes in the $V_{oc}^{(NH)}$ values when samples with different *t*-BP

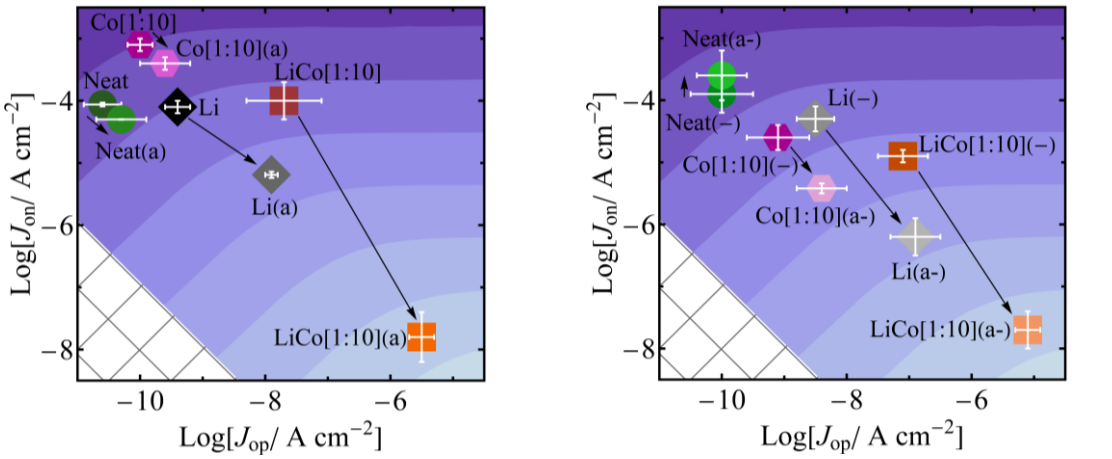

Change	$\Delta V_{oc}^{(NH)}$ [V]
Neat → Neat(a)	0.01(1)
Co[1:10] → Co[1:10](a)	0.03(2)
Li → Li(a)	0.08(1)
LiCo[1:10] → LiCo[1:10](a)	0.21(4)

Change	$\Delta V_{oc}^{(NH)}$ [V]
Neat(-) → Neat(a-)	-0.01(4)
Co[1:10](-) → Co[1:10](a-)	0.05(2)
Li(-) → Li(a-)	0.12(3)
LiCo[1:10](-) → LiCo[1:10](a-)	0.15(2)

Fig. 23. Changes to experimental J_0 values and accompanying changes in $V_{oc}^{(NH)}$ (tabulated) due to air exposure when different amounts of *t*-BP are present in the spiro-OMeTAD film. Samples in the left panel have more *t*-BP (6.7:1 mole ratio to spiro-OMeTAD) than samples in the right panel (3-3.8:1 mole ratio to spiro-OMeTAD), as indicated with (-). Green circles = neat spiro-OMeTAD, black/gray diamonds = Li-TFSI (1:4 mole ratio to spiro-OMeTAD), pink hexagons = Co-TFSI (1:10 mole ratio), and orange squares = Li-TFIS (1:4 mole ratio) and Co-TFSI (1:10 mole ratio to spiro-OMeTAD).

concentrations are exposed to air. For samples with Co- or Li-TFSI only, larger changes are observed due to air exposure at lower *t*-BP concentrations. This result reflects the smaller degree of spiro-OMeTAD$^{\bullet+}$ quenching that occurs when less *t*-BP is present and/or the lesser degree of metal complexation at lower *t*-BP concentrations. That is, more spiro-OMeTAD$^{\bullet+}$ is generated in the film due to air exposure.

When both salts are present, there is a smaller change over time in air with lower *t*-BP concentration. This, however, is simply due to the initial contact hole selectivity being larger, indicating a higher degree of spiro-OMeTAD oxidation before the first measurement is taken because there is less *t*-BP available to quench spiro-OMeTAD$^{\bullet+}$ or/and complex with metal ions. As also demonstrated in Fig. 22, the charge transfer characteristics and $V_{\mathrm{oc}}^{(\mathrm{NH})}$ after air exposure of films with both salts are the same regardless of *t*-BP concentration. This indicates that when both salts are used, an equilibrium is established where there is a maximum spiro-OMeTAD$^{\bullet+}$ concentration that can be formed that is not impacted by decreasing the *t*-BP concentration. In this case, there is a low enough *t*-BP concentration already that decreasing it further does not change the overall spiro-OMeTAD$^{\bullet+}$ concentration that can be produced. Instead, it impacts how *quickly* spiro-OMeTAD$^{\bullet+}$ is generated.

These representations show the differences in charge transfer and the V_{oc} when the *t*-BP to spiro-OMeTAD mole ratio is varied. However, it is instructive to also compare the results when the *t*-BP to overall salt concentration is approximately the same for the different compositions. Thus, Figure 24 shows the characteristics of samples with different amounts of salt and *t*-BP but with approximately the same *t*-BP to overall salt concentration ratio. The two exceptions are neat spiro-OMeTAD, which has no *t*-BP in this

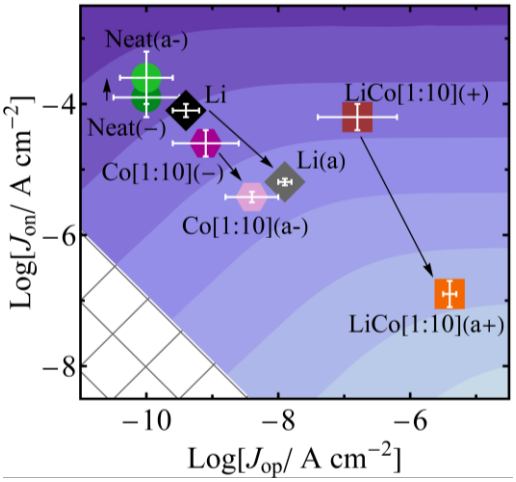

Fig. 24. Changes to experimental J_0 values due to air exposure when the *t*-BP:overall salt concentration ratio is approximately the same. Green circles = neat spiro-OMeTAD, black/gray diamonds = Li-TFSI (1:4 mole ratio to spiro-OMeTAD), pink hexagons = Co-TFSI (1:10 mole ratio), and orange squares = Li-TFIS (1:4 mole ratio) and Co-TFSI (1:10 mole ratio to spiro-OMeTAD). The amount of *t*-BP compared to spiro-OMeTAD is indicated using (-) or (+) while (a) indicates air exposure.

representation, and spiro-OMeTAD with Co-TFSI only, which has a minimum *t*-BP concentration to achieve smooth films and thus the *t*-BP to salt ratio is as low as it can be. However, comparing the samples in this manner is still instructive. Table 10 shows all initial and final J_0 and $V_{oc}^{(NH)}$ values presented graphically in Fig. 24. Samples with both salts, in this case, have a higher *t*-BP concentration than any of those previously shown, as indicated in Fig. 24 with (+).

When the *t*-BP to overall salt concentration is approximately the same, we find that

Table 10. Measured J_0 and $V_{oc}^{(NH)}$ values for samples with approximately the same *t*-BP to total salt mole ratio. All samples contain the same spiro-OMeTAD concentration.

	Log(J_{0n})		Log(J_{0p})		Log(J_{0p}/J_{0n})		Log(($J_{0n}J_{0p}$)$^{0.5}$)		$V_{oc}^{(NH)}$	
Mole Ratio	Initial	Final	Initial	Final	Initial	Final	Initial	Final	Initial	Final
[27:1] *t*-BP:Li-TFSI	-4.1(1)	-5.19(5)	-9.4(2)	-7.9(1)	-5.4(3)	-2.7(2)	-6.76(5)	-6.53(3)	0.14(1)	0.223(6)
[36:1] *t*-BP:Co-TFSI	-4.6(2)	-5.42(8)	-9.1(5)	-8.4(4)	-4.5(7)	-6.2(5)	-6.8(1)	-6.5(1)	0.17(2)	0.22(1)
[25:1] *t*-BP:Li- & Co-TFSI	-4.2(2)	-6.9(2)	-6.8(6)	-5.4(1)	-2.6(8)	1.4(3)	-5.5(2)	-6.2(1)	0.18(2)	0.34(1)

spiro-OMeTAD with Co-TFSI (1:10 mole ratio to spiro-OMeTAD) yields about the same properties after air exposure as that with Li-TFSI (1:4 mole ratio to spiro-OMeTAD). When both salts are present, the results are similar to those when there is less *t*-BP, that is, the addition of both salts leads to larger changes than when only one or the other is present. This representation illustrates two important points. First, when the *t*-BP to salt ratio is approximately the same, a lower concentration of Co-TFSI can yield about the same changes in charge transfer and V_{oc} characteristics as a higher concentration of Li-TFSI, aligning more with our original predictions based on the EPR results than. Second, when both salts are present, while decreasing the *t*-BP concentration does not change the properties of air-exposed samples, increasing the *t*-BP concentration does change them, though only slightly (compare the air exposed sample shown here to those in Fig. 23). This means spiro-OMeTAD-modified gold contacts with both salts are not immune to the quenching effects of *t*-BP or/and the effects of *t*-BP complexation with metal ions or other species. However, as mentioned above, the presence of both salts still tempers the effects of *t*-BP because of the synergistic effects of the interactions of both salts with *t*-BP and also likely because there is a significant concentration of spiro-OMeTAD$^{\bullet+}$.

While these results illustrate the dependence of the charge transfer characteristics and $V_{oc}^{(NH)}$ on *t*-BP concentration, they do not explain why the contact hole selectivity when Co-TFSI is the only salt present does not reflect the significant radical character measured for solutions. Though the properties do change with *t*-BP concentration, indicating the presence of spiro-OMeTAD$^{\bullet+}$ in the film when only Co-TFSI is present (particularly at lower *t*-BP concentration), based on the EPR results one would predict the J_{0p}/J_{0n} and $V_{oc}^{(NH)}$ to be significantly larger for Co-TFSI only films than for Li-TFSI only films, which we

never observe to be the case regardless of *t*-BP concentration. As mentioned above, one explanation could be that *t*-BP quenches spiro-OMeTAD$^{\bullet+}$ to a much larger degree in films than in solution because the lack of solvent increases its proximity to spiro-OMeTAD$^{\bullet+}$. Once this film is deposited, this would essentially reverse the formation of spiro-OMeTAD$^{\bullet+}$ by Co-TFSI in solution, causing the concentration in the film to be very low and the contact hole selectivity to be similar to that of gold contacts modified with neat spiro-OMeTAD. When less *t*-BP is present, more spiro-OMeTAD$^{\bullet+}$ is produced in solution *and* less is quenched when the film is made, leading to a high enough concentration in the film to change the contact properties. Another explanation is the interaction of *t*-BP with Co-TFSI, Li-TFSI, or other species generated in the film, which could either impact the amount of spiro-OMeTAD$^{\bullet+}$ produced or determine the contact properties instead of spiro-OMeTAD$^{\bullet+}$ or both.

To investigate whether any of these hypotheses could be the case, visible spectra of spiro-OMeTAD films were collected both before and after one hour of dark air exposure as shown in Figure 25 (refer to Appendix A for complete experimental details). Neutral spiro-OMeTAD absorbs maximally at about 390 nm compared to the 521 nm of spiro-OMeTAD$^{\bullet+}$. Previous studies have shown that as the peak at 521 nm increases with the concentration of oxidant in spiro-OMeTAD solutions, the peak at 390 nm decreases, generating an isosbestic point and indicating the conversion of one species into the other.[42-44] The results presented in Fig. 25 likewise show this is the case due to air exposure. Thus, the ratio of the absorbances at these two peaks provides a measure of how much spiro-OMeTAD$^{\bullet+}$ is present compared to neutral spiro-OMeTAD. This comparison also "normalizes" for potential differences in film thickness. Comparing this value to the charge

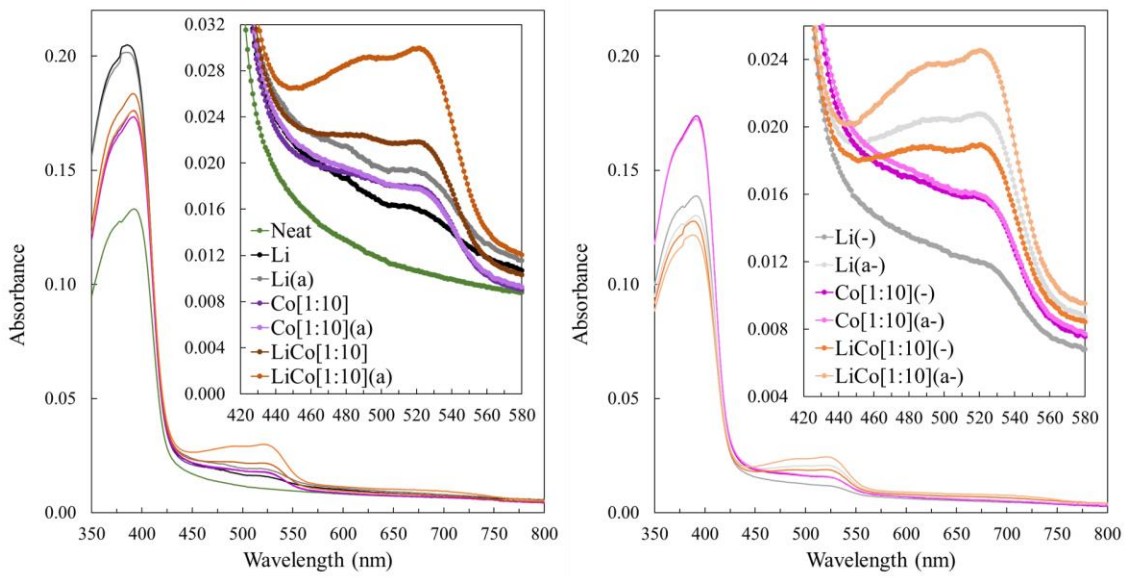

Fig. 25. Visible spectra of spiro-OMeTAD films with Li-TFSI (1:4 mole ratio to spiro-OMeTAD, black/gray), Co-TFSI (1:10 mole ratio, pink/purple), Co-TFSI (1:10 mole ratio) and Li-TFSI (1:4 mole ratio, red/orange), or neat (green) before and after one hour of air exposure. On the left, films have higher *t*-BP concentration (6.7:1 mole ratio to spiro-OMeTAD) while those on the right have lower *t*-BP concentration (3-3.8:1 mole ratio) as denoted by (-). All solutions used to make films contain the same spiro-OMeTAD concentration. The peaks corresponding to spiro-OMeTAD$^{\bullet+}$ are shown magnified inset.

transfer characteristics or $V_{oc}^{(NH)}$ measured for spiro-OMeTAD-modified contacts can tell us whether the contact properties (specifically, the contact selectivity) we measure using IBC cell experiments depend on the amount of spiro-OMeTAD$^{\bullet+}$ in the film.

Thus, Figure 26 shows the ratio of the absorbance at 521 nm to that at 390 nm for spiro-OMeTAD films compared to the $V_{oc}^{(NH)}$ and J_{0p}/J_{0n} measured for contacts modified with the same spiro-OMeTAD film compositions. These values all correspond to either the initial time point or the measurement after one hour of dark air exposure. For films with Li-TFSI only and with both salts, we find that the peak ratios report on the $V_{oc}^{(NH)}$ and J_{0p}/J_{0n}, indicating that the formation of spiro-OMeTAD$^{\bullet+}$ measured *via* UV-Vis is likely responsible for the observed changes in contact properties.

However, films with only Co-TFSI do not follow the same trends. In fact, contrary

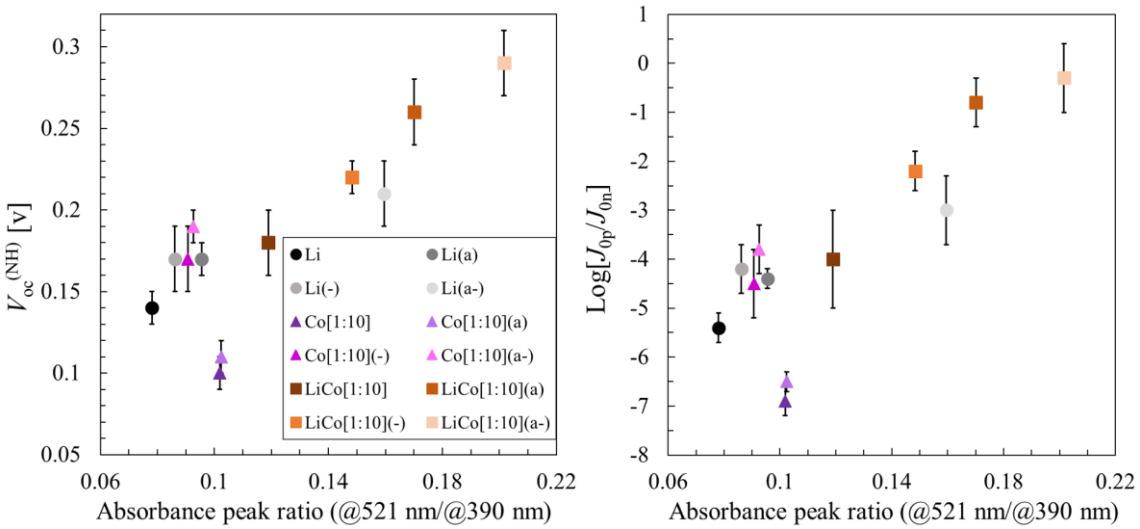

Fig. 26. Ratio of the absorbance peak at 521 nm to that at 390 nm for spiro-OMeTAD films with different salt and *t*-BP concentrations both before and after 1 hour of air exposure plotted *vs.* the corresponding $V_{oc}^{(NH)}$ (left) and log[J_{0p}/J_{0n}] (right) values of contacts modified with the same films.

to the changes in charge transfer characteristics we observe when decreasing the *t*-BP concentration, the peak ratio does not change to a large degree with *t*-BP concentration for these films. This finding indicates that despite the solution-phase dependence of spiro-OMeTAD$^{\bullet+}$ concentration on *t*-BP content in the presence of Co-TFSI, and the differences in charge transfer when the *t*-BP concentration is decreased in spiro-OMeTAD films containing only Co-TFSI, the spiro-OMeTAD$^{\bullet+}$ concentration in films with Co-TFSI only does not depend on the *t*-BP concentration. Further, this also means that at higher *t*-BP concentrations, contact hole selectivity (J_{0p}/J_{0n}) and the $V_{oc}^{(NH)}$ do not appear to depend on the spiro-OMeTAD$^{\bullet+}$ concentration.

These findings indicate that the reactions between spiro-OMeTAD, Co-TFSI, and *t*-BP are likely different than those between spiro-OMeTAD, Li-TFSI, and *t*-BP. This could explain both the low contact hole selectivity when Co-TFSI alone is used (at 1:10 mole ratio to spiro-OMeTAD) and the much larger effects of using both Co- and Li-TFSI than

only one or the other alone. As mentioned, at higher *t*-BP concentrations, the presence of spiro-OMeTAD$^{\bullet+}$ in these films may not dictate the contact selectivity or $V_{oc}^{(NH)}$ of Co-TFSI-containing spiro-OMeTAD-modified contacts. Instead, some other aspect of the film chemistry – perhaps involving the ligand of the Co(III) complex, the interaction between Co-TFSI and *t*-BP, or simply the sheer number of *t*-BP molecules – could overpower the contributions of spiro-OMeTAD$^{\bullet+}$ to the contact properties and therefore $V_{oc}^{(NH)}$. When Li-TFSI is also present, these interactions could simply limit the availability of *t*-BP to quench spiro-OMeTAD$^{\bullet+}$ or complex with metal ions, thus causing greater increases in spiro-OMeTAD$^{\bullet+}$ concentration than when only one salt or the other is present, leading to greater increases in contact hole selectivity. Future work is necessary to determine the exact nature of these interactions, however.

In summary, we find the *t*-BP concentration impacts both the radical character of spiro-OMeTAD solutions with only Co- or Li-TFSI and the charge transfer characteristics, in particular the contact selectivity, of spiro-OMeTAD-modified contacts also with Co- or Li-TFSI. When both salts are present, however, there is little change in radical character or charge transfer characteristics when the *t*-BP concentration decreases, likely because the original *t*-BP concentration was low enough to not impact the properties. At the same time, we find that in the case where the only salt is Co-TFSI, the spiro-OMeTAD$^{\bullet+}$ concentration as determined using UV-Vis measurements does not always correlate with the $V_{oc}^{(NH)}$ or J_{0p}/J_{0n}, unlike when Li-TFSI only or both salts are present.

Taken in conjunction with results from measuring the impact of Co-TFSI itself on the charge transfer properties of spiro-OMeTAD-modified gold contacts, these results suggest that while Co-TFSI generates significant concentrations of spiro-OMeTAD$^{\bullet+}$ in

solution, this species does not always dictate the properties of spiro-OMeTAD-modified contacts with only Co-TFSI. Instead, when the *t*-BP concentration is high enough, other interactions in the film appear to have a greater impact and may also contribute to the larger changes in charge transfer properties and $V_{oc}^{(NH)}$ when both salts are used. Elucidation of the exact nature of these interactions is still necessary, however. These results have implications for the use of additives in spiro-OMeTAD IFLs in complete solar cells and will aid the rational design of IFLs in general for higher photovoltaic efficiencies.

CHAPTER VII

THE ROLE OF SPIRO-OMETAD IN HYSTERESIS BEHAVIOR

This chapter contains both published and unpublished results. Measurements of IBC cell quantities of spiro-OMeTAD-modified gold contacts with Li-TFSI shown in this chapter are published in the Results and Discussion section of Egelhofer Ruegger *et al.* 2020[1] while the same measurements with Co-TFSI are unpublished. Further, the resulting changes in J_0 values are all unpublished. For a complete discussion of what the IBC cell results mean and how we determine J_0 values from these measurements and numerical simulation, please refer to sections III.I and III.III.

For a complete discussion of hysteresis phenomena in solar cells and the potential role of spiro-OMeTAD, please refer to section I.IV. To briefly summarize, hysteresis describes the typically undesired behavior wherein the performance of a solar cell changes under different pre-measurement conditions. This phenomenon does not allow a solar cell to operate consistently under steady-state conditions, limiting its viability for commercialization. Perovskite solar cells often demonstrate severe hysteresis[20,48-50] but the specific role of spiro-OMeTAD remains unclear. Some studies have employed informative and interesting techniques[20,48] for probing the movement of carriers and ions during solar cell operation and their relation to hysteresis. These studies suggest spiro-OMeTAD could be involved, but there is little information about whether there are fundamental changes to spiro-OMeTAD during cell operation and how such changes could contribute to shifts in V_{oc} and to overall hysteresis behavior. Thus, this study aims to elucidate just such information, which will aid the field in addressing hysteresis phenomena in perovskite cells employing spiro-OMeTAD and more generally in IFL-containing solar cells that

demonstrate hysteresis behavior.

To illustrate the contributions of charge transfer at spiro-OMeTAD-modified contacts to hysteresis behavior, we employ new *operando* measurements using the IBC cell to show how electron and hole transfer rates at the spiro-OMeTAD-modified contact are affected by cell operation. Operation of the cell subjects the modified contact to the same pre-measurement conditions (*i.e.*, voltage applied under illumination) as those that produce hysteresis in perovskite and SSDS cells. These *operando* measurements are performed with the spiro-OMeTAD-modified gold contact to the IBC cell operating as the hole contact *vs.* the n^+-Si electron contact (use of the IBC cell to measure IFL-modified contact properties is detailed in section III.I). In this study, spiro-OMeTAD films contain either Li-TFSI alone (in a 1:4 mole ratio to spiro-OMeTAD) or both Li-TFSI and one of three Co-TFSI concentrations, 1:20, 1:10, or 1:5 mole ratio to spiro-OMeTAD (for more details about why salts are added to spiro-OMeTAD and their impacts on the properties of spiro-OMeTAD-modified gold contacts, refer to section I.IV and Chapters IV and V). All films in this study contain salts because we are interested in understanding the contribution of spiro-OMeTAD IFLs with commonly used dopant concentrations.[20,24,28,42-46]

Before conducting these measurements, the spiro-OMeTAD-modified gold contact is exposed to air for 6 hours after which a nitrogen atmosphere is established for 90 minutes for stabilization of $V_{\mathrm{oc}}^{(\mathrm{PE})}$, $V_{\mathrm{oc}}^{(\mathrm{NH})}$, and $I_{\mathrm{sc}}^{(\mathrm{PN})}$. To operate the cell, it is illuminated for 60 seconds with the applied voltage (V_{app}) held at either: 0.8 V (forward bias), 0.34 V (V_{oc}), 0 V (short circuit), or -0.8 V (reverse bias). The cell is then returned to open circuit in the dark, and the time dependence of $V_{\mathrm{oc}}^{(\mathrm{PE})}$, $V_{\mathrm{oc}}^{(\mathrm{NH})}$, and $I_{\mathrm{sc}}^{(\mathrm{PN})}$ is measured.

Figures 27 and 28 show the transients in $V_{\mathrm{oc}}^{(\mathrm{PE})}$, $V_{\mathrm{oc}}^{(\mathrm{NH})}$, and $I_{\mathrm{sc}}^{(\mathrm{PN})}$ following cell

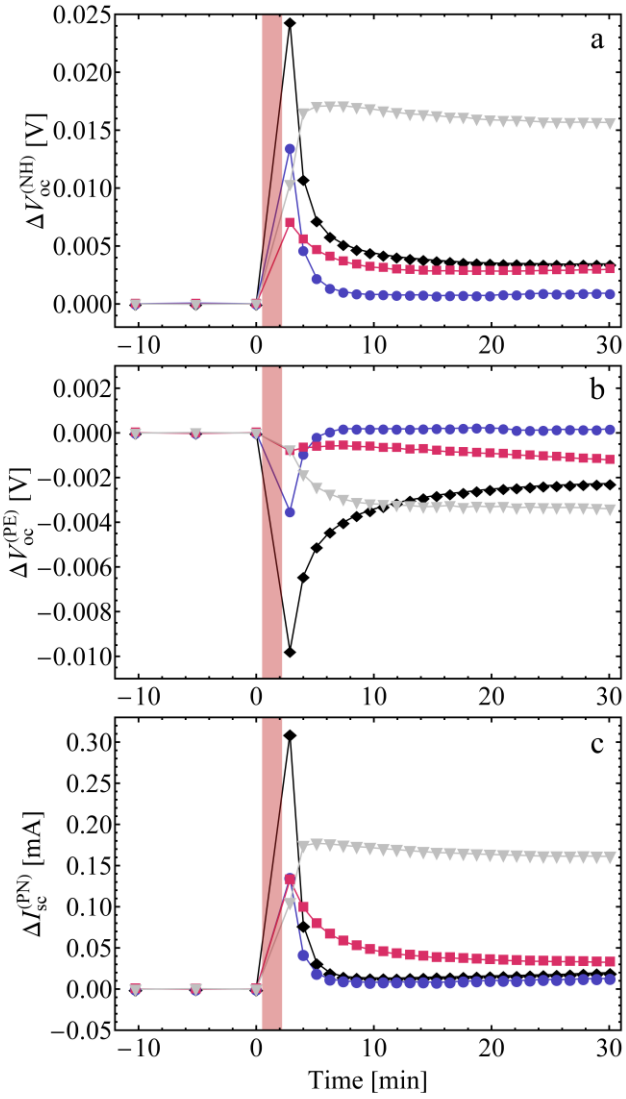

Fig. 27. Changes to (a) $V_{oc}^{(NH)}$, (b) $V_{oc}^{(PE)}$, and (c) $I_{sc}^{(PN)}$ when potential steps are applied to the Li-TFSI-containing spiro-OMeTAD-modified gold contact when it acts as the hole contact (is operated *vs.* the n^+-Si back contact). Li-TFSI is present in a 1:4 mole ratio to spiro-OMeTAD. Black diamonds indicate forward bias V_{app} = 0.8 V, blue circles are V_{app} = V_{oc}, fuchsia squares are V_{app} = 0 V, and gray inverted triangles are reverse bias V_{app} = -0.8 V. The red shaded area indicates the time during which the voltage is applied under illumination.

operation. Fig. 27 shows the effects of the four different applied voltages while Fig. 28 shows the effects of only forward bias on the properties when different salt mixtures are used in the spiro-OMeTAD film. Though the cells stabilize for 90 minutes after transition into nitrogen, some small drift in the measured quantities remains, thus data in both figures

are corrected for this baseline drift.

When only Li-TFSI is present, the direction of change of each parameter is independent of the operating voltage, but the magnitude of change and the change over time depend on V_{app}. The largest changes occur when forward bias (0.8 V) is applied. The

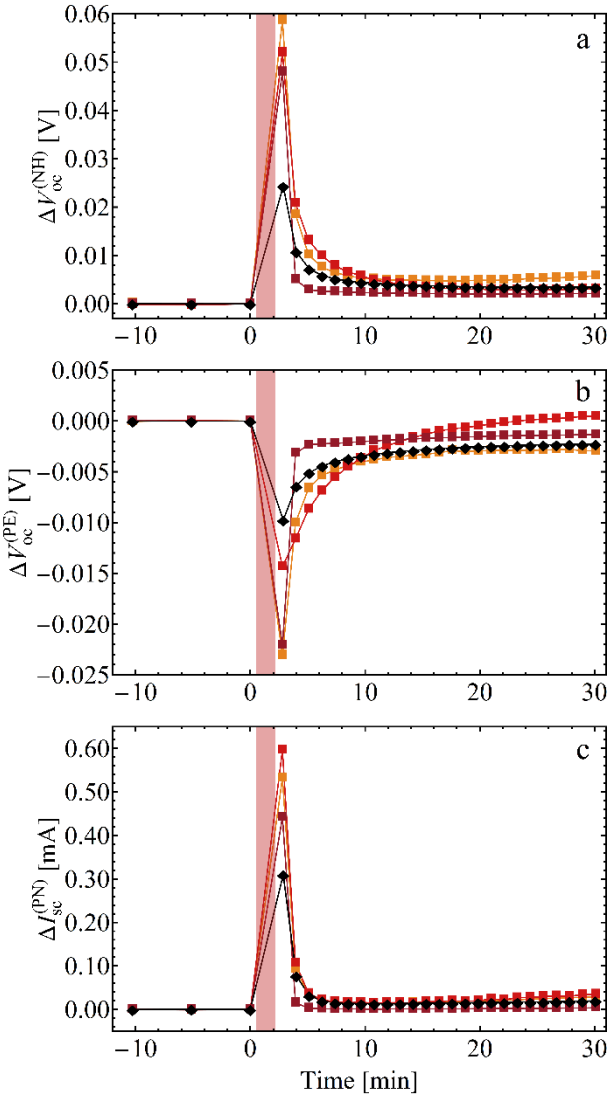

Fig. 28. Changes to (a) $V_{oc}^{(NH)}$, (b) $V_{oc}^{(PE)}$, and (c) $I_{sc}^{(PN)}$ when potential steps are applied to Co- and/or Li-TFSI-containing spiro-OMeTAD-modified gold contacts when they act as the hole contact (operated *vs.* the n^+-Si back contact). All traces correspond to forward bias V_{app}. Black diamonds indicate samples with Li-TFSI (1:4 mole ratio to spiro-OMeTAD) and no Co-TFSI while squares refer to samples with both Co-TFSI and Li-TFSI (1:4 mole ratio). Orange = Co-TFSI at 1:20 mole ratio, red = Co-TFSI at 1:10 mole ratio, dark red = Co-TFSI at 1:5 mole ratio. The red shaded area indicates the time during which the voltage is applied under illumination.

$V_{oc}^{(PE)}$ decreases while $V_{oc}^{(NH)}$ and $I_{sc}^{(PN)}$ both increase with each pre-bias application. Further, the duration of the effect depends on the voltage; voltages further into reverse bias cause longer relaxation times. In particular, reverse bias application (-0.8 V) leads to the most lasting effect of the voltages studied.

When Co-TFSI is added at various concentrations and forward bias is applied, the changes occur in the same direction for each parameter as when Li-TFSI is used alone. However, the magnitude of the change of each parameter is even greater than when Co-TFSI is not present. In particular, the change in $V_{oc}^{(NH)}$ is more than twice as large as when Li-TFSI is used alone. These results indicate that the potential interactions between Co-TFSI and *t*-BP or other chemistries occurring in the presence of Co-TFSI discussed in detail in section VI.III could be causing spiro-OMeTAD to contribute to a larger degree to hysteretic behavior than when Co-TFSI is not used. Alternatively, or perhaps additionally, the larger effect could simply be due to an increase in overall salt concentration in the film or higher spiro-OMeTAD$^{\bullet+}$ concentration (see below for further discussion of the potential causes for the observed changes in contact properties due to operation).

These changes in the experimentally measured IBC cell results translate to changes in charge transfer (for a description of how IBC cell measurements and simulation results are used to quantify charge transfer, please refer to sections III.I and III.III). Figure 29 shows the changes in Log[J_{0p}] and Log[J_{0n}] when gold contacts modified with spiro-OMeTAD containing only Li-TFSI (1:4 mole ratio to spiro-OMeTAD) or both Li-TFSI and Co-TFSI (1:10 mole ratio) are subjected to forward bias *operando* conditions. The J_0 values for the samples containing 1:10 mole ratio Co-TFSI to spiro-OMeTAD are the ones shown of the three Co-TFSI concentrations because the changes in $V_{oc}^{(PE)}$, $V_{oc}^{(NH)}$, and $I_{sc}^{(PN)}$

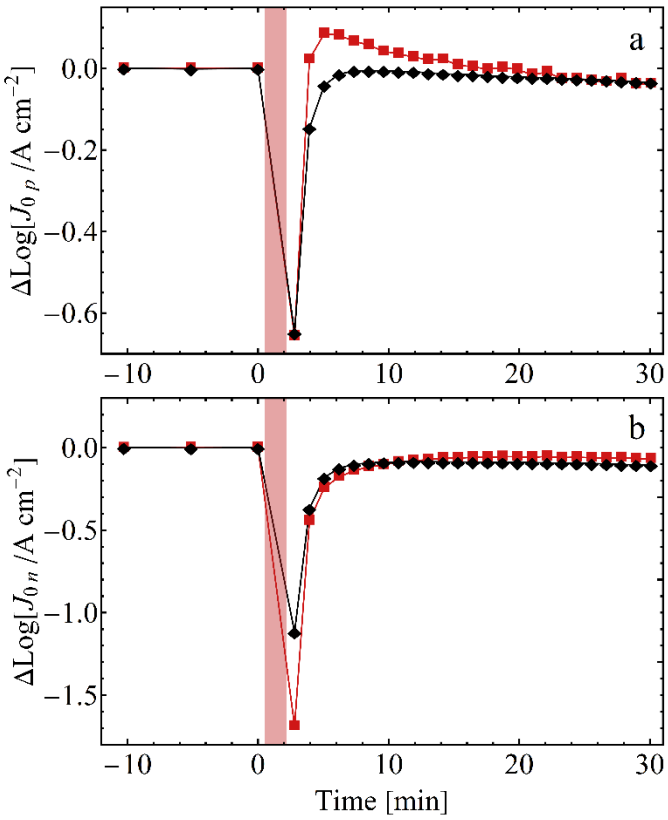

Fig. 29. Changes to (a) Log[J_{0p}] and (b) Log[J_{0n}] when a forward bias potential step (0.8 V) is applied to Co- and/or Li-TFSI-containing spiro-OMeTAD-modified gold contacts when they act as the hole contact (operated *vs.* the n^+-Si back contact). Black diamonds = Li-TFSI (1:4 mole ratio to spiro-OMeTAD) with no Co-TFSI, red squares = both Co-TFSI (1:10 mole ratio) and Li-TFSI (1:4 mole ratio). The red shaded area indicates the time during which the voltage is applied under illumination.

are very similar for all three Co-TFSI concentrations. Thus, the changes in J_{0n} and J_{0p} for all three Co-TFSI concentrations are likewise similar.

For spiro-OMeTAD-modified contacts both with and without Co-TFSI, both J_{0n} and J_{0p} experience a transient decrease. Further, these results show that the larger changes in $V_{oc}^{(PE)}$, $V_{oc}^{(NH)}$, and $I_{sc}^{(PN)}$ Co-TFSI is used at 1:10 mole ratio are due to a larger change in J_{0n} while the change in J_{0p} is the same. This reflects the dependence of $V_{oc}^{(NH)}$ on J_{0n} in the regime where these samples operate, *i.e.*, the J_{0n} must change in order for the $V_{oc}^{(NH)}$ to change. When Co-TFSI at a 1:10 mole ratio is present, the J_{0n} changes by more than half

an order of magnitude more than when it is not, causing the ~25 mV larger increase in $V_{oc}^{(NH)}$. Otherwise, the responses to applied bias with *vs*. without Co-TFSI are nominally the same.

Our *operando* measurements show for the first time that, independent of the sign or magnitude of applied voltage or the addition of Co-TFSI, the J_{0n} and J_{0p} of spiro-OMeTAD-modified gold contacts both decrease in a transient manner when the cell is operated. These results indicate that the properties of the spiro-OMeTAD IFL *change under the same conditions as those that produce hysteresis in complete cells* and that the contribution of spiro-OMeTAD to hysteretic behavior is to reversibly decrease the rates of both electron and hole transfer at the hole contact, decreasing $(J_{0n}J_{0p})^{0.5}$ and slightly increasing J_{0p}/J_{0n}.

We do not believe these changes are due to reduction of spiro-OMeTAD$^{\bullet+}$ because that would cause an increase in J_{0n} rather than the decrease we observe. Instead, these changes could occur in response to trap filling[65] in the spiro-OMeTAD film, causing J_{0n} and J_{0p} to decrease regardless of the sign or magnitude of V_{app}, instead simply depending on the flow of some partial current across the interface. The reversibility of the effect could be due to the system relaxing back to equilibrium when V_{app} is removed through extraction of trapped carriers at the contact. Further, the larger changes in the presence of Co-TFSI could simply be due to the higher overall salt or/and spiro-OMeTAD$^{\bullet+}$ concentration in the film or to the complexation of *t*-BP with Co-TFSI which could generate defect-causing species. Both of these phenomena could increase the trap density and therefore trap filling upon operation, leading to a larger change in the properties of the spiro-OMeTAD-modified contact.

The changes in J_{0n} and J_{0p} due to operation of the cell in the power quadrant result in an increase in $V_{oc}^{(NH)}$, indicating that spiro-OMeTAD can contribute to the observed increases in V_{oc} that are often characteristic of hysteresis in both perovskite and SSDS cells.[20,48-50] That the same direction of change also occurs when reverse bias is applied is in contrast to decreases in V_{oc} that are observed when complete cells are held at reverse bias before current-voltage characterization,[48-50] indicating that changes to spiro-OMeTAD itself likely compete with effects due to the absorber to produce hysteretic behavior. These results show a clear way in which spiro-OMeTAD IFLs can contribute to hysteresis.

In summary, *operando* measurements of the charge transfer characteristics of spiro-OMeTAD-modified gold contacts illustrate that the same conditions that produce hysteresis in compete solar cells cause changes in the charge transfer properties of spiro-OMeTAD-modified contacts. Because the direction of change of each parameter measured is independent of the sign or magnitude of applied voltage, we believe these changes could be due to trap filling in the spiro-OMeTAD film. Further, films that contain Co-TFSI in addition to Li-TFSI induce larger decreases in J_{0n} and therefore increases in $V_{oc}^{(NH)}$ than when Li-TFSI alone is used. This could be due to interactions between Co-TFSI and *t*-BP, a higher spiro-OMeTAD$^{\bullet+}$ concentration, or simply a higher overall salt concentration. This increased response to operation in the presence of Co-TFSI could in fact contribute to observed increases in V_{oc} of complete solar cells when Co-TFSI is used *vs.* when it is not. If the current-voltage characteristics of these photovoltaics are measured without considering hysteresis, operation of the cell to collect the current-voltage curve could in fact artificially inflate the V_{oc} due to changes in charge transfer properties induced by the measurement itself.

This idea illustrates the importance of understanding the role of spiro-OMeTAD and its additives in both charge transfer and hysteresis behavior. In order to accurately measure the performance of solar cells that demonstrate hysteretic behavior, it is important to know all the different factors that contribute to hysteresis to account for them in the measurement. Thus, our finding that spiro-OMeTAD with Li-TFSI and with both Li- and Co-TFSI contribute to hysteresis by decreasing the electron collection ability of a gold hole contact is just one of many processes occuring in multiple parts of the cell that combine to cause overall hysteresis behaviors.

CHAPTER VIII

CONCLUSION

In this dissertation, quantitative charge transfer, selectivity, and recombination characteristics of IFL-modified solar cell contacts have been presented. Charge transfer is quantified using the equilibrium exchange current density (J_0) for both charge carriers. The relation of these J_0 values to precise definitions of selectivity and recombination and their impact on the important photovoltaic performance metric, the open-circuit voltage (V_{oc}), have also been shown. These results and the insights gained from them can inform the rational design of solar cell contacts for improved efficiencies.

The J_0 describes the magnitude of charge carriers crossing the interface per unit area at dynamic equilibrium. We define selectivity and recombination in terms of these quantities for both the electron and hole. Contact selectivity is the ratio of the two J_0 values at one contact, *e.g.*, J_{0p}/J_{0n} is the contact hole selectivity, while carrier selectivity is the ratio of the J_0 values for the same carrier at the two contacts. Recombination is $(J_{0n}J_{0p})^{0.5}$, which is the geometric average of both carrier collection rates.

Using theory developed by our group, we show two regimes where V_{oc} depends on the J_0 values differently. In the regime where the majority of the interfacial layer (IFL)-modified contacts investigated in this work operate, the V_{oc} depends on the light-limited carrier selectivity. In practice, this means that changes in the J_{0n} of the hole contacts studied herein dictate changes in the V_{oc}. In the other regime, V_{oc} depends on the contact selectivity. For the systems studied herein, shifts in recombination do not directly lead to changes in V_{oc}. However, they can lend insight into chemical changes, and, in other absorber systems, changes in recombination could lead to changes in V_{oc}. Thus, depending on the materials

in use, understanding how an IFL affects contact recombination can often be vital information for improving efficiency.

While theoretical knowledge of these relationships is important as a framework for understanding IFL-modified contacts, the specific aim of this work was to measure J_0 values for real IFL-modified contacts using experiments and numerical simulation. Our unique approach to measuring the properties of IFL-modified contacts utilizes the interdigitated back-contact silicon solar cell, which provides a three-in-one photovoltaic where the characteristics of the contact under study may be measured when it acts separately as a hole contact, electron contact, and recombination center. The results of using this platform to measure the selectivity and recombination characteristics of IFL-modified contacts may then be compared to numerical simulation results generated with known J_0 values. This comparison enables the determination of the J_0 values responsible for measured experimental behavior.

Using this platform, I show the charge transfer, selectivity, and recombination characteristics of gold contacts modified with the most common "hole selective" IFL used in perovskite solar cells, spiro-OMeTAD. Further, I show how its most common additives, Li-TFSI, Co-TFSI, and *t*-BP impact these properties and how they relate to the V_{oc} when spiro-OMeTAD-modified gold acts as the hole contact. Spiro-OMeTAD IFLs decrease the recombination of gold contacts by four orders of magnitude. The addition of Li-TFSI, Co-TFSI, both, and air exposure tune the contact selectivity in conjunction with the generation of spiro-OMeTAD$^{\bullet+}$, increasing J_{0p}/J_{0n} by up to nine orders of magnitude. When only Co-TFSI is used, EPR spectra of solutions and UV-Vis measurements of films show significant spiro-OMeTAD$^{\bullet+}$ formation, but at higher *t*-BP concentrations, the charge transfer

properties of spiro-OMeTAD-modified gold contacts with only Co-TFSI do not reflect these measurements. Further, when only Co- or Li-TFSI is used, the charge transfer properties are highly sensitive to the *t*-BP concentration, showing the quantitative impacts on charge transfer of *t*-BP complexation with metal ions (such as Li^+ or $Co^{2+/3+}$) or "quenching" of spiro-OMeTAD$^{\bullet+}$. However, when both salts are used, the charge transfer characteristics are much less sensitive to *t*-BP concentration.

This result, coupled with lower-than-expected contact hole selectivity for Co-TFSI-only samples, suggests that interactions between *t*-BP and Co-TFSI could be more complicated than those between *t*-BP and Li-TFSI. These findings also indicate that these interactions with Co-TFSI could have a larger impact on contact properties at higher *t*-BP concentrations (*i.e.*, those relevant to solar cells) than spiro-OMeTAD$^{\bullet+}$ itself when Co-TFSI is the only salt. When both salts are present, this enables the formation of significantly more spiro-OMeTAD$^{\bullet+}$ because *t*-BP is less available to interact with Li^+ and spiro-OMeTAD$^{\bullet+}$, leading both to the larger J_{0p}/J_{0n} we observe and the relative insensitivity to *t*-BP concentration when both salts are used.

Observed changes in charge transfer properties also translate to changes in V_{oc} when spiro-OMeTAD-modified gold acts as the hole contact. Compared to neat spiro-OMeTAD, the addition of both Li- and Co-TFSI results in an increase in the V_{oc} of about 240 mV due to the about four order-of-magnitude decrease in J_{0n}. However, this only leads to an increase in V_{oc} compared to bare gold of about 80 mV because the decrease in recombination almost entirely cancels out the work function (*i.e.*, contact hole selectivity) effect. These results illustrate the importance of measuring the charge transfer characteristics in addition to the V_{oc} in order to understand the complete picture of how

IFLs impact individual contact and complete solar cell properties for rational IFL/contact design.

Additionally, our unique *operando* measurements show that the role of Li- and Co-TFSI-containing spiro-OMeTAD in hysteresis behavior is to transiently decrease both J_{0n} and J_{0p} under solar cell operation conditions. These changes occur in the same direction independent of the sign or magnitude of the applied bias (*i.e.*, pre-measurement condition), indicating this behavior is likely due to trap filling in the film. This causes a transient increase in the V_{oc} when the spiro-OMeTAD-modified gold contact acts as the hole contact as a direct result of the decrease in J_{0n}. The addition of Co-TFSI increases the response compared to when only Li-TFSI is used, which could contribute to the observed increases in V_{oc} when Co-TFSI is used in spiro-OMeTAD in perovskite and SSDS solar cells if hysteresis is not accounted for when measuring solar cell performance. Further, because the direction of these changes is independent of the pre-measurement conditions, unlike in complete perovskite and SSDS cells, the contributions of spiro-OMeTAD IFLs to hysteresis likely compete with processes that occur in the absorber and at the other contact to generate overall hysteresis behavior.

The results presented in this dissertation answer lingering questions in the literature about the relative importance of electron and hole transfer when spiro-OMeTAD modifies gold contacts and the role(s) of its most commonly used additives. We find the electron blocking ability of doped spiro-OMeTAD to be the most important factor in dictating the V_{oc} when spiro-OMeTAD-modified gold acts as the hole contact in the cells studied herein. This, coupled with insights gained using *operando* measurements, illustrate that spiro-OMeTAD-modified gold contacts could be improved, for example, if the observed

decrease in J_{0n} during solar cell operation could somehow be harnessed as a permanent rather than transient characteristic. Engineering a method to achieve this would also negate spiro-OMeTAD's contribution to hysteresis, improving the stability of perovskite solar cells. Overall, these findings can help optimize the use of spiro-OMeTAD in perovskite and SSDS solar cells in particular and the use of IFLs in solar cells in general. This information will help the broad solar cell community to rationally develop interfacial layer and contact technologies for improved photovoltaic efficiencies and/or lower costs, ultimately decreasing humankind's dependence on nonrenewable energy sources.

APPENDIX A

MATERIALS AND METHODS

Silicon IBC solar cells were donated by SunPower and chemo-mechanically polished by Axus Technology to remove the silicon nitride antireflective coating and pyramidal texturing for ease of thin-film deposition. Cr/Au electrodes were thermally evaporated onto glass slides (cleaned in detergent in DI water, sonicated sequentially in acetone and isopropyl alcohol, then spun dry), onto which IBC devices were mounted with Loctite Hysol 1C epoxy. Before epoxy attachment, copper wires were connected to the IBC cell metal contacts to the n^+- and p^+-Si using silver epoxy. Silver paint was used to make contact between these copper wires and the gold electrodes on the glass, and white epoxy was used to protect metal components from further processing steps. The complete device making procedure is presented in detail in Appendix C.

Completed devices were immersed for 10 minutes in a solution of 5:1:1 18.2 MΩ cm deionized water to 29% w/w $NH_4OH_{(aq)}$ (Fisher Scientific, ACS grade) to 30% w/w $H_2O_{2(aq)}$ (EMD Millipore, ACS grade) at 50 ºC, then rinsed with DI water and dried with N_2. Next, oxide was etched with buffered oxide etch (5:1 $NH_4F_{(aq)}$ to $HF_{(aq)}$, J.T. Baker/Avantor) for one minute. Neat Spiro-OMeTAD (HPLC-grade, 99%, Sigma-Aldrich) films were spin coated onto the IBC cells in ambient conditions from 10 mg/mL solutions in chlorobenzene (anhydrous, 99.8%, Sigma-Aldrich) at 2000 rpm for 60 seconds to yield 3-5 nm films. Solutions were mixed and kept in air-free flasks under N_2 and in the dark until spun coating and filtered through 0.1 μm PTFE (GE/Whatman) directly before deposition.

Neat films were spin coated directly from 10 mg/mL neat spiro-OMeTAD solution

in chlorobenzene. The solution for neat films with *t*-BP was made by adding 8 μL *t*-BP (96%, Sigma-Aldrich) to 1 mL neat 10 mg/mL spiro-OMeTAD stock solution. Solutions for films with Li-TFSI in a 1:4 mole ratio to spiro-OMeTAD were made by adding 1.1 μL Li-TFSI (99.95%, Sigma-Aldrich, 107 mg/mL stock solution made in dry, HPLC-grade acetonitrile from Fisher Scientific) and 0.7 or 1.6 μL *t*-BP to 0.2 mL neat 10 mg/mL spiro-OMeTAD solution. Solutions for films with Co-TFSI in a 1:10 mole ratio (FK102, 98%, Sigma Aldrich) were made by adding 0.8 μL stock solution (280 mg/mL in acetonitrile) and either 0.9 or 1.6 μL *t*-BP to 0.2 mL stock 10 mg/mL spiro-OMeTAD solution. Solutions for films with Co-TFSI in a 1:5 mole ratio were made by adding 1.6 μL of stock solution and 1.6 μL *t*-BP to 0.2 mL stock spiro-OMeTAD solution. Solutions with both Li- and Co-TFSI were made by adding 1.1 μL Li-TFSI stock solution, 0.8 or 1.6 μL Co-TFSI stock solution, and 1.1, 1.6, or 2.1 μL t-BP to 0.2 mL stock spiro-OMeTAD solution. Film thicknesses were measured using a Zygo NewView 7300 optical profilometer.

Gold electrodes (50 nm) were thermally evaporated on the cell top and silver paint was used to create electrical contact for characterization. Electrical measurements were performed using a custom, modified Instec variable temperature vacuum/controlled atmosphere stage with 2.5 mm diameter aperture. Temperature is controlled using a liquid nitrogen feedthrough controlled by an Instec temperature controller and PID settings set through PID testing. PID settings are different at atmospheric pressure *vs.* at lower pressures. The temperature of the sample is measured using a LakeShore temperature diode clamped to the sample for the duration of the time course measurement. This temperature measurement is performed using a LakeShore 331 Temperature controller through the measurement automation code. Complete setup and measurement details are provided in

Appendices B and C.

Pressure inside the stage is controlled using a vacuum pump and nitrogen gas feed, the latter of which may be set to establish a particular pressure. Inert atmosphere is established over the course of five minutes by alternately pulling vacuum on the stage and backfilling with nitrogen. For time course samples, an initial measurement is first taken in air to confirm electrical continuity for all contacts. Then, an inert atmosphere is established directly after this measurement, and samples are measured for one hour in this atmosphere to provide a baseline for further measurements. Samples are then re-exposed to air for further measurement over six hours.

A ThorLabs 785 nm laser diode with collimating lens and circularizing prisms was used as the illumination source. The bulk silicon of the IBC cells is approximately 200 μm thick. Thus, when illuminating from the back, light with longer wavelengths (>800 nm) travels through the entire bulk of the silicon to encounter the top contact (the contact under study). There, it may reflect back into the cell if the top contact is a metal such as gold. Reflected light can then generate free carriers artificially close to the contact under study, thus leading to decreased sensitivity in the measurement of contact recombination. Light with shorter wavelengths (<800 nm) does not penetrate the silicon far enough to reach the top contact at significant intensities and therefore does not contribute to artifacts generated by longer wavelengths.

A 785 nm laser diode not only provides a means of limiting the wavelength of light but also enables tuning of the light intensity *via* the laser diode controller, which also maintains the temperature of the laser diode to ensure constant (correct) output. However, to make doubly sure that constant light intensity was output from the laser diode (as the

properties of the solar cell are rather sensitive to the intensity), an auxiliary silicon photodiode controlled by a Keithley 2400 source-measure unit was used to measure the light intensity of the laser beam. The light level was set by measuring a 2 mA short-circuit current between the n^+- and p^+-Si contacts of each freshly etched IBC device before addition of a film or/and top contact. At this illumination intensity, the absorber is under high injection conditions.

A Keithley 2400 source-measure unit, Keithley 7001 switching matrix, and ThorLabs filter wheel were used to measure the $I_{sc}^{(PN)}$, $V_{oc}^{(NH)}$, and $V_{oc}^{(PE)}$ *via* Python code automation. The stage possesses four probers for electrical measurements, which are connected to the Keithley 2400 through the switching matrix. The role of the latter is to control which contact pairs are connected for a given measurement (all three probers are in contact with their respective contacts throughout the entirety of the measurement). For example, when $I_{sc}^{(PN)}$ is measured, the switching matrix allows the source-measure unit to connect to only the two contacts needed to perform that measurement, *i.e.*, the n^+- and p^+-Si contacts on the back of the IBC cell. For the other two measurements, it does the same thing, but connects the top contact to only one or the other of the back contacts. The Keithley 2400 either sources 0 V and measures current in the case of $I_{sc}^{(PN)}$ or sources 0 A and measures voltage in the case of the V_{oc} values.

Voltage step samples were fabricated in the exact same manner as time course samples but were measured in air for 6 hours before being taken into N_2 for 90 minutes to establish a baseline for *operando* measurements. Voltage was applied between the n^+-Si contact and top contact for 60 seconds under illumination (at V_{app} = 0.8 V, V_{oc}, 0 V, or -0.8 V) while keeping the p^+ contact at open circuit while also measuring the resulting current

or voltage. The $V_{oc}^{(NH)}$, $V_{oc}^{(PE)}$, and $I_{sc}^{(PN)}$ were then measured over the next 3 hours.

Visible spectra were collected using a Perkin Elmer Lambda-1050 UV/Visible/NIR spectrophotometer and films were made in the same manner as described above but spin coated on glass instead of on IBC devices. Electron paramagnetic resonance spectra of solutions made in the same manner as described above were collected using a Bruker Elexsys E500 EPR spectrometer with 15 dB receiver gain, 5 G modulation amplitude, and at room temperature in quartz tubes.

APPENDIX B

EXPERIMENTAL SETUP AND MEASUREMENT DETAILS

I. Instec Stage Setup Description

The Instec Stage measurement platform for IBC samples consists of many different components working in harmony to enable automated electrical measurements of IBC cells under controlled atmosphere and sample temperature. The setup consists of:

1. Instec stage mounted on aluminum plate above the laser table with silver stage block with 2.5 mm diameter aperture and threaded holes for clamp attachment,
2. Four gold plated tungsten electrical probers (extras and different lengths are also provided) connected to BNC outputs,
3. Stage temperature control through liquid nitrogen feedthrough controlled and measured by the MK2000 temperature controller and stage temperature measurement/feedback through thermocouple probers in the silver block,
4. Auxiliary sample temperature measurement using Lake Shore diode connected to Lake Shore 331 temperature controller,
5. Laser diode illumination source and laser diode controller to illuminate the sample through the bottom of the stage and aperture,
6. Filter wheel to control when the sample is exposed to illumination,
7. Silicon photodiode to measure laser diode intensity through current measured by Keithley2400,
8. Switching matrix (Keithley7001) connected to prober BNCs to switch between contact pairs during automated measurements,
9. Keithley2400 for electrical measurements of contact pairs under test,

10. Liquid nitrogen dewar and tubing to supply liquid nitrogen to the stage,

11. Vacuum pump and valve to allow for controlled atmosphere inside the stage,

12. Nitrogen gas line and valve to aid controlled atmosphere inside the stage,

13. Pressure gauge to aid establishment of controlled atmosphere inside the stage.

Images of these components are shown in Figure 30. These components are controlled using Python code on the Linux Scientific computer in SuNRISE (room 076 CAMCOR). The four code files that are most important for the measurements I performed in my PhD work are called Isc_Voc.py, ivt_sweep_continuous_N2.py, volt_Isc_Voc.py, and

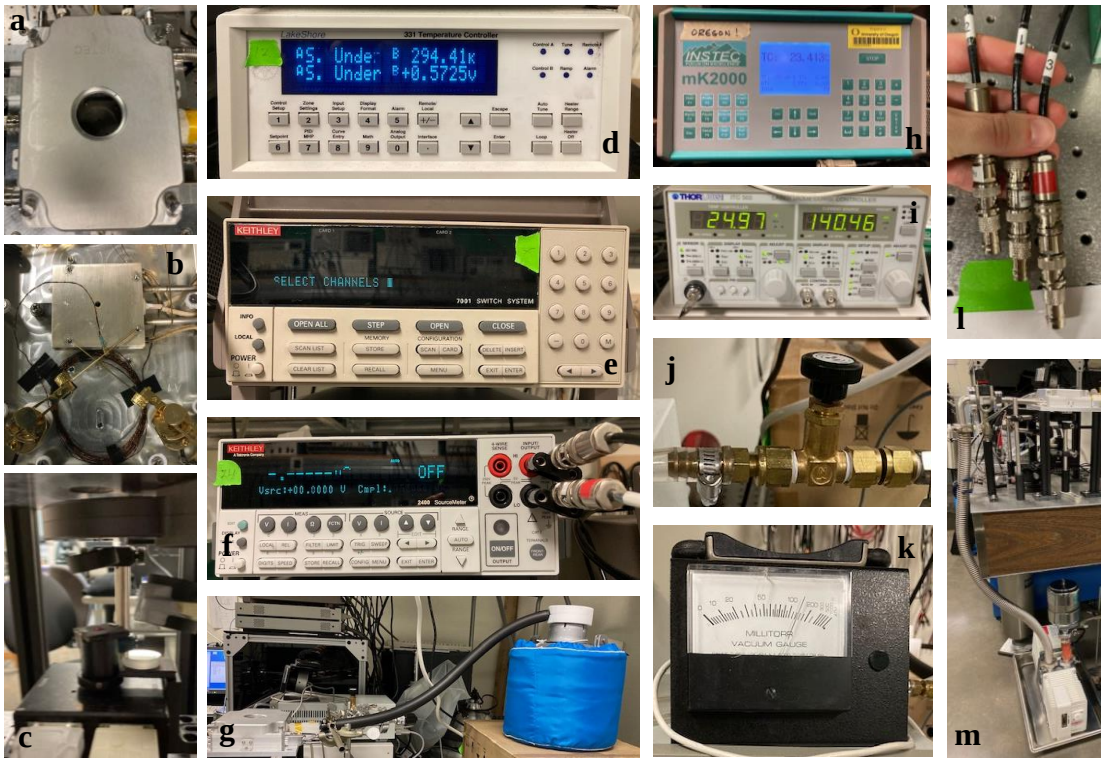

Figure 30. (a) Instec stage with lid on, (b) silver block stage with aperture, probers, tapped holes, auxiliary temperature measurement diode, feedthrough tubes, and stage thermocouple, (c) laser diode including optics, filter wheel, and silicon photodiode for intensity measurement, (d) Lake Shore 331 for auxiliary temperature measurement, (e) Keithley 7001 switching matrix, (f) Keithley 2400 SMU, (g) liquid nitrogen dewar connected to stage, (h) mK2000 temperature controller, (i) laser diode controller, (j) nitrogen gas valve, (k) pressure gauge, (l) BNCs to connect probers to switching matrix, and (m) vacuum pump connected to stage through vacuum valve.

curr_Isc_Voc.py which have accompanying text files called Isc_Voc.txt, ivt_sweep_continuous_N2.txt, volt_Isc_Voc.txt, and curr_Isc_Voc.txt. The Isc_Voc.measure() command measures the $I_{sc}^{(PN)}$, $V_{oc}^{(PE)}$, and $V_{oc}^{(NH)}$ of the IBC cell while controlling the temperature of the sample/stage, the contact pair under test during each measurement, the number of total measurements, and the time between measurements, also only allowing the sample to be exposed to illumination for the time necessary to measure the three electrical characteristics. The total length of the measurement is determined by setting both the number of measurements and time between them in the text file ("num meas" and "btw time").

The ivt_sweep_continuous_N2.measureivt() command sweeps an IV curve of the designated contact pair or list of contact pairs. It does not control the filter wheel, however, which must be set to the desired position (open or closed) before the command is given to run the code. The volt_Isc_Voc.measure() and curr_Isc_Voc.measure() commands are used to perform *operando* measurements. In the text file, the contact pair under test is specified (in my case, this was always the nt contact pair because we were interested in the action of the spiro-OMeTAD-modified gold contact as the hole contact), as is the number of voltage or current measurements to be applied to the contact pair under test during the *operando* measurement. The number of these measurements also determines the amount of time the contact will be operated. I use 300 measurements to operate the cell with the desired contact pair for about 60 s. This code also performs automated measurements of the three electrical characteristics after the operation event occurs. Just like with the Isc_Voc measurement, one simply enters the desired number of measurements and time between them. I typically perform 180 measurements every minute which is overkill (we

have only been using the first 30 or so minutes), but ensures I capture the entire response of each characteristic.

Appendix C provides instructions on how to make IBC cell devices and samples and how to perform measurements using the stage and commands in the Python shell. Here, the following pages show the Python code I wrote for these four files and their accompanying text files. In developing the original versions of these scripts, I received significant help and guidance from Dr. Wes Miller and Dr. Ellis Roe. In 2019 I edited and retooled the original versions on my own to incorporate new functionality.

Because this is text code, it is not presented in figures but rather as body text (beginning on the next page). Each code file and text file is, however, titled with its name. Further, the coloration is maintained from the original Python code text. Red text is comments, orange is commands, black is definitions or calls, blue is the actual measurement command, green is text to be written to the data file or returned in Idle as a command to the operator, and purple is text with internal definitions. The first code file shown in Isc_Voc, the next is ivt_sweep_continuous_N2, then volt_Isc_Voc, then curr_Isc_Voc. The accompanying text file called by the code is shown directly after the code it corresponds to.

II. I_{sc} and V_{oc} measurement Python code text

```
## Isc_Voc.py
## Original written by: D.W. Miller & K. Egelhofer 28-11-2017
## Last edited: 27 April 2019 to measure LD intensity with PD in addition
## to measuring Isc and Voc of the sample under test

import keithley2400 as k2400
import mk2000 as mk
import numpy
import time
import os
import ivfunctions
import datetime
import shutil
import lakeshore331 as ls331
import keithley7001 as k7001
import fwl02c as fw

## Performs a current vs. voltage measurement and probes sample temp throughout
## using a thermocouple probe via the Lakeshore331; uses a switching matrix
## to switch between measuring 3 different pairs of contacts on the sample (p/top,
## n/top, and p/n).

def measure():

    ## initialize mk2000
    mk.gettemp()
    time.sleep(1.0)
    mk.gettemp()

    ## get the date
    date = datetime.date.today()

    ## get the filename
    name = raw_input('Enter sample name:\n')
    directory = 'ivt_KE' + '/' + str(name) + '_' + str(date)

    ## make the directory
    os.mkdir( directory )

    ## copy the cv.txt file to the new directory
    shutil.copy( 'Isc_Voc.txt', directory + '/Isc_Voc.txt' )

    ## read in the experiment parameters stored in the ivt_Jsc_Voc.txt file
    params = ivfunctions.getIscVocparams( directory + '/Isc_Voc.txt' )

    initemp = params[0]
    fintemp = params[1]
    numsteps = params[2]
    k2400address = params[3]
    ls331address = params[4]
    k7001address = params[5]
    samplelist = params[6].split(',')
    numsweeps = params[7]
    btwtime = params[8]
    fwnum = params[9]
    k2400address2 = params[10]

    ## initialize keithley2400#1
    k2400.initialize(k2400address)
    k2400.setcurrentlimit(k2400address,0.02)
    ## initialize keithley2400#2
    k2400.initialize(k2400address2)
    k2400.setcurrentlimit(k2400address2,0.0001)

    ## contact routing syntax is
    ## '(@ cardnumber!rownumber!columnnumber, cardnumber!rownumber!columnnumber)'
    ## code assumes that
    ## source measure unit (SMU) is connected to 'rows out' cable set and the
    ## device(s) under test (DUTs) are connected to the 'columns in' cable
    ## keithley SMU should always have hi connected to 'rows out' 1
    ## and low to rows out 2
    ## DUT should have contacts connected to
    ## 'columns in' #1 through len(samplelist)
    ## Define list of contact routes
    ## change this to change order in which things are measured...
    routelist = ['(@ 1!1!1, 1!2!3)', '(@ 1!1!2, 1!2!3)','(@ 1!1!1, 1!2!2)']

    numsweeps = numpy.linspace(1,numsweeps,numsweeps)
```

```
## have the user check their contact connections before starting measurement
for i in range(len(samplelist)):
    print(str(samplelist[i]) + ' should be connected to:')
    columninhigh = routelist[i][7]
    columninlow = routelist[i][-2]
    print(str(columninhigh) + ' and ' + str(columninlow) + '.')

inittime = time.time()

## initialize temperature array
temperatures = numpy.linspace(initemp,fintemp,numsteps)

## initialize Jsc/Voc and measured temperature arrays
Isc = numpy.zeros([len(temperatures),len(numsweeps)])
V = numpy.zeros([len(temperatures),len(numsweeps)])
Ipd = numpy.zeros([len(temperatures),len(numsweeps)])

## make a data file to write the current data to
f = open( directory + '/' + str(name) + '_' + 'pn.dat', 'a' )
f.write('MeasNum\ttime/min\tIsc/mA' + '\n')
g = open( directory + '/' + str(name) + '_' + 'pt.dat', 'a' )
g.write('MeasNum\ttime/min\tVp/V' + '\n')
h = open( directory + '/' + str(name) + '_' + 'nt.dat', 'a' )
h.write('MeasNum\ttime/min\tVn/V' + '\n')
i = open( directory + '/' + str(name) + '_' + 'Ipd.dat', 'a' )
i.write('MeasNum\ttime/min\tIpd/A' + '\n')

dummy = raw_input('Connect the sample and press enter to begin measurement.')

## go to starting temperature
## settemp takes target temp and ramp rate in K/min
## equilibrate takes waittime in seconds and tolerance in K
mk.settempatmo( temperatures[0], 10)
mk.equilibrate(0.5,1.0)
nominaltemp = mk.gettemp()
countto5 = 0

while abs(nominaltemp-temperatures[0]) > 2:
    mk.settempatmo(temperatures[0], 10)
    print 'Still not at temperature, current temp is:'+str(nominaltemp)
    countto5 += 1
    if countto5 >= 5 :
        print 'Could not reach initial temperature.'
        print 'Check LN2 levels and restart measurement.'
        return
    time.sleep(60.0*abs(nominaltemp-temperatures[0])/10)
    mk.equilibrate(0.5,1.0)
    nominaltemp = mk.gettemp()

for t in range(len(temperatures)):

    ## set temperature and ramp, equilibrate at Jsc
    k2400.setvoltage(k2400address, 0.0)
    k2400.setvoltage(k2400address2, 0.0)
    mk.settempatmo(temperatures[t], 10)
    mk.equilibrate(0.5,1.0)
    ## wait for sample to achieve less than
    ## 1 K/second drift for ten consecutive seconds
    ## equilibrate takes tolerance (K) and waittime(seconds)
    ls331.equilibrate(1,1, ls331address, 'B')

    for p in range(len(numsweeps)):

        elaptime = (time.time() - inittime)/60
        fw.setfwpos(1, fwnum)

        k2400Ipd = k2400.getIsc(k2400address2)
        Ipd[t][p] = k2400Ipd
        i.write( str(numsweeps[p]) + '\t' + str(elaptime) + '\t' + str(k2400Ipd) + '\t' + '\n' )
        i.flush() ## store the data NOW!
        k2400.setvoltage(k2400address2, 0.0)
        k2400.setoutstate(k2400address2, 'OFF')

        for s in range(len(samplelist)):
            ## tell 7001 to open all the channels, then close the two channels
            ## that correspond to the contact pair to be measured
            k7001.opench(k7001address, 'all')
            ## set to appropriate contact pair
            k7001.closech(k7001address, routelist[s]) ##coding big league
```

```
                ## record actual sample temperature in K
                toptemp = ls331.gettemp(ls331address, 'B')

        ## use keithley 2400 getIsc function to measure the current
        ## write data to file right away

                if samplelist[s] == 'pt':
                    Voc = k2400.getVoc(k2400address)
                    V[t][p] = Voc
                    g.write( str(numsweeps[p]) + '\t' + str(elaptime) + '\t' +
                         str(Voc) + '\t' + '\n' )
                    g.flush() ## store the data NOW!

                if samplelist[s] == 'nt':
                    Voc = k2400.getVoc(k2400address)
                    V[t][p] = Voc
                    h.write( str(numsweeps[p]) + '\t' + str(elaptime) + '\t' +
                         str(Voc) + '\t' + '\n' )
                    h.flush() ## store the data NOW!

                if samplelist[s] == 'pn':
                    k2400Isc = k2400.getIsc(k2400address)
                    I = k2400Isc*1e3
                    Isc[t][p] = I
                    f.write( str(numsweeps[p]) + '\t' + str(elaptime) + '\t' +
                         str(I) + '\t' + '\n' )
                    f.flush() ## store the data NOW!

                ## turn off k2400 before waittime
                k2400.setvoltage(k2400address, 0.0)
                k2400.setoutstate(k2400address, 'OFF')

            ## Close FW for waittime
            fw.setfwpos(1,2)

            ## set time between "sweeps"; btwtime is given in minutes
            if numsweeps[p]/numsweeps[-1] == 1:
                time.sleep(0.0)
            if numsweeps[p]/numsweeps[-1] != 1:
                time.sleep(60.0*btwtime)

            ## End data line
            f.flush()
            g.flush()
            h.flush()
            i.flush()

        ## exit numsweeps loop

    ## all data is taken so close the files
    f.close()
    g.close()
    h.close()
    i.close()

    mk.stop()

    ## set sample to Jsc and turn off
    ## (which actually opens the circuit, I've checked -DWM)
    k2400.setvoltage(k2400address, 0.0)
    k2400.setoutstate(k2400address, 'OFF')
    k2400.setvoltage(k2400address2, 0.0)
    k2400.setoutstate(k2400address2, 'OFF')


    return

##---------------------------------------------------------------------------
```

III. I_{sc} and V_{oc} measurement text file

```
300     initial temperature     [K]
300     final temperature       [K]
1       number of steps         [K]
24      keithley2400 address    []
12      ls331 address           []
7       k7001 address           []
pT,nT,pn        sample list             []
1       num sweeps              []
0       btw time                []
3       fw num                  []
23      keithley2400 address2   []
```

IV. *IV* curve measurement Python code text

```
## ivt_sweep_N2.py
## Original written by: D.W. Miller & K. Egelhofer 28-11-2017
## Last edited: 11 May 2018 to be used without the filter wheel

import keithley2400 as k2400
import mk2000 as mk
import numpy
import time
import os
import ivfunctions
import datetime
import shutil
import lakeshore331 as ls331
import keithley7001 as k7001

## Performs a current vs. voltage measurement and probes sample temp throughout
## using a thermocouple probe via the Lakeshore331; adjusts generation rate via
## automated neutral density filter wheel thorlabs fw102c; uses a switching matrix
## to switch between measuring 3 different pairs of contacts on the sample (p/top,
## n/top, and p/n).

def measureivt():

    ## initialize mk2000
    mk.gettemp()
    time.sleep(1.0)
    mk.gettemp()

    ## get the date
    date = datetime.date.today()

    ## get the filename
    name = raw_input('Enter sample name:\n')
    directory = 'ivt_KE' + '/ivt_' + str(name) + '_' + str(date)

    ## make the directory
    os.mkdir( directory )

    ## copy the cv.txt file to the new directory
    shutil.copy( 'ivt_sweep_continuous_N2.txt', directory + '/ivt_sweep_continuous_N2.txt' )

    ## read in the experiment parameters stored in the cv.txt file
    params = ivfunctions.getivtcontinuoussweepparams( directory + '/ivt_sweep_continuous_N2.txt' )

    initemp = params[0]
    fintemp = params[1]
    numsteps = params[2]
    startstopvolt = params[3]
    maxvolt = params[4]
    minvolt = params[5]
    voltstep = params[6]
    area = params[7]
    k2400address = params[8]
    ls331address = params[9]
    k7001address = params[10]
    samplelist = params[11].split(',')
    irange = params[12]
    numcycles = params[13]
    ivcycles = params[14]
    numsweeps = params[15]

    ## contact routing syntax is
    ## '(@ cardnumber!rownumber!columnnumber, cardnumber!rownumber!columnnumber)'
    ## code assumes that
    ## source measure unit (SMU) is connected to 'rows out' cable set and the
    ## device(s) under test (DUTs) are connected to the 'columns in' cable
    ## keithley SMU should always have hi connected to 'rows out' 1
    ## and low to rows out 2
    ## DUT should have contacts connected to
    ## 'columns in' #1 through len(samplelist)
    ## Define list of contact routes
    ## change this to allow greater than 3 samples
    ## '(@ 1!1!1, 1!2!2)', '(@ 1!1!1, 1!2!3)', '(@ 1!1!2, 1!2!3)'
    routelist = ['(@ 1!1!1, 1!2!2)', '(@ 1!1!1, 1!2!3)', '(@ 1!1!2, 1!2!3)']
```

```
## make file names for the subdirectories to go in the overarching directory
## one each for: p/n, p/T, and n/T
subdirlist = []
subsubdirlist = []
numsweeps = numpy.linspace(1,numsweeps,numsweeps)

for p in range(len(numsweeps)):
    subdirlist.append( str(name) + '_' + str(numsweeps[p]) )
    os.mkdir( directory + '/' + str(name) + '_' + str(numsweeps[p]) )
    for i in range(len(samplelist)):
        subsubdirlist.append( str(name) + '_' + samplelist[i] )
        os.mkdir( directory + '/' + subdirlist[p] + '/' + subsubdirlist[-1] )

for i in range(len(samplelist)):
    print(str(samplelist[i]) + ' should be connected to:')
    columninhigh = routelist[i][7]
    columninlow = routelist[i][-2]
    print(str(columninhigh) + ' and ' + str(columninlow) + '.')

## initialize temperature and voltage arrays
temperatures = numpy.linspace(initemp,fintemp,numsteps)  ## set temps

if ((maxvolt-minvolt)/ voltstep) % 1 != 0:
    print('Measurement requires an integer number of volt steps')
    print('from maximum voltage to minimum voltage.')
    print('Measurement aborted.')
    return

##construct custom voltage list for hysteretic iv sweep
if startstopvolt > maxvolt or startstopvolt < minvolt:
    print('Start/stop volt must lie between maximum and minimum voltages.')
    print('Measurement aborted.')
    return

elif voltstep > 0:
    leg1 = numpy.arange(startstopvolt, maxvolt + voltstep, voltstep)
    leg2 = numpy.arange(maxvolt-voltstep, minvolt, -1.0*voltstep)
    leg3 = numpy.arange(minvolt, startstopvolt+voltstep, 1.0*voltstep)
    voltages = numpy.concatenate((leg1,leg2,leg3))
elif voltstep < 0:
    leg1 = numpy.arange(startstopvolt, minvolt + voltstep, voltstep)
    leg2 = numpy.arange(minvolt-voltstep, maxvolt, -1.0*voltstep)
    leg3 = numpy.arange(maxvolt, startstopvolt + voltstep, voltstep)
    voltages = numpy.concatenate((leg1,leg2,leg3))
else:
    print('Warning, volt step of zero makes no sense.')
    print('Measurement aborted.')
    return

## make list of numbers for number of iv cycles

numivcycles = numpy.linspace(1,ivcycles,ivcycles)

## initialize current and measured temperature arrays
I = numpy.zeros([len(temperatures),len(samplelist),len(numivcycles),len(voltages)])
kelvin = numpy.zeros([len(temperatures),len(samplelist),len(numivcycles),len(voltages)])

## initialize Voc and Jsc arrays
Vocs = numpy.zeros([len(temperatures),len(numivcycles),len(samplelist)])
Jscs = numpy.zeros([len(temperatures),len(numivcycles),len(samplelist)])

## open Voc and Jsc data file
for p in range(len(numsweeps)):
    for i in range(len(samplelist)):
        locals()["fvoc%02d" % (10*p+i) ] = open( directory + '/' + subdirlist[p] + '/'
                                            + subsubdirlist[i] + '/' + 'VocJsc.dat', 'a' )
```

```
    ##write header for Voc Jsc data file, loop over num iv cycles
        locals()["fvoc%02d" % (10*p+i) ].write('JVcycle\t')
        for x in range(len(numivcycles)):
            locals()["fvoc%02d" % (10*p+i) ].write(str(numivcycles[x])+'\t'+
                                    str(numivcycles[x])+'\t'
                                    +str(numivcycles[x])+'\t'
                                        +str(numivcycles[x])+'\t')
        locals()["fvoc%02d" % (10*p+i) ].write('\nT_s\t')
        for x in range(len(numivcycles)):
            locals()["fvoc%02d" % (10*p+i) ].write('T_m\tVoc\tJsc\tTime\t')
        locals()["fvoc%02d" % (10*p+i) ].write('\nK\t')
        for x in range(len(numivcycles)):
            locals()["fvoc%02d" % (10*p+i) ].write('K\tV\tmA/cm^2\tseconds\t')
        locals()["fvoc%02d" % (10*p+i) ].write('\n')

## must enter temperature/sample loop and collect data before continuing

dummy = raw_input('Connect the sample and press enter to begin measurement.')

## go to starting temperature
## settemp takes target temp and ramp rate in K/min
## equilibrate takes waittime in seconds and tolerance in K
mk.settempatmo( temperatures[0], 10)
mk.equilibrate(0.5,1.0)
nominaltemp = mk.gettemp()
countto5 = 0

while abs(nominaltemp-temperatures[0]) > 2:
    mk.settempatmo(temperatures[0], 10)
    print 'Still not at temperature, current temp is:'+str(nominaltemp)
    countto5 += 1
    if countto5 >= 5 :
        print 'Could not reach initial temperature.'
        print 'Check LN2 levels and restart measurement.'
        return
    time.sleep(60.0*abs(nominaltemp-temperatures[0])/10)
    mk.equilibrate(0.5,1.0)
    nominaltemp = mk.gettemp()

for t in range(len(temperatures)):
    ## open the data file for each contact pair in append mode
    for p in range(len(numsweeps)):
        for s in range(len(samplelist)):
            locals()["f%02d" % (10*p+s) ] = open( directory + '/' + subdirlist[p] + '/'
                            + subsubdirlist[s] + '/' + str(temperatures[t]) + '.dat', 'a' )

            ## write file header for this temperature/contact pair's data file
            locals()["f%02d" % (10*p+s) ].write('V\tJ\tT\tTime\t')
            locals()["f%02d" % (10*p+s) ].write('\nV\tmA/cm^2\tK\tseconds\t')
            locals()["f%02d" % (10*p+s) ].write('\n')

    ## set temperature and ramp, equilibrate at Jsc
    k2400.setvoltage(k2400address, 0.0)
    mk.settempatmo(temperatures[t], 10)
    mk.equilibrate(0.5,1.0)
    ## wait for sample to achieve less than
    ## 1 K/second drift for ten consecutive seconds
    ## equilibrate takes tolerance (K) and waittime(seconds)
    ls331.equilibrate(1,1, ls331address, 'B')

    ## enter switching loop to switch between samples
    inittime = time.time()
    for p in range(len(numsweeps)):
        for s in range(len(samplelist)):
            elaptime = time.time() - inittime
            ## tell 7001 to open all the channels, then close the two channels
            ## that correspond to the contact pair to be measured
            k7001.opench(k7001address, 'all')
            ## set to appropriate contact pair
            k7001.closech(k7001address, routelist[s]) ##coding big league

            ## here, loop over iv sweep in order to measure multiple JV curves
            for x in range(len(numivcycles)):

            ## use sweep function to measure current at each voltage in voltages

                ## record current in mA/cm^2
                k2400out = k2400.customsweep(k2400address, voltages,
                                    irange, numcycles)
```

```
                    ## record actual sample temperature in K
                    toptemp = ls331.gettemp(ls331address, 'B')

                    current = k2400out[1] * 1e3 / area

                    ## save current and temp data into data cubes
                    I[t][s][x] = current
                    kelvin[t][s][x] = numpy.ones(len(voltages))*toptemp

                    ## record measured current at each voltage and T for whole sweep
                    for v in range(len(voltages)):

                        ## write data to file
                        locals()["f%02d" % (10*p+s) ].write( str(voltages[v]) + '\t' +
                                            str(current[v]) + '\t' +
                                            str(toptemp) + '\t' + str(elaptime) + '\t' + '\n')
                        locals()["f%02d" % (10*p+s) ].flush() ## store the data NOW!


                ## exit voltage loop
                ## End data line; contains all the currents for this generation
                locals()["f%02d" % (10*p+s) ].flush()

            ## exit sample loop

        ## this tab level is in the temperature loop
        ## compute and store Voc, Jsc, and corresponding temperature
        ## loop over samples
            for s in range(len(samplelist)):
                locals()["fvoc%02d" % (10*p+s) ].write(str(temperatures[t])+'\t')

                ## compute average measured temp, Voc, and Jsc for this temperature
                for x in range(len(numivcycles)):
                    avtemp = numpy.median(kelvin[t][s][x])
                    Voc = voltages[numpy.argmin(abs(I[t][s][x]))]
                    Jsc = I[t][s][x][numpy.argmin(abs(voltages))]
             # write the values to the file
                    locals()["fvoc%02d" % (10*p+s) ].write(str(avtemp) + '\t' + str(Voc) + '\t'
                                        + str(Jsc) + '\t' + str(elaptime) + '\t')
                locals()["fvoc%02d" % (10*p+s) ].write('\n')
                locals()["fvoc%02d" % (10*p+s) ].flush()

                ## this file is complete so close and go to next temperature file
        locals()["f%02d" % (10*p+s) ].close()

    ## all data is taken, computed, and stored, close each Voc/Jsc file
    for s in range(len(samplelist)):
        locals()["fvoc%02d" % (10*p+s) ].close()

    ## measurement complete. Exit temperature loop.
    ## turn off temp control
    mk.stop()
    ## set sample to Jsc and turn off
    ## (which actually opens the circuit, I've checked -DWM)
    k2400.setvoltage(k2400address, 0.0)
    k2400.setoutstate(k2400address, 'OFF')

    return

##-------------------------------------------------------------------------------
```

V. *IV* curve measurement text file

```
300     initial temperature     [K]
300     final temperature       [K]
1       number of steps         [K]
0.0     start/stop voltage      [V]
1.0     max voltage             [V]
-1.0    min voltage             [V]
0.005   voltage step/initial direction  [V]
0.05    sample area             [cm^2]
24      keithley2400 address    []
12      ls331 address           []
7       k7001 address           []
pn      sample list             []
'AUTO'  current range           []
1.0     num PL cycles           []
1       num iv cycles           []
1       num sweeps              []
```

VI. *Operando* measurement with applied voltage Python code text

```
## volt_Isc_Voc.py
## Original written by: D.W. Miller & K. Egelhofer 28-11-2017
## Last edited: 27 April 2019 to measure LD intensity with PD in addition
## to measuring Isc and Voc of the sample under test (potential step application included)

import keithley2400 as k2400
import mk2000 as mk
import numpy
import time
import os
import ivfunctions
import datetime
import shutil
import lakeshore331 as ls331
import keithley7001 as k7001
import fwl02c as fw

## Performs a current vs. voltage measurement and probes sample temp throughout
## using a thermocouple probe via the Lakeshore331; uses a switching matrix
## to switch between measuring 3 different pairs of contacts on the sample (p/top,
## n/top, and p/n).

def measure():

    ## initialize mk2000
    mk.gettemp()
    time.sleep(1.0)
    mk.gettemp()

    ## get the date
    date = datetime.date.today()

    ## get the filename
    name = raw_input('Enter sample name:\n')
    directory = 'ivt_KE' + '/' + str(name) + '_' + str(date)

    ## make the directory
    os.mkdir( directory )

    ## copy the cv.txt file to the new directory
    shutil.copy( 'volt_Isc_Voc.txt', directory + '/volt_Isc_Voc.txt' )

    ## read in the experiment parameters stored in the ivt_Jsc_Voc.txt file
    params = ivfunctions.getvoltIscVocparams( directory + '/volt_Isc_Voc.txt' )

    initemp = params[0]
    fintemp = params[1]
    numsteps = params[2]
    k2400address = params[3]
    ls331address = params[4]
    k7001address = params[5]
    samplelist = params[6].split(',')
    voltsample = params[7].split(',')
    numcurrmeas = params[8]
    numsweeps = params[9]
    numvoltsweeps = params[10]
    btwtime = params[11]
    voltage = params[12]
    fwnum = params[13]
    k2400address2 = params[14]

    ## initialize keithley2400#1
    k2400.initialize(k2400address)
    k2400.setcurrentlimit(k2400address,0.02)
    ## initialize keithley2400#2
    k2400.initialize(k2400address2)
    k2400.setcurrentlimit(k2400address2,0.0001)

    ## contact routing syntax is
    ## '(@ cardnumber!rownumber!columnnumber, cardnumber!rownumber!columnnumber)'
    ## code assumes that
    ## source measure unit (SMU) is connected to 'rows out' cable set and the
    ## device(s) under test (DUTs) are connected to the 'columns in' cable
    ## keithley SMU should always have hi connected to 'rows out' 1
    ## and low to rows out 2
    ## DUT should have contacts connected to
    ## 'columns in' #1 through len(samplelist)
    ## Define list of contact routes
    ## change this to change order in which things are measured...
```

```
for c in range(len(voltsample)):
    if voltsample[c] == 'pvt':
        route = '(@ 1!1!1, 1!2!3)'
    if voltsample[c] == 'nvt':
        route = '(@ 1!1!2, 1!2!3)'
    if voltsample[c] == 'pvn':
        route = '(@ 1!1!1, 1!2!2)'

routelist = ['(@ 1!1!1, 1!2!3)', '(@ 1!1!2, 1!2!3)','(@ 1!1!1, 1!2!2)']

numsweeps = numpy.linspace(1,numsweeps,numsweeps)
numvoltsweeps = numpy.linspace(1,numvoltsweeps,numvoltsweeps)

## have the user check their contact connections before starting measurement
for i in range(len(samplelist)):
    print(str(samplelist[i]) + ' should be connected to:')
    columninhigh = routelist[i][7]
    columninlow = routelist[i][-2]
    print(str(columninhigh) + ' and ' + str(columninlow) + '.')

inittime = time.time()

## initialize temperature array
temperatures = numpy.linspace(initemp,fintemp,numsteps)
numcurrmeas = numpy.linspace(1,numcurrmeas,numcurrmeas)

## initialize Jsc/Voc and measured temperature arrays
Isc = numpy.zeros([len(temperatures),len(numsweeps)])
V = numpy.zeros([len(temperatures),len(numsweeps)])
Ipd = numpy.zeros([len(temperatures),len(numsweeps)])
Iv = numpy.zeros([len(temperatures),len(voltsample),len(numcurrmeas)])

## make a data file to write the current data to
e = open( directory + '/' + str(name) + '_' + 'curr_meas.dat', 'a' )
e.write('MeasNum\ttime/min\tI/mA' + '\n')
f = open( directory + '/' + str(name) + '_' + 'pn.dat', 'a' )
f.write('MeasNum\ttime/min\tIsc/mA' + '\n')
g = open( directory + '/' + str(name) + '_' + 'pt.dat', 'a' )
g.write('MeasNum\ttime/min\tVp/V' + '\n')
h = open( directory + '/' + str(name) + '_' + 'nt.dat', 'a' )
h.write('MeasNum\ttime/min\tVn/V' + '\n')
i = open( directory + '/' + str(name) + '_' + 'Ipd.dat', 'a' )
i.write('MeasNum\ttime/min\tIpd/A' + '\n')

dummy = raw_input('Connect the sample and press enter to begin measurement.')

## go to starting temperature
## settemp takes target temp and ramp rate in K/min
## equilibrate takes waittime in seconds and tolerance in K
mk.settempatmo( temperatures[0], 10)
mk.equilibrate(0.5,1.0)
nominaltemp = mk.gettemp()
countto5 = 0

while abs(nominaltemp-temperatures[0]) > 2:
    mk.settempatmo(temperatures[0], 10)
    print 'Still not at temperature, current temp is:'+str(nominaltemp)
    countto5 += 1
    if countto5 >= 5 :
        print 'Could not reach initial temperature.'
        print 'Check LN2 levels and restart measurement.'
        return
    time.sleep(60.0*abs(nominaltemp-temperatures[0])/10)
    mk.equilibrate(0.5,1.0)
    nominaltemp = mk.gettemp()

for t in range(len(temperatures)):

    ## set temperature and ramp, equilibrate at Jsc
    k2400.setvoltage(k2400address, 0.0)
    k2400.setvoltage(k2400address2, 0.0)
    mk.settempatmo(temperatures[t], 10)
    mk.equilibrate(0.5,1.0)
    ## wait for sample to achieve less than
    ## 1 K/second drift for ten consecutive seconds
    ## equilibrate takes tolerance (K) and waittime(seconds)
    ls331.equilibrate(1,1, ls331address, 'B')

    fw.setfwpos(1,fwnum)
```

```
## enter switching loop to switch between samples

for n in range(len(numvoltsweeps)):
    for c in range(len(voltsample)):

        ## tell 7001 to open all the channels, then close the two channels
        ## that correspond to the contact pair to be measured
        k7001.opench(k7001address, 'all')
        ## set to appropriate contact pair
        k7001.closech(k7001address, route)

        ## record actual sample temperature in K
        toptemp = ls331.gettemp(ls331address, 'B')

        ## here, loop over Jsc or Voc measurement in order to measure
        ## multiple values of Jsc or Voc for the contact pair under test

        for l in range(len(numcurrmeas)):

            elaptime = (time.time() - inittime)/60

        ## use keithley 2400 getspecCurr function
        ## to measure current over time while the SMU supplies the desired voltage
        ## write data to file right away

            if voltsample[c] == 'pvt':
                k2400I = k2400.getspecCurr(k2400address, voltage)
                Curr = k2400I*1e3
                Iv[t][c][l] = Curr
                e.write( str(numcurrmeas[l]) + '\t' + str(elaptime) + '\t' +
                         str(Curr) + '\t' + '\n' )
                e.flush() ## store the data NOW!

            if voltsample[c] == 'nvt':
                k2400I = k2400.getspecCurr(k2400address, voltage)
                Curr = k2400I*1e3
                Iv[t][c][l] = Curr
                e.write( str(numcurrmeas[l]) + '\t' + str(elaptime) + '\t' +
                         str(Curr) + '\t' + '\n' )
                e.flush() ## store the data NOW!

            if voltsample[c] == 'pvn':
                k2400I = k2400.getspecCurr(k2400address, voltage)
                Curr = k2400I*1e3
                Iv[t][c][l] = Curr
                e.write( str(numcurrmeas[l]) + '\t' + str(elaptime) + '\t' +
                         str(Curr) + '\t' + '\n' )
                e.flush() ## store the data NOW!

    ## this is the sample list loop level
    ## End data line; contains all the measurements for this contact pair cycle (?)
    e.flush()

    k2400.setvoltage(k2400address, 0.0)
    k2400.setoutstate(k2400address, 'OFF')

    ## switch filter wheel to block light again
    fw.setfwpos(1,2)

for p in range(len(numsweeps)):

    elaptime = (time.time() - inittime)/60
    fw.setfwpos(1, fwnum)

    k2400Ipd = k2400.getIsc(k2400address2)
    Ipd[t][p] = k2400Ipd
    i.write( str(numsweeps[p]) + '\t' + str(elaptime) + '\t' + str(k2400Ipd) + '\t' + '\n' )
    i.flush() ## store the data NOW!
    k2400.setvoltage(k2400address2, 0.0)
    k2400.setoutstate(k2400address2, 'OFF')

    for s in range(len(samplelist)):
        ## tell 7001 to open all the channels, then close the two channels
        ## that correspond to the contact pair to be measured
        k7001.opench(k7001address, 'all')
        ## set to appropriate contact pair
        k7001.closech(k7001address, routelist[s]) ##coding big league
```

```
            ## record actual sample temperature in K
            toptemp = ls331.gettemp(ls331address, 'B')

        ## use keithley 2400 getIsc function to measure the current
        ## write data to file right away

            if samplelist[s] == 'pt':
                Voc = k2400.getVoc(k2400address)
                V[t][p] = Voc
                g.write( str(numsweeps[p]) + '\t' + str(elaptime) + '\t' +
                     str(Voc) + '\t' + '\n' )
                g.flush() ## store the data NOW!

            if samplelist[s] == 'nt':
                Voc = k2400.getVoc(k2400address)
                V[t][p] = Voc
                h.write( str(numsweeps[p]) + '\t' + str(elaptime) + '\t' +
                     str(Voc) + '\t' + '\n' )
                h.flush() ## store the data NOW!

            if samplelist[s] == 'pn':
                k2400Isc = k2400.getIsc(k2400address)
                I = k2400Isc*1e3
                Isc[t][p] = I
                f.write( str(numsweeps[p]) + '\t' + str(elaptime) + '\t' +
                     str(I) + '\t' + '\n' )
                f.flush() ## store the data NOW!

                ## turn off k2400 before waittime
                k2400.setvoltage(k2400address, 0.0)
                k2400.setoutstate(k2400address, 'OFF')

            ## Close FW for waittime
            fw.setfwpos(1,2)

            ## set time between "sweeps"; btwtime is given in minutes
            if numsweeps[p]/numsweeps[-1] == 1:
                time.sleep(0.0)
            if numsweeps[p]/numsweeps[-1] != 1:
                time.sleep(60.0*btwtime)

            ## End data line
            f.flush()
            g.flush()
            h.flush()
            i.flush()

        ## exit numsweeps loop

    ## all data is taken so close the files
    f.close()
    g.close()
    h.close()
    i.close()

    mk.stop()

    ## set sample to Jsc and turn off
    ## (which actually opens the circuit, I've checked -DWM)
    k2400.setvoltage(k2400address, 0.0)
    k2400.setoutstate(k2400address, 'OFF')
    k2400.setvoltage(k2400address2, 0.0)
    k2400.setoutstate(k2400address2, 'OFF')


    return

##-------------------------------------------------------------------------------
```

VII. *Operando* measurement with applied voltage text file

```
300     initial temperature     [K]
300     final temperature       [K]
1       number of steps         [K]
24      keithley2400 address    []
12      ls331 address           []
7       k7001 address           []
pT,nT,pn        sample list             []
nvt     volt sample             []
300     num currmeas            []
60      num sweeps              []
1       num voltsweeps          []
1       btw time                []
-0.8    volt applied            []
3       fw num                  []
23      keithley2400 address2   []
```

VIII. *Operando* measurement with applied current Python code text

```
## curr_Isc_Voc.py
## Original written by: D.W. Miller & K. Egelhofer 28-11-2017
## Last edited: 11 May 2019 to measure LD intensity with PD in addition
## to measuring Isc and Voc of the sample under test (current application included)

import keithley2400 as k2400
import mk2000 as mk
import numpy
import time
import os
import ivfunctions
import datetime
import shutil
import lakeshore331 as ls331
import keithley7001 as k7001
import fwl02c as fw

## Performs a current vs. voltage measurement and probes sample temp throughout
## using a thermocouple probe via the Lakeshore331; uses a switching matrix
## to switch between measuring 3 different pairs of contacts on the sample (p/top,
## n/top, and p/n).

def measure():

    ## initialize mk2000
    mk.gettemp()
    time.sleep(1.0)
    mk.gettemp()

    ## get the date
    date = datetime.date.today()

    ## get the filename
    name = raw_input('Enter sample name:\n')
    directory = 'ivt_KE' + '/' + str(name) + '_' + str(date)

    ## make the directory
    os.mkdir( directory )

    ## copy the cv.txt file to the new directory
    shutil.copy( 'curr_Isc_Voc.txt', directory + '/curr_Isc_Voc.txt' )

    ## read in the experiment parameters stored in the ivt_Jsc_Voc.txt file
    params = ivfunctions.getcurrIscVocparams( directory + '/curr_Isc_Voc.txt' )

    initemp = params[0]
    fintemp = params[1]
    numsteps = params[2]
    k2400address = params[3]
    ls331address = params[4]
    k7001address = params[5]
    samplelist = params[6].split(',')
    voltsample = params[7].split(',')
    numcurrmeas = params[8]
    numsweeps = params[9]
    numvoltsweeps = params[10]
    btwtime = params[11]
    current = params[12]
    fwnum = params[13]
    k2400address2 = params[14]

    ## initialize keithley2400#1
    k2400.initialize(k2400address)
    k2400.setcurrentlimit(k2400address,0.02)
    ## initialize keithley2400#2
    k2400.initialize(k2400address2)
    k2400.setcurrentlimit(k2400address2,0.0001)

    ## contact routing syntax is
    ## '(@ cardnumber!rownumber!columnnumber, cardnumber!rownumber!columnnumber)'
    ## code assumes that
    ## source measure unit (SMU) is connected to 'rows out' cable set and the
    ## device(s) under test (DUTs) are connected to the 'columns in' cable
    ## keithley SMU should always have hi connected to 'rows out' 1
    ## and low to rows out 2
    ## DUT should have contacts connected to
    ## 'columns in' #1 through len(samplelist)
    ## Define list of contact routes
    ## change this to change order in which things are measured...
```

```
for c in range(len(voltsample)):
    if voltsample[c] == 'pvt':
        route = '(@ 1!1!1, 1!2!3)'
    if voltsample[c] == 'nvt':
        route = '(@ 1!1!2, 1!2!3)'
    if voltsample[c] == 'pvn':
        route = '(@ 1!1!1, 1!2!2)'

routelist = ['(@ 1!1!1, 1!2!3)', '(@ 1!1!2, 1!2!3)','(@ 1!1!1, 1!2!2)']

numsweeps = numpy.linspace(1,numsweeps,numsweeps)
numvoltsweeps = numpy.linspace(1,numvoltsweeps,numvoltsweeps)

## have the user check their contact connections before starting measurement
for i in range(len(samplelist)):
    print(str(samplelist[i]) + ' should be connected to:')
    columninhigh = routelist[i][7]
    columninlow = routelist[i][-2]
    print(str(columninhigh) + ' and ' + str(columninlow) + '.')

inittime = time.time()

## initialize temperature array
temperatures = numpy.linspace(initemp,fintemp,numsteps)
numcurrmeas = numpy.linspace(1,numcurrmeas,numcurrmeas)

## initialize Jsc/Voc and measured temperature arrays
Isc = numpy.zeros([len(temperatures),len(numsweeps)])
V = numpy.zeros([len(temperatures),len(numsweeps)])
Ipd = numpy.zeros([len(temperatures),len(numsweeps)])
Vi = numpy.zeros([len(temperatures),len(voltsample),len(numcurrmeas)])

## make a data file to write the current data to
e = open( directory + '/' + str(name) + '_' + 'volt_meas.dat', 'a' )
e.write('MeasNum\ttime/min\tVoc/V' + '\n')
f = open( directory + '/' + str(name) + '_' + 'pn.dat', 'a' )
f.write('MeasNum\ttime/min\tIsc/mA' + '\n')
g = open( directory + '/' + str(name) + '_' + 'pt.dat', 'a' )
g.write('MeasNum\ttime/min\tVp/V' + '\n')
n = open( directory + '/' + str(name) + '_' + 'nt.dat', 'a' )
h.write('MeasNum\ttime/min\tVn/V' + '\n')
i = open( directory + '/' + str(name) + '_' + 'Ipd.dat', 'a' )
i.write('MeasNum\ttime/min\tIpd/A' + '\n')

dummy = raw_input('Connect the sample and press enter to begin measurement.')

## go to starting temperature
## settemp takes target temp and ramp rate in K/min
## equilibrate takes waittime in seconds and tolerance in K
mk.settempatmo( temperatures[0], 10)
mk.equilibrate(0.5,1.0)
nominaltemp = mk.gettemp()
countto5 = 0

while abs(nominaltemp-temperatures[0]) > 2:
    mk.settempatmo(temperatures[0], 10)
    print 'Still not at temperature, current temp is:'+str(nominaltemp)
    countto5 += 1
    if countto5 >= 5 :
        print 'Could not reach initial temperature.'
        print 'Check LN2 levels and restart measurement.'
        return
    time.sleep(60.0*abs(nominaltemp-temperatures[0])/10)
    mk.equilibrate(0.5,1.0)
    nominaltemp = mk.gettemp()

for t in range(len(temperatures)):

    ## set temperature and ramp, equilibrate at Jsc
    k2400.setvoltage(k2400address, 0.0)
    k2400.setvoltage(k2400address2, 0.0)
    mk.settempatmo(temperatures[t], 10)
    mk.equilibrate(0.5,1.0)
    ## wait for sample to achieve less than
    ## 1 K/second drift for ten consecutive seconds
    ## equilibrate takes tolerance (K) and waittime(seconds)
    ls331.equilibrate(1,1, ls331address, 'B')

    fw.setfwpos(1,fwnum)
```

```
## enter switching loop to switch between samples

for n in range(len(numvoltsweeps)):
    for c in range(len(voltsample)):

        ## tell 7001 to open all the channels, then close the two channels
        ## that correspond to the contact pair to be measured
        k7001.opench(k700laddress, 'all')
        ## set to appropriate contact pair
        k7001.closech(k700laddress, route)

        ## record actual sample temperature in K
        toptemp = ls331.gettemp(ls331address, 'B')

        ## here, loop over Jsc or Voc measurement in order to measure
        ## multiple values of Jsc or Voc for the contact pair under test

        for l in range(len(numcurrmeas)):

            elaptime = (time.time() - inittime)/60

        ## use keithley 2400 getspecCurr function
        ## to measure current over time while the SMU supplies the desired voltage
        ## write data to file right away

            if voltsample[c] == 'pvt':
                k2400V = k2400.getspecVolt(k2400address, current)
                Vi[t][c][l] = k2400V
                e.write( str(numcurrmeas[l]) + '\t' + str(elaptime) + '\t' +
                         str(k2400V) + '\t' + '\n' )
                e.flush() ## store the data NOW!

            if voltsample[c] == 'nvt':
                k2400V = k2400.getspecVolt(k2400address, current)
                Vi[t][c][l] = k2400V
                e.write( str(numcurrmeas[l]) + '\t' + str(elaptime) + '\t' +
                         str(k2400V) + '\t' + '\n' )
                e.flush() ## store the data NOW!

            if voltsample[c] == 'pvn':
                k2400V = k2400.getspecVolt(k2400address, current)
                Vi[t][c][l] = k2400V
                e.write( str(numcurrmeas[l]) + '\t' + str(elaptime) + '\t' +
                         str(k2400V) + '\t' + '\n' )
                e.flush() ## store the data NOW!

    ## this is the sample list loop level
    ## End data line; contains all the measurements for this contact pair cycle (?)
    e.flush()

    k2400.setvoltage(k2400address, 0.0)
    k2400.setoutstate(k2400address, 'OFF')

    ## switch filter wheel to block light again
    fw.setfwpos(1,2)

for p in range(len(numsweeps)):

    elaptime = (time.time() - inittime)/60
    fw.setfwpos(1, fwnum)

    k2400Ipd = k2400.getIsc(k2400address2)
    Ipd[t][p] = k2400Ipd
    i.write( str(numsweeps[p]) + '\t' + str(elaptime) + '\t' + str(k2400Ipd) + '\t' + '\n' )
    i.flush() ## store the data NOW!
    k2400.setvoltage(k2400address2, 0.0)
    k2400.setoutstate(k2400address2, 'OFF')

    for s in range(len(samplelist)):
        ## tell 7001 to open all the channels, then close the two channels
        ## that correspond to the contact pair to be measured
        k7001.opench(k700laddress, 'all')
        ## set to appropriate contact pair
        k7001.closech(k700laddress, routelist[s]) ##coding big league

        ## record actual sample temperature in K
        toptemp = ls331.gettemp(ls331address, 'B')
```

```
        ## use keithley 2400 getIsc function to measure the current
        ## write data to file right away

                if samplelist[s] == 'pt':
                    Voc = k2400.getVoc(k2400address)
                    V[t][p] = Voc
                    g.write( str(numsweeps[p]) + '\t' + str(elaptime) + '\t' +
                         str(Voc) + '\t' + '\n' )
                    g.flush() ## store the data NOW!

                if samplelist[s] == 'nt':
                    Voc = k2400.getVoc(k2400address)
                    V[t][p] = Voc
                    h.write( str(numsweeps[p]) + '\t' + str(elaptime) + '\t' +
                         str(Voc) + '\t' + '\n' )
                    h.flush() ## store the data NOW!

                if samplelist[s] == 'pn':
                    k2400Isc = k2400.getIsc(k2400address)
                    I = k2400Isc*1e3
                    Isc[t][p] = I
                    f.write( str(numsweeps[p]) + '\t' + str(elaptime) + '\t' +
                         str(I) + '\t' + '\n' )
                    f.flush() ## store the data NOW!

                    ## turn off k2400 before waittime
                    k2400.setvoltage(k2400address, 0.0)
                    k2400.setoutstate(k2400address, 'OFF')

                ## Close FW for waittime
                fw.setfwpos(1,2)

                ## set time between "sweeps"; btwtime is given in minutes
                if numsweeps[p]/numsweeps[-1] == 1:
                    time.sleep(0.0)
                if numsweeps[p]/numsweeps[-1] != 1:
                    time.sleep(60.0*btwtime)

                ## End data line
                f.flush()
                g.flush()
                h.flush()
                i.flush()

        ## exit numsweeps loop

    ## all data is taken so close the files
    f.close()
    g.close()
    h.close()
    i.close()

    mk.stop()

    ## set sample to Jsc and turn off
    ## (which actually opens the circuit, I've checked -DWM)
    k2400.setvoltage(k2400address, 0.0)
    k2400.setoutstate(k2400address, 'OFF')
    k2400.setvoltage(k2400address2, 0.0)
    k2400.setoutstate(k2400address2, 'OFF')


    return

##-------------------------------------------------------------------------------
```

IX. *Operando* measurement with applied current text file

```
300     initial temperature     [K]
300     final temperature       [K]
1       number of steps         [K]
24      keithley2400 address    []
12      ls331 address           []
7       k7001 address           []
pT,nT,pn        sample list             []
nvt     volt sample             []
300     num currmeas            []
60      num sweeps              []
1       num voltsweeps          []
1       btw time                []
0.0     curr applied            []
3       fw num                  []
23      keithley2400 address2   []
```

APPENDIX C

SAMPLE PREPARATION DETAILS

The device and sample making procedure used throughout my doctoral research was adapted from a procedure developed by Dr. Chris Weber who worked with IBC cells in the Lonergan Lab before me. Though some aspects are similar to Dr. Weber's sample making processes, I altered essentially all processing steps in some manner due to using polished IBC cells rather than Dr. Weber's use of textured IBC cells. Using polished IBC cells requires further cleaning steps and therefore better protection of the interdigitated metal IBC contacts. In particular, using silver epoxy to connect the copper wires to the IBC contacts, using white epoxy to mount the IBC cell to the glass, and mounting the IBC cell with the silicon side up are new compared to Dr. Weber's device processing steps. My procedures for making samples are also different from Dr. Weber's, where I first clean the silicon using the basic Standard Clean 1, etch with buffered oxide etch, set the illumination intensity, and then perform another buffered oxide etch before depositing the film, none of which were necessary with textured IBC cells.

The following is a step-by-step procedure that describes the fabrication of the IBC cell devices used in my research, accompanied by photos. Further, it details the steps taken to deposit films on IBC devices to make a complete sample, and the necessary procedures to measure the desired properties of the sample. If using these instructions to make devices or samples, I would suggest reading through the instructions for the entire step you are on before proceeding. I would also suggest making dummy devices the first time as practice (*i.e.*, using dead IBC cells and mounting them on glass slides without gold contacts).

I. Substrate preparation

The goal is to generate clean, 1 square inch glass slides with Cr/Au contacts that will not lift off in the cleaning process of completed devices (SC1).

What you'll need:

1" x 3" glass slides (I use the Thermo Fisher ones from Science Stores)

Diamond scribe

Two rulers

Sonicator

Glass slide holders (2, there is one labeled "Acetone" and one "IPA")

Glass washing detergent

DI water

Two medium crystallization dishes

Acetone

Acetone wash bottle

IPA

IPA wash bottle

Spin coater

Teflon tweezers

Metal tweezers

Kim wipes

Evaporation masks

Kapton tape

Chromium

Gold

Ammonia

Hydrogen peroxide

SC1 crystallization dish, hot plate, and rinse dish (in spin coater hood)

1. Figure 31 shows the supplies necessary for making glass slides with chromium/gold contacts. Starting with the 1” x 3” glass slides, use the rulers and diamond scribe to make three 1” x 1” squares. I lay the slide along the larger ruler and the thinner ruler perpendicular and along the top of the slide, then use the scribe with medium pressure to draw one line at one inch and one at two inches. Pick up the slide and use medium pressure away from yourself with one thumb on each side of the scribe line to cleave the glass. Make 20.

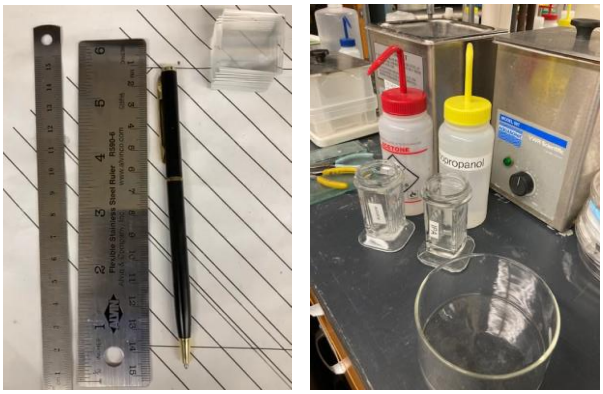

Figure 31. Supplies for making glass slides with chromium/gold contacts. Rulers, diamond scribe, and cleaved glass slides (left). Acetone and IPA wash bottles, slide holders, and medium crystallization dish (right).

2. Using one of the crystallization dishes, make a detergent solution with DI water (from the sink is fine, and a little detergent goes a long way!). Submerge the glass slides in the solution, swirl around with a gloved hand, and drain the solution. Rinse the slides with DI water until all detergent is removed, then fill with enough water in the dish to cover the slides.
3. Fill one glass slide holder with acetone and the other with IPA, about to the top of the grooves.

4. Using the Teflon tweezers, take a glass slide from the water and briefly rinse with acetone wash bottle into the empty crystallization dish (the “rinse” crystallization dish). Place the glass slide in the slide holder with acetone. Repeat to fill the slide holder. Ensure there is the correct amount of water in the sonicator (enough to cover the grooves of the slide holder but not so much that the slide holder floats or is in danger of falling over). Place slide holder in sonicator and turn on.
5. Turn on spin coater. Set speed to 5000 rpm and time to 10 seconds.
6. Figure 32 shows aspects of steps 6 – 11. On top of a large kim wipe, lay out masks. If small pieces of Kapton tape have not yet been cut, cut 24 2-3 mm strips, which will be used to affix the slides to the masks.
7. Remove slide holder from sonicator. Using Teflon tweezers, take a glass slide out and rinse with IPA into the rinse crystallization dish. Place slide in the IPA slide holder and repeat until all slides have been transferred. Place slide holder in the sonicator.

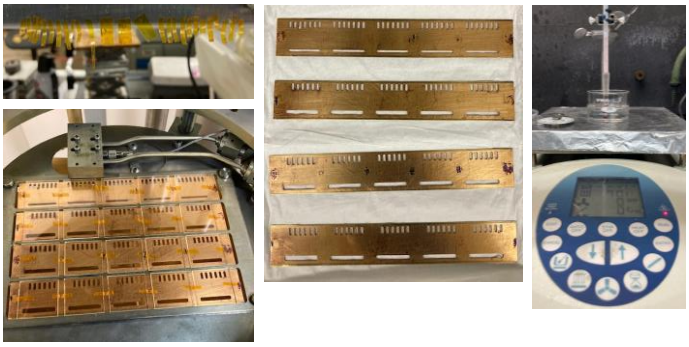

Figure 32. Kapton tape strips (top left), slides on masks in the evaporator (bottom left), evaporation masks before glass slide attachment (center), and SC1 solution on hot plate (right).

8. Fill the acetone slide holder with a fresh batch of slides from the DI water, rinsing each slide with acetone before placing it in the slide holder. Remove IPA slide holder from the sonicator and replace with acetone slide holder.

9. Bring IPA slide holder, Teflon tweezers, and a small kim wipe to the spin coater. Remove a slide from the holder with the tweezers and use the kim wipe to dry off ONLY the bottom side of the slide. Using a gloved hand, place the slide on the spin coater chuck, establish vacuum, and spin to dry. Being careful not to directly touch the top surface, use gloved hand to remove slide from chuck and place top side down on one of the evaporation masks. Repeat until all five slides are dry and placed on the same evaporation mask.
10. During down time (if any), open and prepare evaporator for chromium/gold evaporation.
11. Repeat steps 7-9 until all 20 glass slides are situated on evaporation masks. Use the Kapton take strips to affix the slides to the masks, using one piece on each end and one piece between every two slides. Gently place masks into slots in the evaporator.
12. Making sure to establish a substantial vacuum (I typically do a 20-minute rough pump and 45 minutes on high vac), evaporate ~5-10 nm chromium and then ~50 nm gold. Cool about 15-20 minutes.
13. While evaporator is cooling, remove crystallization dish from hot plate in spin coater hood and turn on the hot plate. It should be set to 70C, but if not, set the correct temperature as well. Make the SC1 solution using 20 mL DI water, 4 mL ammonia, and 4 mL hydrogen peroxide in the dish that was on the hot plate (this dish is used only for SC1). Swirl to ensure proper mixing and place in the center of the sharpie dots marked in the center of the hot plate. Lower thermometer into the solution so it is as submerged as possible without touching the bottom.
14. When cool, remove slides from the evaporator and choose one to test in the SC1.

When the SC1 has reached ~50-55C, set a 10-minute timer but don't start it yet. Use the Teflon tweezers to place the chosen slide into the SC1 then start the timer. When timer goes off, remove slide again with Teflon tweezers, rinse with DI water, and gently pat dry with a kim wipe.

15. Visually inspect the glass slide. There should be no significant degradation of the gold contacts. If there is…your chromium evaporation likely failed, and you will have to start over. If not, you're good to move on to the next steps.

II. Device making

The goal of making devices is to generate (mostly) flat, working IBC cell devices in which all metal components are protected from future cleaning steps.

What you'll need:

IBC wafers

Diamond scribe

2 rulers

Glass slides with gold contacts made in previous step

Device making station (microscope station near COMSOL computer office)

Extreme patience

1. Steps 1 – 7 are demonstrated in Figure 33. Start by cleaving IBC wafers. I make approximately 8 mm x 8 mm chips. Cleaving IBC cells takes extreme patience, and I cannot stress this enough. These things cleave VERY easily, and often in ways you don't want them to. So, be gentle, be patient, don't give up, and you'll get the hang of it with practice.

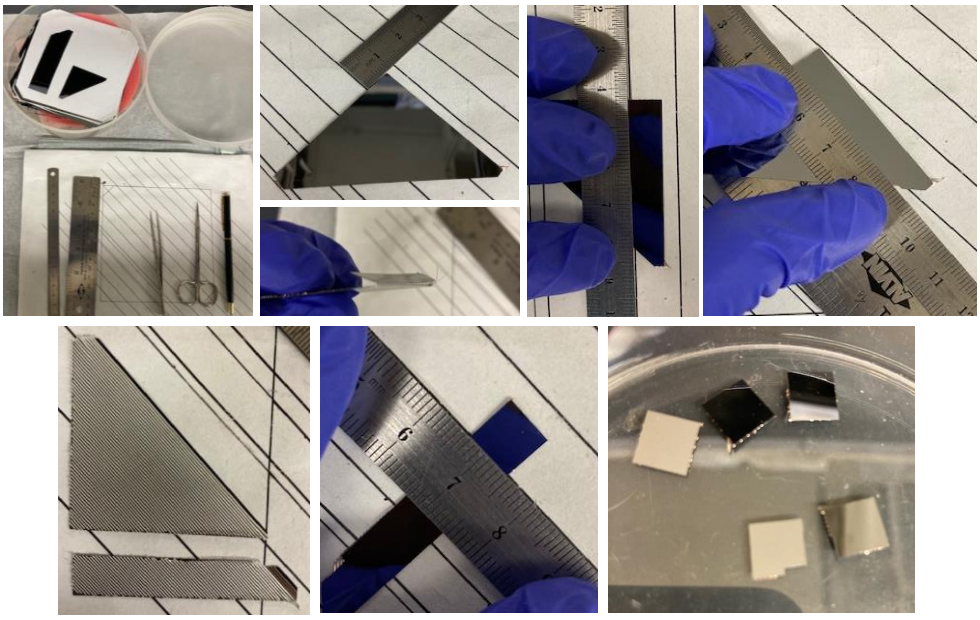

Figure 33. From top left to bottom right, IBC cleaving tools and steps.

2. Use the cleaving station next to the sonicator(s) and IBC wafers. The lines on the paper should be useful for sizing during the cleaving process. Typically, my approach is to cleave one long strip off the wafer, and then cleave smaller chips from that strip. I lay the IBC wafer silicon side up on the paper with the edge I want to cleave off parallel to the lines. Use the small and thin metal ruler to line up the edge 8 mm to the right of a line (if you are right-handed or use the scribe in your right hand, otherwise do the reverse). Then gently lay the ruler along the line on top of the wafer, apply gentle downward force spread along the ruler/wafer, and use gentle force to scribe the length of the wafer along the line.
3. Remove the ruler from the top and place the larger metal ruler with corked back on the paper cork side down. Set the wafer on top of this ruler, aligning the scribe line with the right edge (or left if you are left-handed). Gently place the smaller metal ruler over the top of the wafer along the right (left) edge of the bottom ruler near the scribe line. Align the ruler such that you can just barely see the scribe line. Apply gentle downward

pressure with the thumb and first two fingers of your left (right) hand along the length of this ruler to hold the wafer in place. Using the entire length of the forefinger of your right (left) hand, gently press down along the length of the IBC portion to be cleaved. You should hear/feel the wafer cleave, but the cleaved portion will not separate due to the contacts on the back.

4. Pick up the wafer. Apply gentle pressure to the edge of the portion to be cleaved to bend it toward the back side of the wafer. Gently bend the portion back and forth a few times, taking care not to twist the portion to be cleaved (this could cause those unwanted cleaves mentioned above). This is essentially like a loose tooth – the more it's wiggled, the looser it should get. These contacts sometimes break easily while other times do not. BE PATIENT. The goal here is to end up with a strip that is intact (no unwanted breakage) with the metal contacts still on the back. Both accidental cleaving and complete removal of the metal contacts result in unusable chips.
5. Once the strip is separated from the main wafer, set the main wafer aside. Use the same cleaving method to individually scribe and cleave correctly sized chips from the strip (~8 mm x 8 mm). Sometimes, the small scissors may be needed to sever any stubborn metal contacts. If you need to resort to this method, use extreme caution – scissors are an easy way to accidentally break chips.
6. Repeat this process until the desired number of intact chips with metal contacts still on the back is generated.
7. Using a plastic petri dish, move the chips to the device making station.
8. Steps 8 – 17 are demonstrated in Figure 34. At the device making station, there should be two pairs of metal tweezers, one with sharper, pointier ends than the other. The

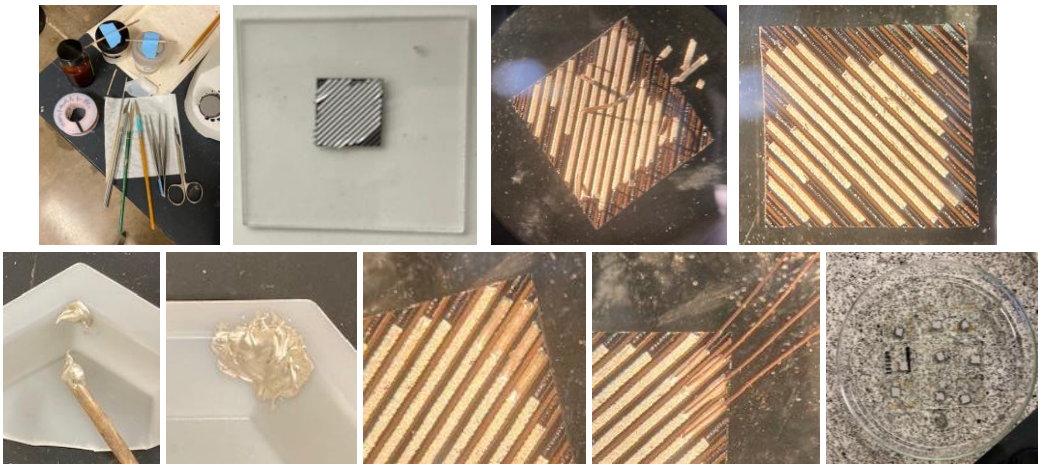

Figure 34. From top left to bottom right, tools necessary for and steps to attach copper wires to IBC contacts using silver epoxy.

former has blue tape on the handle while the latter does not. There is also a stack of 1" x 1" glass slides that are for use in device making. Turn the dial on the light all the way up to turn it on and adjust its position as necessary to ensure good lighting of the microscope subject.

9. Using the blue tape tweezers, gently place an IBC chip contact-side up on one of the glass slides then under the microscope. When handling IBC chips, be very careful not to drop them as this typically leads to breakage. Visually inspect the IBC chip under the microscope (pick it up with the tweezers if necessary) to ensure there are no cleaves that are not visible to the naked eye.
10. Still under the microscope and using the blue tape tweezers in your dominant hand and the other metal pair in your non-dominant hand, begin to clean up the messy contact edges. This process helps avoid shorts and damage to the silicon surface during further processing steps. Use your non-dominant hand to maintain gentle pressure on the IBC cell to prevent it from sliding around on the glass. Use the blue tape tweezers to gently lift a metal contact at the edge of the chip. There should be a point at which it no longer

lifts (don't tug too hard or the entire contact could rip off, you want to avoid this). Once lifted, take the end of the contact in the tweezers and gently wiggle it back and forth, keeping the end being wiggled in line with the contact, until it breaks off. Repeat on all contacts on the chip and on all chips in the batch. As chips are completed, move them (still on the glass slide) to one of the large glass petri dishes on the granite block to the right of the microscope.

11. The next step is to attach copper wires to the IBC contacts using silver epoxy. The copper wire and silver epoxy are both on the counter to the left of the microscope light. Use a small hexagonal plastic boat and the wooden applicators taped to their respective containers to get about equal amounts of the two silver epoxy components. A little goes a long way here – shoot for approximately the size of a match head of each component. Thoroughly mix the components using the applicator with the tapered end. Wipe the applicator clean with a kim wipe once mixed.
12. Cut ~1" pieces of the copper wire into a plastic petri dish using the small metal scissors at the station. You'll need 4 for each device plus a few extra.
13. Under the microscope, choose which four contacts you want to make contact to. Typically, I use four consecutive contacts that span as much of the chip as possible.
14. Use the blue tape tweezers to place four of the copper wires on a glass slide.
15. Working under the microscope and using the paint brush with the green handle, pick up a small amount of silver epoxy and carefully paint a small amount on the first contact of the four. Be very careful to not get the epoxy between the contacts. This usually results in bad devices. If a small amount gets on the silicon, put down the paint brush

and use the exacto knife to gently scrape the epoxy off the silicon to the best of your ability. It will not all come off, but less is better.

16. Once all four contacts have epoxy on them, wipe the paint brush with a kim wipe and use the blue tape tweezers to pick up a copper wire. Before attempting to place the copper wire on the silver epoxy, line the wire up off to the side of the desired contact, usually I do this somewhere to the left or right of the contacts with epoxy but still on the IBC cell, that way the wire ends up at the correct height. Once mocked up, carefully pick up the copper wire and gently place it so the end does not protrude too much past the silver epoxy (into the center of the device). You should be able to tell the wire is touching the silver epoxy, but don't squish it down too much yet. Perform this same step for all four copper wires, then use the tip of the blue tape tweezers to press the end of the wire in the epoxy down so that it forms good contact with the epoxy. Don't push too hard or the epoxy may spill over on to the IBC surface. Repeat for all four copper wires, then perform any additional cleanup as necessary with the exacto knife. Then, very gently and carefully (so the IBC cell doesn't slide off), move the glass slide holding the IBC cell to one of the larger glass petri dishes on the granite block. Repeat these steps for all planned devices, then put the petri dish with all devices in the hotter oven (100-140 C) for 20 minutes to cure the silver epoxy.
17. Once the silver epoxy is cured, check the devices under the microscope to ensure all contacts are still attached and no obvious shorts have occurred between contacts. Also test that the silver epoxy is cured by gently scraping at it with the exacto knife on one of the devices. If it is solid, you're good to go.
18. Figure 35 shows steps 18 – 29. Next, use a new hexagonal plastic boat to mix some

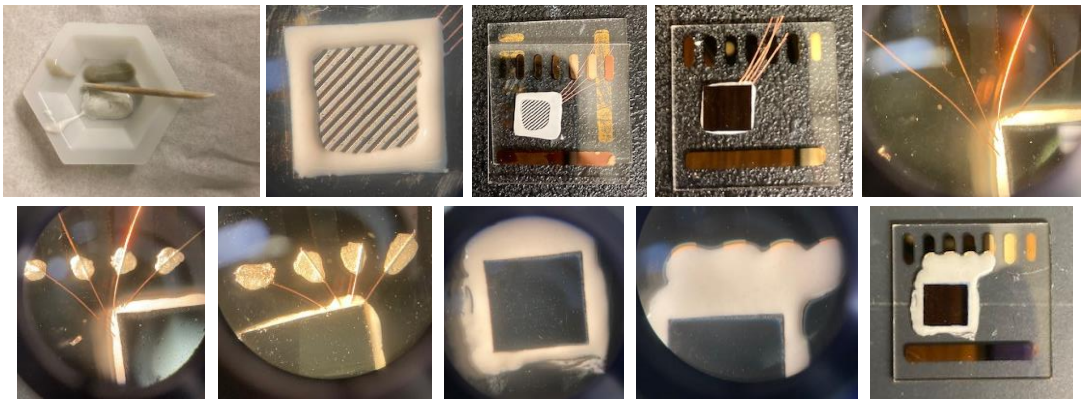

Figure 35. From top left to bottom right, steps for attaching IBC cell to glass slide with gold contacts using white epoxy, making electrical connection between copper wires and gold contacts using silver paint, and covering the cell with white epoxy.

white epoxy. This epoxy lives in the drawer beneath the microscope station. The mix ratio is based on the tube size – dispense equal lengths of epoxy into the boat, then mix thoroughly with the small wooden applicator. This epoxy has a short working time, but it should remain pliable enough for use on about 10 devices before new epoxy will need to be mixed.

19. The goal of this next step is to apply epoxy around the perimeter of the IBC cell on the contact side in order to attach the IBC cell to the glass with gold contacts but to still allow for illumination through the glass and contact side of the cell. This means epoxy must be applied with care to ensure enough IBC contacts are uncovered for illumination. Working under the microscope and with the larger tweezers in your non-dominant hand, gather a small amount of epoxy on the tapered end of the applicator. Applying gentle pressure with the tweezers to hold the IBC cell in place, apply epoxy to the perimeter of the contact side of the cell using short dabbing motions with the applicator. Be careful not to get epoxy on the glass as this can transfer to the IBC surface and cause issues down the line. Turn the glass slide as necessary. I find it best to apply the epoxy left to right or top to bottom, rather than right to left or bottom to

top. The applied epoxy should extend into the IBC cell center no more than about a fifth of the width of the cell. Much more and the epoxy will cover too much of the contact surface when the IBC cell is mounted to the glass.

20. When all four edges have epoxy, take a glass slide with gold contacts and flip upside down in your fingers. Using both hands (typically I hold the four corners of the slide with my index fingers and thumbs), align the slide over the IBC cell such that the copper wires point toward the smaller gold contacts and the chip is not directly in the center of the glass (this is important for placement of the temperature diode on the glass surface during sample measurement). In a controlled manner, lower the glass slide onto the IBC cell until the cell sticks. Flip the slide over and apply gentle pressure to the top of the IBC cell to ensure it is securely attached, but without cracking the cell. Set the device in a large glass petri dish.
21. Repeat these steps for all devices to be made, mixing more epoxy if needed. Let the devices rest for about 30 minutes before moving on to the next fabrication step. This allows the epoxy to cure enough that the devices will not move around as you attempt to complete the next step, but a full cure is not yet needed.
22. Use the blue tape tweezers to position individual copper wires over individual gold contacts on the glass. Make sure the copper wires do not cross or touch each other.
23. Shake the silver paint well, then using the paint brush with the teal tape, apply a small dab of silver paint to connect each copper wire to its gold contact on the “bottom” part of the gold contact (the part closer to the IBC cell). Try not to cover more than about half of the gold contact with silver paint and be sure not to cover the entire thing. Again, ensure the silver paint for each copper wire is separated from all others. Gently press

the copper wire against the glass with the blue tape tweezers after silver paint is applied if the wire is not already flush with the glass. This helps ensure electrical contact. Place the device in a large glass petri dish once all four copper wires are attached to their contacts with the silver paint. Repeat steps for all devices being made, then place the petri dish in the cooler oven (60 C) for 20 minutes to harden the silver paint.

24. Upon removing devices from the oven, inspect under the microscope. Using the exacto knife, trim excess copper wire protruding from the silver paint on the side toward the edge of the glass slide. This ensures good epoxy coverage in the next step.
25. Once all copper wires are trimmed, mix a new batch of white epoxy, this time to be used to cover the exposed copper wires, silver paint, and edges of the IBC cell. Though a less precise step than some of the others, be sure not to get epoxy on the surface of the IBC cell. Though it can be mostly removed before curing, it is better to maintain as pristine as possible of a silicon surface for later film deposition.
26. Again using the tapered end of the wooden applicator, cover the exposed copper wires and silver paint with the epoxy. I use small circular motions farther from the IBC cell and small dabbing motions closer to the cell as in the previous epoxy step. Be sure not to cover the entire gold contact in epoxy. The exposed gold contact is necessary to perform electrical measurements, but it is also necessary to completely cover other exposed metal components in the white epoxy to prevent them from being destroyed during the SC1 cleaning step (Cr/Au should be inert to SC1, as tested after deposition).
27. Once the contact area is covered, move on to the edges. Using small dabbing motions, again from top to bottom or left to right (if right-hand dominant), draw the epoxy up to the edge of the silicon without getting it on the surface. This prevents the SC1 from

getting under the edges and destroying the IBC's back contacts. Once everything is covered, I like to go back and clean up around the edges of the epoxy using the exacto knife. This is not strictly necessary but helps with the ability to place the temperature diode on the glass surface with fewer location restrictions. If any bubbles appear in the epoxy, use the tip of the exacto knife to gently work them out. Apply more epoxy if necessary.

28. When this epoxy step has been completed for all devices in the batch, cover the petri dish and let the devices sit for 30 minutes before transferring them to the cooler oven for 2 hours. The 30 minutes room temperature cure prevents running of the epoxy when the devices are transferred to the oven. Two hours will provide a complete cure at 60 C but if the temperature is different, be sure to adjust the cure time appropriately – there is additional cure information for this epoxy online.
29. Once cured, remove devices from oven and let cool. Using a fine point sharpie, label them on the bottom, under the large gold contact, with device numbers and bring downstairs for testing.
30. For testing, you'll need liquid nitrogen to control the temperature of the sample on the Instec stage.
31. Figure 36 illustrates steps 31 – 36. Refer to Appendix II for more a detailed description of how to use the Instec stage. Turn the laser diode current up to about 150 mA. Unscrew the captive screws on the lid of the stage. They will be loose when completely unscrewed but will not come off. Close the valve connecting the stage to the pump. Make sure the nitrogen valve on the wall is open to the clear hose on the right (which is the nitrogen that supplies the stage). Briefly open the nitrogen valve at the stage to

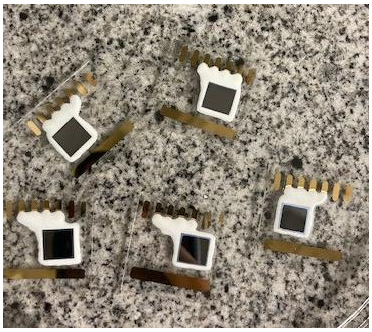

```
>>> mk.settempatmo(300,10)
>>> fw.setfwpos(1,3)
Changing Neutral Density Filter Wheel #1 to
Position #3 (ND 0.3)
>>> mk.stop()
>>> ivt_sweep_continuous_N2.measureivt()
Enter sample name:
KE3_155p1_1A_test
pn should be connected to:
1 and 2
Connect to sample and press enter to begin
measurement
```

Figure 36. Steps for testing IBC devices. Completed devices (left), device being tested in the stage (center), and commands and code responses in device testing in Python Shell (right). See Appendix B for Python code text.

reestablish atmospheric pressure in the stage. Close the valve and remove the stage lid. Fill the Instec liquid nitrogen dewar and place the carbon fiber sheathed hose inside, then place the dewar on the cardboard box.

32. Turn on the computer monitor on the right. If the Python Shell is not open, use the computer's terminal to open Idle using the command "idle &". In the shell, if not newly opening it, restart it by hitting ctrl F6. Import the necessary programs: "import FW102c as fw", "import ivt_sweep_continuous_N2", "import keithley7001 as k7001", "import mk2000 as mk". These will allow you to control the temperature, contact pair under test, whether the sample is being illuminated, and the actual measurement. If the text file for ivt_sweep_continuous_N2 (ivt_sweep_continuous_N2.txt) is not yet open, open it from the cohenlab main folder. Make sure where it says "contact pair" the entered value is "pn". Set the temperature of the stage to room temp by entering "mk.settempatmo(300,10)", then place the first device to be tested on the stage, centering the IBC cell over the aperture as best as you can (but don't spend too much time doing it because you will adjust it in a minute anyway).
33. Check which probers are connected to which BNC cables. The BNC connection for each prober comes off the stage on the outside at the location nearest that prober. Make

sure the two probers in use are connected to BNCs 1 and 2 (the p contact is designated 1 and the n is designated 2 in my setup). Place the probers on the two gold contacts either on the left or the right of the four that are contacted to the IBC cell.

34. Look at the switching matrix (Keithley7001) front panel and verify it has "---" at the 1,1 and 2,2 positions. This ensures the Keithley2400 is connected to BNCs 1 and 2 and will supply current/voltage to the correct contact pair. If there are no closed connections indicated or they are in different positions, use the commands "k7001.opench(7, "All")" and then "k7001.closech(7, "@ 1!1!1, 1!2!2")" to close the correct connections. On the Keithley2400 front panel, set it to local mode and to source 0 V and measure current.
35. In the Python shell, use the command "fw.setfwpos(1,1)" to open the filter wheel and illuminate the IBC cell. Hit the "ON/OFF" button on the Keithley2400 front panel to see what kind of current the cell is producing. If the current is positive, turn off the Keithley and switch the BNCs at their connections on the laser table. This will ensure that reverse bias is always negative and forward always positive. Turn the Keithley back on if you turned it off, then gently move the IBC device around on the stage until maximum current is achieved. Next, dial the laser diode current until it reaches -2 mA. To test the function of the device, there are a few things to consider. The first is how high the laser diode intensity must be to achieve -2 mA. Note the laser diode current in your notebook. The second is how much current is passed in reverse bias at -1 V. Ideally, we'd like this value to be as close as possible to the value at short circuit (0 V). To test this, set the supplied voltage to -1 V and again measure the current, noting the value. Typically, I only use devices where the current in reverse bias is no more than

0.1 mA greater than that at short circuit (*i.e.*, -2.1 mA). However, this also depends on the shape of the IV curve, which is the last thing we will collect to tell us about the function of the device. Testing the current in reverse bias can be a good way to weed out the completely bad devices before measuring the IV curve, however. If the current completely spikes at -1 V, move on to the other contact pair. If the same is true for the second contact pair, the device is simply bad and an IV curve does not need to be collected. If the contact pair is good, however, turn off the Keithley and use the command "mk.stop()" to stop the temperature control momentarily (the IV sweep will set it again) and then "ivt_sweep_continuous_N2.measureivt()" to measure the IV curve. Name the sample when prompted (typically I use "KE*notebook#*_*notebookpagepdevice#*_*contactpair*_test", an example of which is "KE3_123p1_1A_test"). I name the two contact pairs 1A and 2B simply to keep them straight (1A being on the left and 2B being on the right when the contacts are at the top). Next, test the other contact pair (if the first wasn't bad) to see whether it is good or not, but there's no need to measure another IV curve. Note the illumination intensity and the current in reverse bias.

36. Complete these testing steps for all devices in the batch, then use the command "fw.setfwpos(1,2)" to block the laser diode beam from reaching the sample, turn down the laser diode current to about 135 mA, replace the stage lid and screw it down, open the valve to the vacuum pump, screw down the screws, and remove the dewar line from the dewar. Collect the data off the computer for plotting if desired (I typically don't plot these IV curves but instead go off the current in reverse bias. However, if there is

a device on the border it could be good to plot the curve to decide whether or not to use it).

III. Sample making and measurement

1. Figure 37 illustrates the sample making steps outlined in this section. Turn the hot plate on. Make an SC1 solution and place on the hot plate. Make any necessary preparations for solution deposition.
2. Decide which device to use and check which side of the device the IBC cell is on and the contact pair that will be used.
3. Go down to CAMCOR to prepare the stage for use. Turn the laser diode current up to about 145 mA. Fill the liquid nitrogen dewar and attach. Loosen the lid screws, close the valve to the vacuum pump, ensure the house nitrogen valve is open, briefly open the nitrogen valve to the stage to reestablish atmospheric pressure, close the valve, and remove stage lid. If the IBC cell is on the left side of the device, the two probers on the side of the stage closest to the computer will be used for the p and n contacts while if

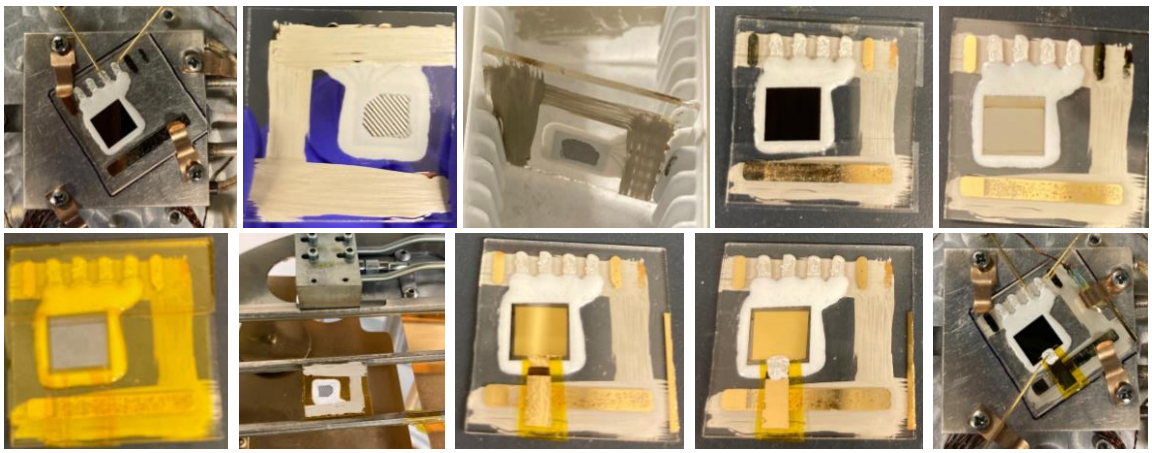

Figure 37. Sample making steps. From top left to bottom right: setting the light intensity, silver paint applied on back, silver paint drying, with clear tape mask, after film deposition, with Kapton tape mask, in evaporator, after gold deposition, with silver paint contact ed, and ready for measurement in Instec stage.

it is on the right side of the device, the two probers furthest from the computer will be used. If the probers in these locations need to be changed to reach the desired contacts, change them now. Ensure the correct BNCs are connected to the correct probers.

4. Turn on the computer monitor and restart the Python Shell using ctrl F6. Import the necessary programs using: “import Isc_Voc”, “import fw102c as fw”, “import mk2000 as mk”, “import keithley7001 as k7001”. Ensure the text file Isc_Voc.txt is open and that its parameters are set the way you want them to be. The only things I change regularly are “num sweeps” and “btw time” which are the number of measurements and time between measurements, respectively. For the first measurement of a time course, “num sweeps” = 1 and “btw time” = 0.
5. Back upstairs, make any additional preparations for depositing a film. This may include making a solution in an air free flask, getting a needle or two out of the hot oven, preparing a syringe or two, getting out a filter, etc.
6. Use acetone and a small kim wipe to remove the sharpie device number. Then use a different part of the kim wipe, also with acetone, to gently wipe the silicon surface. Next, use IPA and a kim wipe to wipe the silicon surface.
7. Set the hot plate timer to 10 minutes but don’t start it yet. Once the solution has reached 50C, rinse the device with water and then place it in the SC1, starting the timer simultaneously. Start an 8-minute timer for yourself.
8. When the 8-min timer goes off, start robing up to use BOE (HF). Put on a lab coat, switch to goggles from glasses, put on a pair of long cuff gloves (keep your lab coat sleeves tucked into them), then put on a pair of normal gloves. When the SC1 timer

goes off, rinse the device with water then bring over to the HF hood to dry with the nitrogen gun.

9. Open the BOE container. Using the Teflon tweezers in your non-dominant hand, hold the device by pinching the glass somewhere that feels sturdy. Using your dominant hand, use a plastic pipet to suction up some BOE. Carefully apply the BOE to only the silicon surface such that it beads up. Add enough to form a droplet large enough to cover the majority of the silicon surface. Etch for 1 minute. Gently use the tip of the plastic pipet to momentarily drag the BOE to each corner of the IBC cell that was uncovered. Be careful not to allow the BOE to spill over the edge of the silicon on to the glass. If it does, suction as much BOE off the surface as possible, then rinse with water. Otherwise, once applying the BOE to the corners, use the pipet to suction off the BOE, then rinse with water for about 5 seconds and blow dry with nitrogen. Being careful not to touch the silicon surface, use a small kim wipe to dry any glass that remains wet. Put the device in a sample carrier to transport downstairs and start a 10-minute timer.
10. Take the sample downstairs and place on the stage in the orientation it will be in for measurement. Use the clamps and the small Philips screwdriver and green tape tweezers in the top right drawer of the tool chest under this laser table to gently align the clamps on the glass of the device. Screw these down partially so the device may still be moved around on the stage but doesn't slide excessively. Use the p and n probers to contact the contact pair of choice. Use the Python shell to set the temperature of the stage to 300K, then open the filter wheel so the sample is illuminated. Turn the Keithley 2400 on to measure the short-circuit current. If positive, switch the BNCs. Move the

IBC cell around slightly on the stage to find the location where maximum current is measured. Once this location is found, tighten the screws to clamp the device in place.

11. Next, dial the laser diode current until the reading is about -2.05 mA. As the sample is exposed to air, the magnitude of the current will go down. I aim for the current to be -2.007 mA when the 10-minute timer goes off. This ensures the correct light intensity each time. Make small adjustments to the laser diode current as necessary to achieve the correct current when the timer goes off. During the last few minutes while waiting for the timer, use the fine point sharpie in the same drawer as the tweezers to gently draw a line around the IBC cell on the stage. This ensures correct placement of the cell after the film and contact have been deposited. Be careful not to move the device around while doing this. Note the final laser diode current (I write it using the sharpie on the laser table). If the dial gets bumped in future steps (which is unfortunately easy to do), you will be able to readjust it back to the correct intensity.
12. When the timer goes off, use the Python Shell to measure an IV curve like when testing devices (ivt_sweep_continuous_N2.measureivt()). When it is done, stop the temperature control, close the filter wheel, unscrew the clamps holding the device in place, remove the device, and replace the lid on the stage. It does not need to be completely screwed down at this point.
13. Take the device back upstairs. Apply a thin layer of silver paint to the bottom of the device, being careful not to cover the glass where the IBC contacts are illuminated. Use the kludge contraption to prop up the device while the silver paint dries.
14. Perform any film deposition prep that has not yet been done. This is also a good time to prepare for any device masking that may take place. I use tape masks both in the film

deposition process and in the contact deposition process (clear scotch tape in the former case and Kapton tape in the latter). Then, robe up for the second BOE etch.

15. Perform a BOE etch as above.
16. At this point, I use clear scotch tape to mask the device for film deposition. This involves putting one piece of tape over the top contacts and one over the bottom contacts without touching the silicon surface with the tape (this tape, unlike Kapton, leaves a residue). This protects the gold contacts from having film deposited on them. If this is not an issue for you, feel free to skip this step. Otherwise, mask the device as shown then place it on the vacuum chuck.
17. Use your solution of choice to spin the film. To make spiro-OMeTAD films 3-5 nm thick, I spin at 2000 rpm for 60 seconds (no specified acceleration). Each time I spin a film, I make a fresh salted solution from stock neat spiro-OMeTAD, *t*-BP, and Li-TFSI in acetonitrile or/and Co-TFSI in acetonitrile in a Schlenck flask. To spin the film, I use a 1 mL plastic syringe, longer metal reusable needle, and 0.1 μm PTFE filter. Use the needle and syringe to gather the solution, remove the needle, apply the filter, and dispense a drop or two of the solution onto the silicon through the filter. Spin!
18. Once the film is deposited, I set a 10-minute timer, but this could vary depending on what material you're working with. For me, 10 minutes is plenty of time to get the tape mask on (5 minutes can be cutting it short sometimes) but not so long that the film is exposed to air for a long time before going into the evaporator. In tape masking the film for contact deposition, it is imperative to NOT scratch the film. Use mostly large pieces of tape, but on the side nearest the large gold contact, use three smaller pieces to enable silver paint contact to be made after the gold contact is deposited.

19. Put the sample in the evaporator and evaporate 50 nm of gold. Let the sample cool 10 minutes before removing it. Upon venting the chamber, set a 10-minute timer. This is how long you have to make contact with the silver paint, transport the sample to the Instec chamber, align the sample with the sharpie mark from earlier, and start the first measurement.
20. Upon removing the sample from the evaporator, first remove all of the tape mask except the one small center piece on the side closest to the large gold contact on the glass.
21. Use the silver paint at the microscope station to carefully make contact between the gold on top of the film and the gold on top of the small piece of tape that is left. This ensures minimal dissolution of the film due to the silver paint solvent while enabling the use of a prober NOT directly on top of the film/contact, which typically will simply poke through the film/contact in this case because the films are so thin (which is bad). Once the silver paint is deposited, put the sample in a sample container, pull rough vacuum on the evaporator, and take the sample downstairs.
22. Remove the stage lid, set the temperature to 300K, place the sample on the stage, align it with the sharpie outline from before, clamp, and now use all three probers to make contact to the three contacts. In addition, use the Apiezon N grease to attach the temperature diode to the top of the glass of the sample. Use the closest clamp to securely clamp it to the surface.
23. Before starting the first measurement, test the contacts to make sure electrical contact is established. Test the pn contacts first. Ensure the correct channels are closed on the Keithley 7001, then open the filter wheel, quickly measure the current (make sure it's somewhere between -1.6 and -2.8 mA or so), then close the filter wheel again. Then,

change the contact pair under test. Use “k7001.opench(7, ‘All’)” and “k7001.closech(7, ‘(@ 1!1!1, 1!2!3)’) to close the connections to the pt contact pair. Switch the Keithley 2400 to source 0 current and measure voltage. Open the filter wheel and quickly measure the voltage. It should read a steady voltage somewhere between 0.05 and 0.5 V. If it is around 0.55 V or greater, or if the reading steadily climbs or decreases, there is likely an issue with connectivity. If this is the case, move the prober for the top contact slightly. Sometimes, simply adjusting where the prober sits on the silver paint can fix the issue. Once a “good” reading is established, close the filter wheel and switch the contact pair using “k7001.opench(7, ‘All’)” and “k7001.closech(7, ‘(@ 1!1!2, 1!2!3)”. Open the filter wheel and quickly measure the voltage, then close the filter wheel when a “good” reading is verified.

24. Stop the temperature control, replace and screw down the lid, drop the black curtain, and start the first measurement using “Isc_Voc.measure()”. While this measurement progresses, change “num sweeps” to 30 and “btw time” to 2 in the txt file to perform measurements every 2 minutes for 60 during the next measurement sequence. Save the file (this will not affect the current measurement so long as it has already been started because the program reads in the text file at the very beginning).
25. When the first measurement is complete, open the valve to the vacuum pump and start a 5-minute timer. Screw down the lid screws and briefly purge the stage with nitrogen gas by opening and then closing the nitrogen valve. As the pressure inside the stage drops, and then equalizes, continue purging with nitrogen gas about every 30 seconds to one minute until 30 seconds remain on the timer. Then, open the nitrogen gas valve such that about atmospheric pressure is reestablished, close the vacuum valve, open the

nitrogen gas valve another 1/8 or a turn or so, and return to the computer to start the next measurement.

26. When the timer goes off, use “Isc_Voc.measure()” to start the next measurement. Start a 45-minute timer. Once the first measurement has been completed, edit the txt file so “num sweeps” is 72 and “btw time” is 5 to perform measurements every 5 minutes for 6 hours and save the file. Wait until the second measurement has been performed before going back upstairs.
27. Back upstairs, close the roughing valve on the evaporator and open the backing valve. Clean glassware, needles, *etc.*, as necessary. Spend the rest of the time until the timer goes off as you wish. Typically, I make the Mathematica notebooks for processing of this sample’s data, drink some coffee, *etc.*
28. When the timer goes off, go back downstairs. This will provide plenty of time to get back downstairs before the first measurement is over. When the measurement is complete, close the nitrogen valve and briefly open the vacuum valve in order to unscrew the screws. Then, close the vacuum valve and then open the nitrogen valve until the stage lid is free to remove. Then, close the nitrogen valve. Remove the stage lid, placing it on the laser table, and carefully wave your hand over the stage to replace the nitrogen bathing the sample with air. Replace the black curtain, being very careful not to disturb the sample or probers while doing so (the stage lid remains off for measurements performed in air).
29. Start the next measurement using “Isc_Voc.measure()” and wait until the first two measurements have been performed before leaving to do other things. Gather data that has already been collected if you wish to look at it before all data is collected.

30. When the measurement is complete, perform an IV sweep if desired. Ensure the pn contacts are connected on the Keithley 7001, open the filter wheel, and use “ivt_sweep_continuous_N2.measureivt()” to perform the measurement.
31. Once all measurements are complete, remove the sample from the stage, use a small amount of ethanol and a kim wipe to clean the sharpie off the stage and laser table, turn the laser diode down to about 135 mA, remove the insert from the liquid nitrogen dewar, and collect the data from the computer. Replace the stage lid, screw down the screws, open the vacuum valve, and tighten the screws once more. All done.

REFERENCES CITED

1. Egelhofer Ruegger, K.E.; Roe, E.T.; Lonergan, M.C. Solar cell contacts: Quantifying the impact of interfacial layers on selectivity, recombination, charge transfer, and V_{oc}. *Proc. Natl. Acad. Sci.* in Review July 2020.

2. Roe, E.T.; Egelhofer, K.E.; Lonergan, M.C. Limits of contact selectivity/recombination on the open-circuit voltage of a photovoltaic. *ACS Appl. Energy Mater.* **2018**, *1*, 1037-1046.

3. Roe, E.T.; Egelhofer, K.E.; Lonergan, M.C. Exchange current density model for the contact-determined current-voltage behavior of solar cells. *J. Appl. Phys.* **2019**, *125*, 225302-1-12.

4. Egelhofer Ruegger, K.E.; Nieves, T.N.; Lonergan, M.C. Effects of Co(III) salt and *t*-BP on electron and hole transfer at spiro-OMeTAD-modified solar cell contacts. In preparation for submission to *Chem. Mater.* August 2020.

5. Ritchie, H.; Roser, M. Our World in Data, Energy. http://ourworldindata.org/energy (accessed April 2020).

6. Ramanujam, J.; Bishop, D.M.; Todorov, T.K.; Gunawan, O.; Rath, J.; Nekovei, R.; Artegiani, E.; Romeo, A. Flexible CIGS, CdTe and a-Si:H based thin film solar cells: A review. *Prog. Mater. Sci.* **2020**, *110*, 100619.

7. Hermle, M.; Felmann, F.; Bivour, M.; Goldschmidt, J.C.; Glunz, S.W. Passivating contacts and tandem concepts: Approaches for the highest silicon-based solar cell efficiencies. *Appl. Phys. Rev.* **2020**, *7*, 021305.

8. Fthenakis, V.; Thias, C.; Blumenthal, A.; Kulur, A.; Magliozzo, J.; Ng, D. Sustainability evaluation of CdTe PV: An update. *Renew. Sust. Energ. Rev.* **2020**, *123*, 109776.

9. Olaleru, S.A.; Kirui, J.K.; Wamwangi, D.; Roro, K.T.; Mwakikunga, B. Perovskite solar cells: The new epoch in photovoltaics. *J. Sol.* **2020**, *196*, 295-309.

10. Green, M.A. Photovoltaic Principles. *Physica E* **2002**, *14*, 11-17.

11. Sze, S.M. *Semiconductor Devices, Physics and Technology*, 2nd Ed., John Wiley and Sons, Inc.: Hoboken, NJ, 2002.

12. Würfel, P. *Physics of Solar Cells: From Basic Principles to Advanced Concepts*, 2nd ed., Wiley-VCH: Weinheim, 2009.

13. Shockley, W; Queisser, H.J. Detailed balance limit of efficiency of p-n junction solar cells. *J. Appl. Phys.* **1961**, *32*, 510-519.

14. Kirchartz, T.; Pieters, B.E.; Taretto, K.; Rau, U. Mobility dependent efficiencies of organic bulk heterojunction solar cells: Surface recombination and charge transfer state distribution. *Phys. Rev. B* **2009**, *80*, 035334-1-6.

15. Swanson, R.M. "Approaching the 29% limit efficiency of silicon solar cells," *Conference Record of the Thirty-first IEEE Photovoltaic Specialists Conference*, 2005, Lake Buena Vista, FL, USA, 2005, pp. 889-894.

16. Liu, Z.; Krückemeier, L.; Krogmeier, B.; Klingebiel, B.; Márquez, J.A.; Levcenko, S.; Öz., S.; Mathur, S.; Rau, U.; Unhold, T.; Kirchartz, T. Open-circuit voltages exceeding 1.26 V in planar methylammonium lead iodide perovskite solar cells. *ACS Energy Lett.* **2019**, *4*, 110-117.

17. Snaith, H.J.; Grätzel, M. Electron and Hole Transport through Mesoporous TiO_2 Infiltrated with Spiro-OMeTAD. *Adv. Mater*. **2007**, *19*, 3643-3647.

18. Abate, A.; Leijtens, T.; Pathak, S.; Teuscher, J.; Avolio, R.; Errico, M.E.; Kirkpatrik, J.; Ball, J.M.; Docampo, P.; McPherson, I.; Snaith, H.J. Lithium salts as "redox active" p-type dopants for organic semiconductors and their impact in solid-state dye-sensitized solar cells. *Phys. Chem. Chem. Phys.* **2013**, *15*, 2572-2579.

19. Correa-Baena, J.-P.; Tress, W.; Domanski, K.; Anaraki, E.H.; Turren-Cruz, S.-H.; Roose, B.; Boix, P.B.; Grätzel, M.; Saliba, M.; Abate, A.; Hagfeldt, A. Identifying and suppressing interfacial recombination to achieve high open-circuit voltage in perovskite solar cells. *Energy Environ. Sci.* **2017**, *10*, 1207-1212.

20. Weber, S.A.L.; Hermes, I.M.; Turren-Cruz, S.-H.; Gort, C.; Bergmann, V.W.; Gilson, L.; Hagfeldt, A.; Grätzel, M.; Tress, W.; Berger, R. How the formation of interfacial charge causes hysteresis in perovskite solar cells. *Energy Environ. Sci.* **2018**, *11*, 2281-2634.

21. Marinova, N.; Tress, W.; Humphry-Baker, R.; Dar, M.I.; Bojinov, V.; Zakeeruddin, S.M.; Nazeeruddin, M.K.; Grätzel, M. Light harvesting and charge recombination in $CH_3NH_2PbI_3$ perovskite solar cells studied by hole transport layer thickness variation. *ACS Nano* **2015**, *9*, 4200-4209.

22. Lu, J.; Lin, X.; Jiao, X.; Gengenbach, T.; Scully, A.D.; Jiang, L.; Tan, B.; Sun, J.; Li, B.; Pai, N.; Bach, U.; Simonov, A.N.; Cheng, Y.-B. Interfacial benzenethiol modification facilitates charge transfer and improves stability of cm-sized metal halide perovskite solar cells with up to 20% efficiency. *Energy Environ. Sci.* **2018**, *11*, 1880-1889.

23. Juarez-Perez, E.J.; Wußler, M.; Fabregat-Santiago, F.; Lakus-Wollny, K.; Mankel, E.; Mayer, T.; Jaegermann, W.; Mora-Seró, I. Role of the selective contacts in the performance of lead halide perovskite solar cells. *Phys. Chem. Lett.* **2014**, *5*, 680-685.

24. Dualeh, A.; Moehl, T.; Nazeeruddin, M.K.; Grätzel, M. Temperature dependence of transport properties of Spiro-OMeTAD as a hole transport material in solid-state dye-sensitized solar cells. *ACS Nano* **2013**, *7*, 2292-2301.

25. Yadav, P.; Turrne-Cruz, S.-H.; Prochowicz, D.; Tavakoli, M.M.; Pandey, K.; Zakeeruddin, S.M.; Grätzel, M.; Hagfeldt, A.; Saliba, M. Elucidation of charge recombination and accumulation mechanism in mixed perovskite solar cells. *J. Phys. Chem. C* **2018**, *122*, 15149-15154.

26. Cappel, U.B.; Daeneke, T.; Bach, U. Oxygen-induced doping of Spiro-OMeTAD in solid-state dye-sensitized solar cells and its impact on device performance. *Nano Lett.* **2012**, *12*, 4925-4931.

27. Belisle, R.A.; Jain, P.; Rasanna, R.; Leijtens, T.; McGehee, M.D. Minimal effect of the hole-transport material ionization potential on the open-circuit voltage of perovskite solar cells. *ACS Energy Lett.* **2016**, *1*, 556-560.

28. Dualeh, A.; Moehl, T.; Tetreault, N.; Teuscher, J.; Gao, P.; Nazeeruddin, M.K.; Grätzel, M. Impedance spectroscopic analysis of lead iodide perovskite-sensitized solid-state solar cells. *ACS Nano* **2014**, *8*, 362-373.

29. Chueh, C.-C.; Li, C.-A.; Jen, A. Recent progress and perspective in solution-processed interfacial materials for efficient and stable polymer and organometal perovskite solar cells. *Energy Environ. Sci.* **2015**, *8*, 1160-1189.

30. Bach, U.; Lupo, D.; Comte, P.; Moser, J.E.; Weissörtel, F.; Slabeck, J.; Spreitzer, H.; Grätzel, M. Solid-state dye-sensitized mesoporous TiO_2 solar cells with high photon-to-electron conversion efficiencies. *Nature* **1998**, *395*, 583-85.

31. Kim, H.-S.; Lee, C.-R.; Im, J.-H.; Lee, K.-B.; Moehl, T.; Marchioro, A.; Moon, S.-J.; Humphry-Baker, R.; Yum, J.-H.; Moser, J.E.; Grätzel, M.; Park, N.-G. Lead Iodide Perovskite Sensitized All-Solid-State Submicron Thin Film Mesoscopic Solar Cell with Efficiency Exceeding 9%. *Scientific Reports* **2012**, *2 (591)*, 1-7.

32. Zuo, C.; Bolink, H.J.; Han, H.; Huang, J.; Cahen, D.; Ding, L. Advances in Perovskite Solar Cells. *Adv. Sci.* **2016**, *3*, 1500324.

33. Wu, Y.; Yan, D.; Peng, J.; Duong, T.; Wan, Y.; Phang, S.P.; Shen, H.; Wu, N.; Barugkin, C.; Fu, X.; Surve, S.; Grant, D.; Walter, D.; White, T.P.; Catchpole, K.R.; Weber, K.J. Monolithic perovskite/silicon-homojunction tandem solar cell with over 22% efficiency. *Energy Environ. Sci.* **2017**, *10*, 2472-2479.

34. Bush, K.A.; Palmstrom, A.F.; Yu, Z.J.; Boccard, M.; Cheacharoen, R.; Mailoa, J.P.; McMeekin, D.P.; Hoye, R.L.Z.; Bailie, C.D.; Leijtens, T.; Peters, I.M.; Minichetti, M.C.; Rolston, N.; Prasanna, R.; Sofia, S.; Harwood, D.; Ma, W.; Maghadam, F.; Snaith, H.J.; Buonassisi, T.; Holman, Z.C.; Bent, S.F.; McGehee, M.D. 23.6%-Efficient monolithic perovskite/silicon tandem solar cells with improved stability. *Nature Energy* **2017**, *2*, 17009.

35. Ratcliff, E.L.; Zacher, B.; Armstrong, N.R. Selective interlayers and contacts in organic photovoltaic cells. *J. Phys. Chem. Lett.* **2011**, *2*, 1337-1350.

36. Schulz, P.; Edri, E.; Kirmayer, S.; Hodes, G.; Cahen, D.; Kahn, A. Interface energetics in organo-metal halide perovskite-based photovoltaic cells. *Energy Environ. Sci.* **2014**, *7*, 1377-1381.

37. Schölin, R.; Karlsson, M.H.; Eriksson, S.K.; Siegbahn, H.; Johansson, E.M.J.; Rensmo, H. Energy level shifts in spiro-OMeTAD molecular thin films when adding Li-TFSI. *J. Phys. Chem. C* **2012**, *116*, 26300-26305.

38. Yavari, M.; Mazlou-Ardakani, M.; Gholipour, S.; Tavakoli, M.M.; Taghavinia, N.; Hagfeldt, H.; Tress, W. Reducing surface recombination by a poly(4-vinylpridine) interlayer in perovskite solar cells with high open-circuit voltage and efficiency. *ACS Omega* **2018**, *3*, 5038-5043.

39. Wang, S.; Sina, M.; Parikh, P.; Uekert, T.; Shahbizian, B.; Devaraj, A.; Meng, Y.S. Role of 4-tert-Butylpyridine as a Hole Transport Layer Morphological Controller in Perovskite Solar Cells. *ACS Nano Lett.* **2016**, *16*, 5594-5600.

40. Wang, S.; Huang, Z.; Wang, X.; Li, Y.; Günther, M.; Valenzuela, S.; Parikh, P.; Cabreros, A.; Xiong, W.; Meng, Y.S. Unveiling the Role of tBP-LiTFSI Complexes in Perovskite Solar Cells. *J. Am. Chem. Soc.* **2018**, *140*, 16720-16730.

41. Lamberti, F.; Gatti, T.; Cescon, E.; Sorrentino, R.; Rizzo, A.; Menna, E.; Meneghesso, G.; Meneghetti, M.; Petrozza, A.; Franco, L. Evidence of Spiro-OMeTAD De-doping by tert-Butylphridine Additive in Hole-Transporting Layers for Perovskite Solar Cells. *Chem* **2019**, *5*, 1806-1817.

42. Burschka, J.; Dualeh, A.; Kessler, F.; Baranoff, E.; Cevey-Ha, N.-L.; Yi, C.; Nazeeruddin, M.K.; Grätzel, M. Tris(2-(1*H*-pyrazol-1-yl)pyridine)cobalt(III) as p-Type Dopant for Organic Semiconductors and Its Application in Highly Efficiency Solid-State Dye-Sensitized Solar Cells. *J. Am. Chem. Soc.* **2011**, *133*, 18042-18045.

43. Burschka, J.; Kessler, F.; Nazeeruddin, M.K.; Grätzel, M. Co(III) Complexes as p-Dopants in Solid-State Dye-Sensitized Solar Cells. *Chem. Mater.* **2013**, *25*, 2986-2990.

44. Noh, J.H.; Jeon, N.J.; Choi, Y.C.; Nazeeruddin, M.K.; Grätzel, M.; Seok, S.I. Nanostructured $TiO_2/CH_3NH_3PbI_3$ Heterojunction Solar Cells Employing Spiro-OMeTAD/Co-complex as Hole-Transporting Material. *J. Mater. Chem. A* **2013**, *1*, 11842-11847.

45. Ma, Y.; Fan, J.; Zhang, C.; Li, H.; Li, W.; Mai, Y. Enhanced Charge Collection and Stability in Planar Perovskite Solar Cells Based on a Cobalt(III)-Complex Additive. *RSC Adv.* **2017**, *7*, 37654-37658.

46. Lu, J.; Scully, A.D.; Sun, J.; Tan, B.; Chesman, A.S.R.; Raga, S.R.; Jiang, L.; Lin, X.; Pai, N.; Huang, W.; Cheng, Y.-B.; Bach, U.; Simonov, A.N. Multiple Roles of Cobalt Pyrazol-Pyridine Complexes in High-Performing Perovskite Solar Cells. *J. Phys. Chem. Lett.* **2019**, *10*, 4675-4682.

47. Kruger, J.; Plass, R.; Cevey, L.; Piccirelli, M.; Grätzel, M.; Bach, U. High Efficiency Solid-State Photovoltaic Device Due to Inhibition of Interface Charge Recombination. *Appl. Phys. Lett.* **2001**, *79*, 2085-2087.

48. Jacobs, D.A.; Wu, Y.; Shen, H.; Barugkin, C.; Beck, F.J.; White, T.P.; Weber, K.; Catchpole, K.R. Hysteresis phenomena in perovskite solar cells: the many and varied effects of ionic accumulation. *Phys. Chem. Chem. Phys.* **2017**, *19*, 3094-3103.

49. Unger, E.L.; Hoke, E.T.; Bailie, C.D.; Nguyen, W.H.; Bowring, A.R.; Heumüller, T.; Christoforo, M.G.; McGehee, M.D. Hysteresis and transient behavior in current-voltage measurements of hybrid-perovskite absorber solar cells. *Energy Environ. Sci.* **2014**, *7*, 3690-3698.

50. Tress, W.; Marinova, N.; Moehl, T.; Zakeeruddin, S.M.; Nazeeruddin, M.K.; Grätzel, M. Understanding the rate-dependent *J-V* hysteresis, slow time component, and aging in $CH_3NH_3PbI_3$ perovskite solar cells: the role of compensated electric field. *Energy Environ. Sci.* **2015**, *8*, 995-1004.

51. Mora-Seró, I.; Bisquert, J. Effect of reduced selectivity of contacts on the current-potential characteristics and conversion performance of solar cells. *Sol. Energy Mater. Sol Cells* **2005**, *85*, 51-62.

52. Sandberg, O.J.; Sundqvist, A.; Nyman, M.; Österbacka, R. Relating charge transport, contact properties, and recombination to open-circuit voltage in sandwich-type thin-film solar cells. *Phys. Rev. App.* **2016**, *5*, 044005.

53. Brendel, R.; Peibst, R. Contact selectivity and efficiency in crystalline silicon photovoltaics. *IEEE J. Photovolt.* **2016**, *6*, 1413-1420.

54. Chavali, R.V.K.; Wilcox, J.R.; Ray, B.; Gray, J.L.; Alam, M.A. Correlated nonideal effects of dark and light *I-V* characteristics in a-Si/c-Si heterojunction solar cells. *IEEE J. Photovolt.* **2014**, *4*, 763-771.

55. Sandberg, O.J.; Nyman, M.; Österbacka, R. Effect of contacts in organic bulk heterojunction solar cells. *Phys. Rev. App.* **2014**, *1*, 024003.

56. Wagenpfahl, A.; Rauh, D.; Binder, M.; Deibel, C.; Dyakonov, V. S-shaped current-voltage characteristics of organic solar devices. *Phys. Rev. B* **2010**, 82, 115306.

57. Niemegeers, A.; Burgelman, M. Effects of the Au/CdTe back contact on *IV* and *CV* characteristics of Au/CdTe/CdS/TCO solar cells. *J. Appl. Phys.* **1997**, *81*, 2881-2886.

58. Horio, K.; Yanai, Y. Numerical modelling of heterojunctions including the thermionic emission mechanism at the heterojunction interface. *IEEE Trans. On Elec. Dev.* **1990**, *37*, 1093-1098.

59. Rhoderick, E.H.; Williams, R.H. *Metal-Semiconductor Contacts*, 2nd ed., Oxford University Press, Oxford, 1988.

60. Weber, C.D.; Stay, D.P.; Lonergan, M.C. Effects of Polyfluorene Polyelectrolyte Interfacial Layers on Selectivity and Recombination Measured Using the Interdigitated Back-Contact Solar Cell. *J. Phys. Chem. C* **2016**, *120*, 19951-19960.

61. Mulligan, W.P.; Cudzinovic, M.J.; Pass, T.; Smith, D.; Kaminar, N.; McIntosh, K.; Swanson, R.M. Solar cell and method of manufacture. U.S. Patent 7897867B1, 2011.

62. Miyata, A.; Mitioglu, A.; Plochocka, P.; Portugall, O.; Wang, J.T.-W.; Stranks, S.D.; Snaith, H.J.; Nicholas, R.J. Direct measures of the exciton binding energy and effective masses for charge carriers in organic-inorganic tri-halide perovskites. *Nat. Phys.* **2015**, *11*, 582-587.

63. Saygili, Y.; Kim, H.-S.; Yang, B.; Suo, J.; Muñoz-Garcia, A.B.; Pavone, M.; Hagfeldt, A. Revealing the Mechanism of Doping of *spiro*-MeOTAD via Zn Complexation in the Absence of Oxygen and Light. *ACS Energy Lett.* **2020**, *5*, 1271-1277.

64. Bard, A.J.; Faulkner, L.R. *Electrochemical Methods: Fundamentals and Applications*, 2nd Ed.; D. Harris, E. Swain, C. Robey, E. Aiello; John Wiley & Sons, Inc.: Hoboken, NJ, 2001.

65. Röhr, J.A.; Shi, X.; Haque, S.A.; Kirchartz, T.; Nelson, J. Charge transport in spiro-OMeTAD investigated through space-charge-limited current measurements. *Phys. Rev. Appl.* **2018**, *9*, 044017.